ALTERNANS AND ATRIAL FIBRILLATION: FROM CELLULAR MECHANISMS TO ARRHYTHMOGENESIS

by

Kelly C. Chang

A dissertation submitted to Johns Hopkins University in conformity with the requirements for the degree of Doctor of Philosophy.

Baltimore, Maryland

June, 2016

Abstract

Atrial fibrillation (AF) is the most common cardiac arrhythmia, but knowledge of the arrhythmogenic substrate is incomplete. Alternans, the beat-to-beat alternation in cardiac electrical signals, typically occurs at fast heart rates and can sometimes lead to arrhythmia. Atrial alternans has been observed at slow pacing rates in cardioverted AF patients, suggesting that alternans may play an important role in the arrhythmogenic substrate of AF. The mechanisms underlying alternans in patients at slow pacing rates, and the contribution of atrial alternans to arrhythmogenesis, are currently unknown.

In order to address these gaps in understanding, a computational approach was used to elucidate the cellular mechanisms underlying alternans and to assess the effects of alternans on arrhythmogenesis in the atria. Simulations revealed that reduced ryanodine receptor (RyR2) inactivation, resulting in a steep sarcoplasmic reticulum (SR) Ca^{2+} release-load relationship, was responsible for alternans at slower pacing rates. The effect of these Ca^{2+}-driven alternans (CDA) on arrhythmogenesis was explored using an anatomically realistic, 3D model of the human atria. It was found

ABSTRACT

that CDA significantly increased the vulnerability of the atria to arrhythmia. Furthermore, CDA was found to promote arrhythmia maintenance through frequent wavebreak, which led to increased arrhythmia complexity and scroll wave persistence. Thus, these findings suggest that disrupted SR Ca^{2+} release in the atria is linked to arrhythmogenesis via the influence of alternans.

This research provides a rationale for new mechanistic therapies for AF, suggesting that targeting RyR2s may be an effective antiarrhythmic strategy. Incorporation of these findings into future models may aid in the development of better treatment strategies for AF.

Primary Reader: Natalia A. Trayanova, Ph.D.

Secondary Reader: Feilim Mac Gabhann, Ph.D.

Acknowledgments

This thesis work would not have been possible without the support and mentorship of my advisor, Dr. Natalia Trayanova. I thank her for always believing in me and challenging me to be a better scientist. I would like to thank the members of my thesis committee, Dr. Leslie Tung and Dr. Feilim Mac Gabhann, who have provided valuable insight and advice on this work. I thank Dr. Seth Weinberg and Dr. Jason Bayer for their tutelage and guidance during my early years as a graduate student. To all the past and present members of the Computational Cardiology Lab with whom I have had the privilege of working, thank you for all the good times and memories.

My experience in graduate school would not have been the same without the close friends and family who have made this place home. I especially wish to thank my parents, Ted and Jane, and my sister Alice for all of their love and encouragement. I would not be where I am today without their support. And to Andrew, who has been a steadfast source of comfort and joy throughout all the ups and downs on this journey, thank you for everything.

Contents

List of Tables

List of Figures

Chapter 1

Background and Motivation

1.1 Cardiac Electrophysiology

The heart is responsible for pumping blood to deliver oxygen and nutrients to the body. The heart muscle (myocardium) is composed of a network of electrically coupled excitable cells (cardiomyocytes), which are organized into fibers and laminar sheets. Electrical signals control mechanical contraction of the heart, and the orderly conduction of electricity through the cardiac syncytium is central to the heart's function. Under normal circumstances, contraction (systole) is initiated by an electrical signal from the sinoatrial node (SAN). This electrical signal propagates through the right atrium (RA) and left atrium (LA), the upper chambers of the heart, causing them to contract. The ventricles, the lower chambers of the heart, are separated from the atria by nonconductive fibrous tissue. During atrial systole, the ventricles

are in diastole (relaxed), and contraction of the atria helps to fill the ventricles with blood. Conduction of electricity from the atria to the ventricles occurs through the atrioventricular node (AVN) and the bundle of His. At the AVN, conduction slows to allow proper timing of contraction between the atria and ventricles. The bundle of His then carries the electrical signal across the fibrous tissue to the Purkinje fibers, a specialized network of cells which rapidly conducts electrical signals to the ventricles. This results in the synchronized contraction of both the right ventricle (RV) and left ventricle (LV), which pump blood to the lungs and body, respectively. After ejecting blood, the myocardium returns to diastole until the next beat is initiated from the SAN.

1.1.1 Cardiac Action Potentials

The electrical signals in the heart are known as action potentials (APs). An AP is the characteristic depolarization and repolarization of the excitable membrane (sarcolemma) of a cardiomyocyte. During an AP, voltage-gated ion channels located in the sarcolemma open in response to changes in membrane polarization, allowing concentration gradients to drive ions across the membrane. This ionic current flow in turn changes the polarization of the sarcolemma, which acts as a capacitor. The voltage across the sarcolemma is known as the transmembrane potential (V_m). Cardiomyocytes are electrically coupled through low-resistance intercellular channels called gap junctions, which allow APs to propagate and excite neighboring cells.

Figure 1.1: Currents that underlie the mammalian cardiac AP[1]

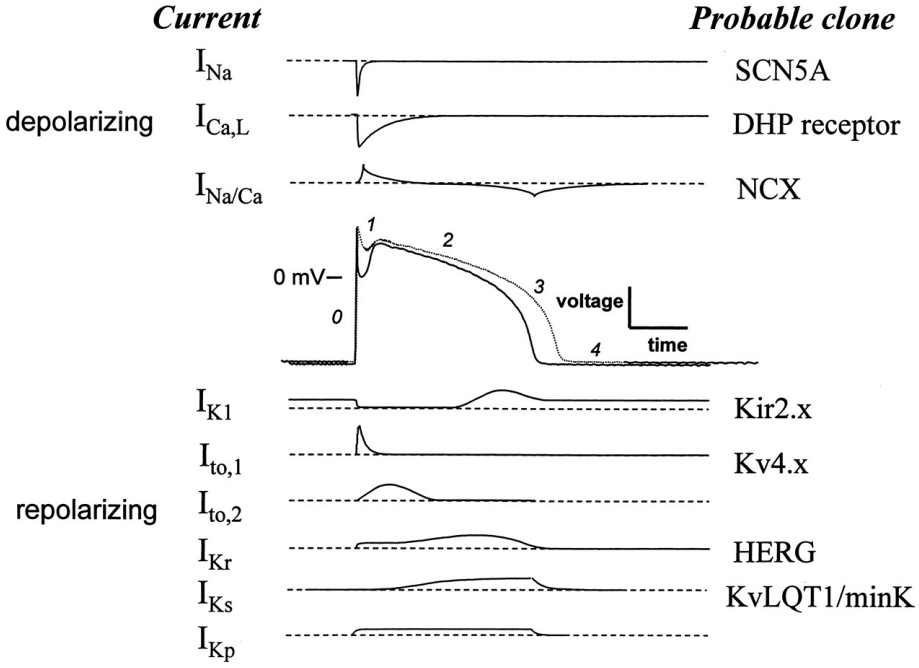

Schematic of the depolarizing and repolarizing currents that underlie the action potential (AP) in the mammalian ventricle. A control (solid line) and failing (dotted line) AP profile are shown in the center. The phases of the AP are labeled. A schematic of the time course of each of the currents is shown as well as the gene product that underlies the current.

Ventricular and atrial myocytes undergo five phases during an AP (Fig. 1.1). During the resting phase (phase 4), the inward rectifier K^+ current (I_{K1}) maintains V_m at a resting potential near -80 mV. When an initiating stimulus raises V_m above the threshold potential (around -40 mV), fast Na^+ channels activate and Na^+ flows from the extracellular space into the cell, resulting in the rapid depolarization of the membrane (the upstroke, phase 0). During phase 1, the fast Na^+ channels inactivate and

[1]Reprinted from G. Tomaselli, "Electrophysiological remodeling in hypertrophy and heart failure," *Cardiovascular Research*, vol. 42, no. 2, pp. 270–283, may 1999, by permission of Oxford University Press.

transient outward K^+ channels activate, resulting in outward flow of K^+ and a brief repolarization period (the "notch" in the AP). During phase 2, transient outward K^+ channels close, and L-type Ca^{2+} channels and delayed rectifier K^+ channels activate. The inward Ca^{2+} current and the outward current K^+ carried are balanced, so V_m does not change significantly during phase 2 (the plateau phase). During phase 3, the L-type Ca^{2+} channels inactivate and the delayed rectifier K^+ current repolarizes the membrane. As V_m returns to rest, the delayed rectifier K^+ channels close, and I_{K1} dominates again in phase 4.

Action potential duration (APD) is the span of time between the AP upstroke (phase 0) and repolarization (phase 3). APD can be quantified at different levels of repolarization. For example, APD90 refers to the duration between phase 0 and 90% repolarization of V_m.

1.1.2 Excitation–Contraction Coupling

An AP triggers the cardiomyocyte to shorten in a process known as excitation–contraction (EC) coupling (Fig. 1.2). The AP is coupled to the mechanical contraction of the myocyte via Ca^{2+}. Critical to this process are structures called T-tubules, which are invaginations in the sarcolemma that carry the electrical signal into the central regions of the cardiomyocyte. Ca^{2+} signaling occurs in the narrow junction between the sarcolemma of the T-tubules and the sarcoplasmic reticulum (SR) membrane. When the membrane depolarizes during an AP and the voltage-gated L-type

Figure 1.2: Ca^{2+} transport in ventricular myocytes[2]

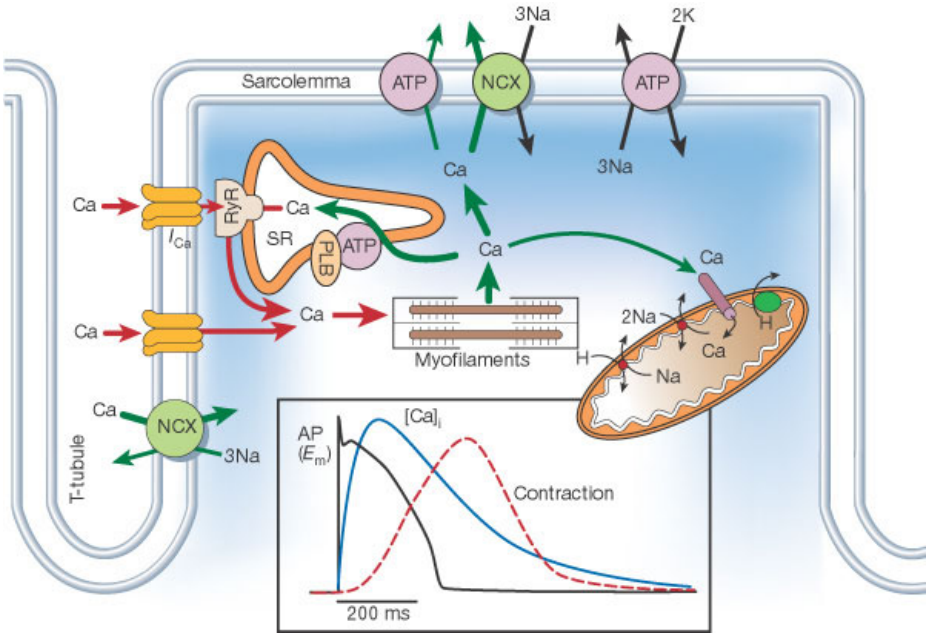

Inset shows the time course of an action potential (AP), Ca^{2+} transient (CaT), and contraction measured in a rabbit ventricular myocyte at 37 °C. NCX, Na^{+}/Ca^{2+} exchanger; ATP, ATPase; PLB, phospholamban; SR, sarcoplasmic reticulum.

Ca^{2+} channels open, Ca^{2+} flows from the extracellular space in the T-tubules to the junctional space (also known as the diad). Ca^{2+} in the diad binds to ryanodine receptors (RyR2s), ion channels located in the SR membrane, triggering them to open and release Ca^{2+} stored in the SR—a process known as Ca^{2+}-induced Ca^{2+} release (CICR). Ca^{2+} also binds to and inactivates L-type Ca^{2+} channels in the diad. Ca^{2+} then diffuses out of the diad into the cytosol, where it binds to myofilaments, allowing the thin and thick filaments to slide against each other and contract the cell. During

[2]Reprinted by permission from Macmillan Publishers Ltd: D. M. Bers, "Cardiac excitation–contraction coupling," *Nature*, vol. 415, no. 6868, pp. 198–205, jan 2002.

relaxation, as Ca^{2+} dissociates from the myofilaments, it is pumped back into the SR by the sarco/endoplasmic reticulum Ca^{2+}-ATPase (SERCA), and it is extruded from the cell by the Na^+/Ca^{2+} exchanger (NCX). A small amount of Ca^{2+} is also extruded by the sarcolemmal Ca^{2+}-ATPase. Calsequestrin (CSQN) binds Ca^{2+} in the SR and helps to store Ca^{2+} at very high concentrations.

1.1.3 Arrhythmogenesis

Cardiac arrhythmias are disruptions in the normal pattern of electrical propagation in the heart. They can occur when the heartbeat is too fast (tachyarrhythmias) or too slow (bradyarrhythmias). Tachyarrhythmias may arise from triggered (ectopic) beats originating outside the SAN, or from what is known as reentry. Reentry occurs when a wave encounters conduction block and is able to propagate around the area of block, eventually re-exciting the previously refractory tissue where block occurred. Reentry persists as long as there is excitable tissue along the direction of propagation. Hence, wavelength (the distance traveled by the electrical impulse during one refractory period) is a critical determinant of reentry vulnerability, since the wavelength must always be shorter than the reentrant circuit. Reduced conduction velocity (CV) and shortened APD both decrease wavelength and thus promote reentry.

Reentry can be either anatomical or functional. In anatomical reentry, a physical obstacle such as fibrotic scar tissue anchors the reentry, which propagates around the non-conducting obstacle (Fig. 1.3A). In functional reentry, all tissue is excitable, but

Figure 1.3: Reentry and arrhythmia

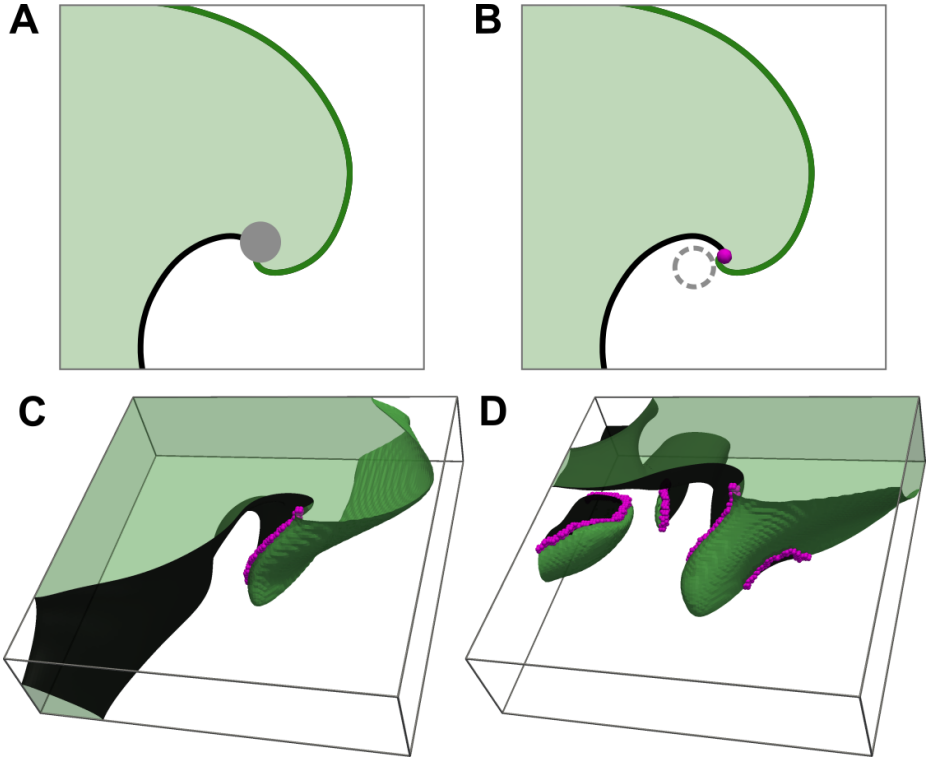

Cardiac tissue with propagating electrical waves (light green), wavefronts (green), wavebacks (black), and filaments (pink). **A.** 2D view of anatomical reentry anchored by a non-conducting obstacle (gray circle). **B.** 2D view of functional reentry rotating around an unexcited core region (dotted gray circle). **C.** 3D view of a single scroll wave. **D.** 3D view of multiple wavelets.

there is a small core region of unexcited tissue around which a scroll wave rotates (Fig. 1.3B). A vortex filament is the organizing center of the scroll wave, located at its tip where the wavefront meets the waveback. Both anatomical and functional reentry require spatial heterogeneity to occur. In the case of functional reentry, this arises from differences in excitability, refractoriness, or tissue structure.

Many tachyarrhythmias are characterized by a single scroll wave or reentrant

circuit (Fig. 1.3C). These can degrade into fibrillation, the most severe form of tachyarrhythmia, when a single wave breaks up into multiple scroll waves or wavelets (Fig. 1.3D). The number of vortex filaments present is thus an indicator of the complexity of the arrhythmia. During fibrillation, the heart is unable to pump blood due to the disorganized electrical activity in the myocardium.

1.1.4 Cardiac Alternans

Alternans is the beat-to-beat alternation in cardiac electrical signals. Alternans can occur at the cellular level, driven by refractoriness of cellular ionic currents, and at the tissue level, driven by conduction refractoriness. At the cellular level, alternans in V_m (such as APD alternans) and alternans in ion concentration usually occur together due to the fact that they are bidirectionally coupled via electrogenic transmembrane currents. Because intracellular Ca^{2+} concentration ($[Ca^{2+}]_i$) varies over a wide range during EC coupling, V_m is often closely coupled to changes in $[Ca^{2+}]_i$. The primary driver of cellular alternans can be either voltage or Ca^{2+} mechanisms.

Alternans can promote arrhythmia by increasing repolarization dispersion in the myocardium, leading to increased wave breakup and reentry [3]. Alternans has been observed in the ventricles of heart failure patients and has been linked to increased arrhythmia susceptibility [4, 5].

1.1.4.1 Voltage-Driven Alternans

Figure 1.4: APD restitution and alternans[3]

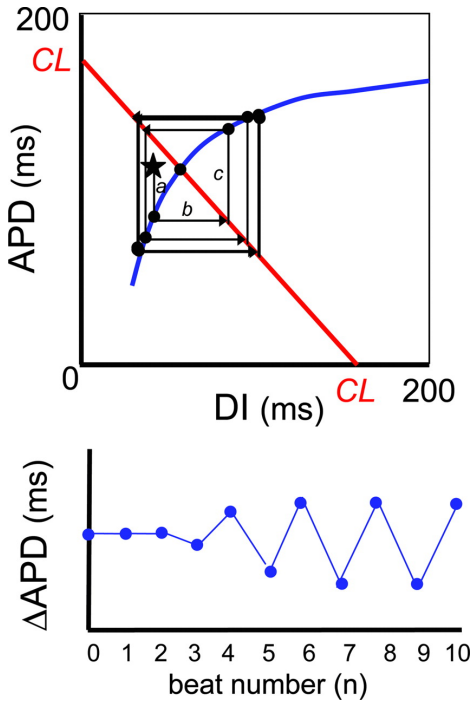

Cobweb diagram of APD alternans arising from steep APD restitution slope, after Ref. [6]. Blue line shows the APD restitution curve, and red line shows the CL = APD + DI line. The top graph illustrates the effects of a perturbation, which shortens DI (asterisk), displacing the system from its unstable equilibrium point (solid black circle at the intersection of the two lines), resulting in persistent APD alternans, as shown in the bottom trace.

APD restitution is the relationship between APD and the preceding diastolic interval (DI). The shape of the APD restitution curve reflects the recovery of the various inward and outward currents that generate the AP. APD typically decreases as DI decreases. When the cell is paced at a fixed rate, the relationship between APD and the following DI is determined by the pacing cycle length (CL). The intersection

[3]Reprinted from J. N. Weiss, A. Karma, Y. Shiferaw, P. S. Chen, A. Garfinkel, and Z. Qu, "From pulsus to pulseless: The saga of cardiac alternans," *Circulation Research*, vol. 98, no. 10, pp. 1244–1253, may 2006, by permission from Wolters Kluwer.

of the APD restitution curve and the pacing CL curve determines the operating point of the system. One can apply fixed point stability analysis to understand the limiting behavior of the system described by the APD restitution curve (Fig. 1.4). APD on the current beat determines APD on subsequent beats through an iterative mapping between the APD restitution function and the pacing CL function. At any given pacing rate, the fixed point is stable if the slope of the restitution curve at the fixed point is <1. At fast pacing rates, the slope of the restitution curve is usually >1, and APD alternans occurs as a result of persisting oscillations around the fixed point.

1.1.4.2 Calcium-Driven Alternans

During EC coupling, Ca^{2+} cycles between the extracellular space and intracellular and SR compartments. The stability of Ca^{2+} cycling depends upon the recovery of these different fluxes from beat to beat. When one or more components of Ca^{2+} cycling lags behind on a given beat, this results in changes in the amplitude and/or duration of the intracellular Ca^{2+} transient (CaT). This in turn impacts the subsequent CaT, leading to alternation analogous to that occurring in V_m due to steep APD restitution. These Ca^{2+}-driven alternans (CDA) depend upon many different factors. Since the CaT is primarily composed of Ca^{2+} released from the SR, two major determinants of Ca^{2+} cycling stability are SR Ca^{2+} uptake efficiency and SR Ca^{2+} release. SR Ca^{2+} uptake efficiency determines how quickly SERCA can restore SR load (the amount of Ca^{2+} in the SR) during diastole. SR Ca^{2+} release changes as

a function of the amount of trigger Ca^{2+} (Ca^{2+} influx through L-type Ca^{2+} channels) and SR load. SR Ca^{2+} release can also depend upon refractoriness of RyR2s [8].

CaT alternans couple to V_m via sarcolemmal Ca^{2+} currents. A large CaT results in increased Ca^{2+} extrusion by NCX, which exchanges three Na^+ for one Ca^{2+}, generating a net inward current. Inward NCX current (I_{NCX}) depolarizes the membrane and causes APD prolongation. On the other hand, a large CaT also results in increased Ca^{2+}-dependent inactivation of L-type Ca^{2+} current (I_{CaL}), which promotes APD shortening. These relations are reversed during the small CaT. Whether the large CaT produces APD prolongation (positive coupling) or APD shortening (negative coupling) depends on the relative balance of I_{NCX} and I_{CaL}.

1.1.4.3 Conduction Alternans

CV in the myocardium depends on tissue structure, the number of gap junctions between cells, and fast Na^+ current (I_{Na}) availability. At faster pacing rates, I_{Na} has less time to recover from inactivation, so fewer channels are available to elicit an AP, resulting in slowed propagation. CV restitution describes how CV changes as a function of the preceding DI. When the slope of the CV restitution curve is steep, CV alternans occurs. Variation in CV impacts the effective CL experienced by tissue distant from the pacing site. During slow conduction, the propagating wavefront takes longer to reach distant sites, so these sites experience a longer CL and a longer DI. During fast conduction, the inverse is true. In tissue, therefore, the effects of APD

restitution and Ca^{2+} cycling restitution are tied to the effects of CV restitution. At fast pacing rates, these interactions can result in discordant alternans, when different regions of tissue alternate out of phase with each other [9]. The regions of positive and negative phase are separated by nodal lines or surfaces, where alternans magnitude is zero.

1.2 Atrial Fibrillation

Atrial fibrillation (AF) is currently the most common sustained arrhythmia and is associated with significant morbidity and mortality, constituting a major public health concern [10]. Advances in the treatment and prevention of AF are needed to address its rising global prevalence and incidence in the coming decades. Therapies which directly target the mechanistic basis of AF in individual patients are currently lacking [11, 12]. Progress in AF treatment will depend upon advances in our understanding of the various mechanisms that underlie atrial arrhythmogenesis.

1.2.1 AF Mechanisms

AF is initiated by ectopic activity, oftentimes arising from the pulmonary veins (PVs). Ectopic activity occurs due to abnormal automaticity, early afterdepolarizations (EADs), or delayed afterdepolarizations (DADs). DADs in particular play an important role in AF initiation [13]. Ca^{2+} overloading due to atrial tachycardia leads

to an increase in spontaneous Ca^{2+} release during diastole, which is then extruded by NCX. DADs, the depolarizing currents generated by NCX, can trigger an AP if V_m rises above the threshold potential, promoting arrhythmia through rapid focal discharge or interaction with a vulnerable substrate. Upregulation of I_{NCX} in response to Ca^{2+} overloading worsens the situation, as it increases the likelihood of DADs triggering an AP [14].

Atrial tachycardia promotes the development of a vulnerable substrate by inducing electrical and structural remodeling of the atria. Downregulation of I_{CaL} and upregulation of K^+ currents result in APD shortening. Reduced I_{Na} and gap junctional coupling and increased interstitial fibrosis result in decreased CV. These changes promote AF by decreasing wavelength and allowing the atria to sustain more reentrant circuits [15]. The remodeling which promotes AF is in turn further induced by AF, leading to an increase in AF frequency and duration—thus the notion that "AF begets AF". Clinically, this occurs as a progression from paroxysmal AF (lasting <7 days) to persistent or chronic AF (lasting ≥7 days) and finally to permanent AF.

1.2.2 AF Treatment

AF is treated with anticoagulants (to decrease the risk of stroke due to AF) and rate- or rhythm-control medications and interventions [11]. Rate control aims to reduce the frequency of ventricular activation during AF by targeting the AVN but does not address the abnormal rhythm within the atria. Rhythm control of the

atria can be attempted either pharmacologically or with catheter ablation. However, antiarrhythmic drugs used to treat AF can oftentimes promote arrhythmia in the ventricles. Catheter ablation is used to treat paroxysmal and persistent AF, through PV isolation and/or targeting of reentrant drivers, but the success of catheter ablation treatment is low for patients with longer-duration AF [16].

1.2.3 Alternans and AF

Clinical evidence suggests that atrial alternans may also play a role in the initiation of AF. APD alternans have been observed in the atria of cardioverted AF patients at slower pacing rates as compared to controls [17]. Narayan *et al.* reported that alternans always occurred before AF was induced at fast pacing rates [18]. Thus, the authors hypothesized that alternans may be an important clinical marker for AF risk. However, whether atrial alternans observed in patients play a significant role in arrhythmogenesis, and whether the underlying cause of alternans might present a promising target for novel therapies, is currently unknown.

1.3 Objectives

The goal of this research was to elucidate the mechanisms underlying alternans observed during atrial pacing in AF patients, and to determine the arrhythmogenic implications of such alternans at the organ scale. The specific aims of this work were:

- Specific Aim 1: Identify the cellular mechanisms responsible for the onset of APD alternans at slow pacing rates using computer models of human atrial tissue and cells.

- Specific Aim 2: Evaluate the effect of elevated alternans propensity on arrhythmia vulnerability due to ectopic beats in an anatomically realistic human atria model.

- Specific Aim 3: Assess differences in arrhythmia complexity and persistence due to elevated alternans propensity in the human atria model.

Chapter 2

General Methods

2.1 Mathematical Modeling

Mathematical modeling enables the study of cardiac electrophysiology at high spatiotemporal resolution. By integrating the complex interactions that occur at multiple scales of biology, computer simulations enhance our understanding of normal cardiac function and disease mechanisms. Cardiac modeling has a rich history and has undergone major advances in recent years [19]. The basic principles and techniques involved in cardiac modeling are outlined in the following sections.

2.1.1 Cell Membrane Kinetics

Hodgkin and Huxley pioneered the first mathematical model of an excitable cell membrane in 1952 [20]. In their model of the squid giant axon membrane, total

membrane current is divided into capacitive and ionic components:

$$I_m = C_m \frac{dV_m}{dt} + I_{ion} + I_{trans} \tag{2.1}$$

I_m is the total membrane current density, C_m is the membrane capacitance per unit area, V_m is the transmembrane potential, I_{ion} is the ionic current density, and I_{trans} is the current density of a transmembrane stimulus. I_{ion} is composed of fast Na^+ current (I_{Na}), delayed rectifier K^+ current (I_{Kr}), and a background leak current (I_l). The ionic conductances of I_{Na} and I_{Kr} depend on gating variables whose opening and closing rates are functions of transmembrane potential (V_m). Hodgkin and Huxley's formulation of these currents was based on detailed experimental measurements using voltage clamping. When integrated numerically, their equations could accurately recapitulate action potentials (APs) in the squid giant axon.

The first model of a cardiac AP, developed by Denis Noble in 1962, was based on this Hodgkin-Huxley formalism [21]. The model included modifications of Hodgkin and Huxley's original equations and the addition of inward rectifier K^+ current (I_{K1}). Since then, as more experimental data has become available, cardiac AP models have been updated considerably to reflect the composition and kinetics of ionic currents in the heart [22]. These include L-type Ca^{2+} current (I_{CaL}), Na^+/Ca^{2+} exchanger (NCX) current (I_{NCX}), Na^+/K^+ pump current (I_{NaK}), and transient outward K^+ current (I_{to}). There are now a multitude of models available based on different animal species

and human data, as well as different cell types within the heart.

2.1.2 Modeling Calcium Handling

During a cardiac AP, cellular Ca^{2+} content changes as a result of I_{CaL} and I_{NCX}. Within the cardiomyocyte, Ca^{2+} cycles between the diad (junction), the sarcoplasmic reticulum (SR), and the cytoplasm. Cardiac AP models generally represent these as separate lumped compartments within the cell, each with its own distinct Ca^{2+} concentration and distribution of ionic currents. Some earlier models do not include representation of the diadic space. The SR may be further subdivided into junctional and network compartments, and the intracellular space may be subdivided into subsarcolemmal and cytosolic compartments. Simple diffusion of Ca^{2+} occurs between compartments not separated by membranes, and movement into and out of the SR occurs through ryanodine receptor (RyR2) and sarco/endoplasmic reticulum Ca^{2+}-ATPase (SERCA) fluxes.

2.1.3 Bidomain Representation

The bidomain equations treat the cardiac syncytium as two continuous conducting mediums that represent the intracellular and interstitial spaces [23]. Current flow within each domain depends on the intracellular and extracellular conductivity tensors ($\bar{\sigma}_i$ and $\bar{\sigma}_e$, respectively), which are anisotropic due to the fiber and laminar sheet

structure of the myocardium. Current flow between the domains is governed by I_m (see Eq. 2.1):

$$\nabla \cdot \bar{\sigma}_i \nabla \phi_i = \beta I_m \tag{2.2}$$

$$\nabla \cdot \bar{\sigma}_e \nabla \phi_e = -\beta I_m - I_e \tag{2.3}$$

$$V_m = \phi_i - \phi_e \tag{2.4}$$

ϕ_i and ϕ_e are the intracellular and extracellular potentials, respectively, β is the cellular surface-to-volume ratio, and I_e is the current density of an extracellular stimulus. The bidomain model assumes that there are no current sources or sinks in either domain and that no charge accumulation occurs at any point. An extracellular bath with conductivity σ_b may also be considered:

$$\nabla \cdot \sigma_b \nabla \phi_e = I_e \tag{2.5}$$

The extracellular domain is assumed to be continuous with any surrounding bath, and no current flux occurs at the boundaries of the intracellular and extracellular domains. If the extracellular field is not being considered, or if the ratio of $\bar{\sigma}_i$ to $\bar{\sigma}_e$ is constant, then the bidomain equations can be simplified to the monodomain equation:

$$\nabla \cdot \bar{\sigma}_m \nabla V_m = \beta I_m \tag{2.6}$$

where $\bar{\sigma}_m$ is the monodomain conductivity tensor.

2.2 Finite Element Method

The bidomain equations can be solved numerically using a finite element approach. Tissue or organ geometry is discretized into a mesh composed of 3D elements connected at points called nodes. Fiber orientation is defined for each element, which determines $\bar{\sigma}_i$ and $\bar{\sigma}_e$ (or $\bar{\sigma}_m$ in the case of the monodomain equation). V_m, ϕ_e, and I_m are defined at every node (V_m and I_m only in monodomain), and equations are solved over each element. The bidomain equations are decoupled into a set of ordinary differential equations (Eq. 2.1), a parabolic partial differential equation (PDE) (Eq. 2.7), and an elliptic PDE (Eq. 2.8), which can be solved together by leapfrogging [24].

$$\nabla \cdot \bar{\sigma}_i \nabla V_m = -\nabla \cdot \bar{\sigma}_i \nabla \phi_e + \beta I_m \tag{2.7}$$

$$\nabla \cdot (\bar{\sigma}_i + \bar{\sigma}_e) \nabla \phi_e = -\nabla \cdot \bar{\sigma}_i \nabla V_m - I_e \tag{2.8}$$

Chapter 3

Disrupted calcium release as a mechanism for atrial alternans

This study has been published in *PLoS Computational Biology* [25].

3.1 Introduction

Atrial fibrillation (AF) is currently the most common cardiac rhythm disorder, posing a significant medical and economic challenge for the U.S. health care system [26, 27]. This burden is likely to increase as the population ages and AF prevalence rises [28]. Effective prevention and treatment of AF depends upon advances in our understanding of underlying disease mechanisms. Although several features of AF electrophysiological remodeling have been identified over the past decades [15, 29],

our knowledge about the arrhythmogenic substrate remains incomplete.

Beat-to-beat alternation in the shape of cardiac electrical signals, a phenomenon called alternans, has been observed in the atria of patients who experience AF, but the mechanism underlying the alternans is not known [17, 18, 30–32]. Narayan *et al.* reported differences in the rate dependence of action potential duration (APD) alternans in patients, with APD alternans occurring at pacing rates near rest in AF patients but only at fast pacing rates in controls [18]. Narayan *et al.* also found that APD alternans always preceded AF initiation, indicating that alternans may play an important role in establishing the arrhythmogenic substrate and creating vulnerability to AF. Thus, a better understanding of AF arrhythmogenesis will likely depend upon identification of the mechanism driving atrial alternans at heart rates near rest.

Interestingly, in AF patients the slope of the APD restitution curve was <1 during APD alternans onset at slow pacing rates. This suggests that a cellular mechanism other than voltage-driven instability underlies APD alternans at heart rates near rest [17]. Altered Ca^{2+} handling in atrial myocytes is known to play a crucial role in the generation of AF triggers and in AF maintenance [33, 34]. Ca^{2+} cycling instabilities have been shown to underlie ventricular alternans in heart failure [5, 35], as well as atrial alternans in several non-AF animal models [36–38]. However, it is unknown whether these represent a plausible mechanism for atrial alternans in AF patients, particularly at heart rates near rest. We therefore sought to determine, using a com-

puter model of human atrial tissue, whether Ca^{2+} handling abnormalities, or other electrophysiological changes that occur in AF, lead to APD alternans. We identified a critical change in the kinetics of the ryanodine receptor (RyR2) that was responsible for APD alternans onset at slower pacing rates, and subsequently aimed to elucidate the mechanistic relationship between this disruption in RyR2 kinetics and alternans onset. To this end, we employed single-cell clamping of ionic model parameters and iterated map analysis in order to dissect the mechanisms which drive alternans in atrial tissue, as well as to provide important insights into the pathophysiological changes that contribute to the development of alternans in AF patients.

3.2 Methods

3.2.1 Human AF tissue model

In order to investigate ionic mechanisms in human AF that contribute to the generation of atrial alternans at the tissue level, we created a computer model of human atrial tissue incorporating ionic remodeling associated with chronic AF (cAF). The atrial tissue preparation had dimensions of 0.33 mm $\times$ 0.33 mm $\times$ 9.9 mm (Fig. 3.1A), similar to the one used by Krummen *et al.* [39]. Human atrial cell membrane kinetics were represented by a modified version of the Grandi-Pandit-Voigt (GPV) human atrial action potential (AP) model [40], which we refer to as the GPVm model. Detailed explanation and justification of the GPVm model modifications are provided

in the supplement (Section 3.5.1.1). Different types of human atrial tissue were modeled individually as homogeneous tissue preparations, with each incorporating ionic changes appropriate for each tissue type. Both control and cAF-remodeled tissue, as well as left and right atrial tissue, were modeled using the parameter changes specified by Grandi *et al.* [40] (see Section 3.5.1.2). The isotropic bulk conductivity value for the tissue was tuned to produce a conduction velocity (CV) of 0.62 m/s in control tissue [41, 42]. When cAF ionic remodeling was incorporated, the same bulk conductivity value produced a CV of 0.59 m/s. These values are within the reported ranges for control and AF CVs [43].

3.2.2 Protocols for evaluating alternans in the human AF tissue model

We assessed alternans in the human AF tissue model by applying the clinical pacing protocol used by Narayan *et al.* to induce alternans in AF patients [18]. The tissue model was first initialized at all nodes with steady-state values from a single cell paced at 750-ms cycle length (CL). The tissue was then paced from the stimulus electrode (Fig. 3.1A) for 20 beats at 750-ms CL and then for 74 beats at each subsequent CL, starting from 500 ms and shortened in 50-ms steps to 300 ms, and then shortened in 10-ms steps, until loss of capture or conduction block occurred.

Voltage traces from the recording electrode (Fig. 3.1A) were analyzed for APD

alternans. APD was calculated as the time from maximal upstroke velocity to 90% repolarization of transmembrane potential (V_m) from phase 2 amplitude. Alternans magnitude was quantified as the mean magnitude of change in APD over the last 10 pairs of beats (11 beats total). APD alternans normalized magnitude (ANM), obtained by dividing the alternans magnitude by the mean APD over the last 10 beats, was used to compare alternans between cells of varying APD. Alternans onset CL was defined as the longest CL for which ANM was greater than 5% [18].

3.2.3 Sensitivity of alternans to ionic model parameters

To identify cellular changes which could account for the onset of alternans in AF patients at CLs of 300 ms to 500 ms [18], we explored how ANM varied in human AF tissue models of both the left atrium (LA) and right atrium (RA) as a result of changes in ionic model parameters. Of the 20 ionic model parameters tested, 10 were parameters altered in the GPVm model to represent cAF [40]; others were associated with L-type Ca^{2+} current (I_{CaL}), delayed rectifier K^+ current (I_{Kr}), sarcoplasmic reticulum (SR) uptake, or SR release (Table 3.1). We scaled parameter values one at a time to between 25% to 200% of the default LA or RA values specified by Grandi *et al.* [40]; for each parameter value within this range, simulations were conducted to determine the presence of alternans (282 simulations total). In AF patients, average

alternans onset CL was >300 ms [18], so pacing and alternans analysis was restricted to CLs $\geq$ 300 ms.

3.2.4 Clamping protocols

After identifying conditions under which APD alternans magnitude and onset CL matched clinical observations, we utilized two different clamping approaches in order to investigate the key cellular properties that gave rise to the alternans, as described below. Further explanation of the rationale behind these methods can be found in Section 3.3.

3.2.4.1 Ionic model variable clamps

To determine which human atrial ionic model variables drive the occurrence of alternans, we clamped individual ion currents and state variables in a single-cell model paced at a CL exhibiting alternans [35]. A model variable was clamped to its steady-state even or odd beat trace for the duration of 50 beats. This procedure was repeated for different model variables (membrane currents, SR fluxes, and all state variables excluding buffer concentrations), and APD alternans magnitude was quantified at the end of the 50 clamped beats. Additionally, the magnitude of alternans in $\Delta[Ca^{2+}]_i$ was quantified in the same manner as APD alternans magnitude, with $\Delta[Ca^{2+}]_i$ calculated as the difference between peak intracellular Ca^{2+} concentration ($[Ca^{2+}]_i$) during the beat and minimum $[Ca^{2+}]_i$ during the preceding diastolic interval (DI). Model

variables were considered critical for alternans if clamping them to either the even or odd beat reduced both APD and Ca^{2+} transient (CaT) alternans magnitudes by >99% of baseline [35].

3.2.4.2 Action potential clamp

To evaluate the Ca^{2+} cycling properties of the human atrial cell model under different pacing rates and parameter values, the following equation was used to clamp V_m to a generic atrial AP-like waveform so that comparisons between different conditions would not be influenced by variations in V_m:

$$V_m = \begin{cases} V_{max} + \frac{t}{\text{APD}} \left(V_{rest} - V_{max}\right) & n\text{CL} \leq t < n\text{CL} + \text{APD} \\ V_{rest} & n\text{CL} + \text{APD} \leq t < (n+1)\,\text{CL} \end{cases} \tag{3.1}$$

This approach has been used previously to investigate Ca^{2+} cycling properties in ventricular myocyte models [44, 45]. We set $V_{max} = 10$ mV, $V_{rest} = -75$ mV, and APD = 200 ms. CL ranged from 200 ms to 700 ms.

The AP clamp enabled evaluation of Ca^{2+} cycling stability in the human atrial cell model via an iterated map analysis [7, 44, 46]. We used a similar approach as Qu *et al.* [47], where SR load and total Ca^{2+} content of the cell are tracked from beat to beat. In our analysis, Ca^{2+} cycling stability depended upon three iterated map parameters: SR Ca^{2+} release slope (m), SR Ca^{2+} uptake factor (u), and cellular Ca^{2+}

efflux factor (κ). A detailed derivation of the iterated map stability criteria can be found in Section 3.5.1.4.

To compute the iterated map parameters, a single atrial cell was repeatedly clamped to the AP waveform until model variables reached steady state. Following this, SR Ca^{2+} concentration ($[Ca^{2+}]_{SR}$) was perturbed by $\pm 1\%$ at the beginning of an even beat, and total SR load, release, uptake, and cellular Ca^{2+} efflux per beat were recorded for the following 10 beats. For the Sato-Bers model, the first beat was excluded since it deviated noticeably from the linear response of later beats. This procedure was repeated starting with an odd beat so that data from a total of 40 beats were recorded (36 beats for the Sato-Bers model). Lastly, m, u, and κ were computed as the slopes of the linear least-squares fit of the data (see Section 3.5.1.4).

3.2.5 Numerical methods

Monodomain and ionic model equations were solved using the Cardiac Arrhythmia Research Package (CARP; Cardiosolv, LLC) [23]. Details on the numerical techniques used by CARP have been described previously [24,48]. A time step of 20 μs was used for all simulations.

Figure 3.1: Human atrial tissue model

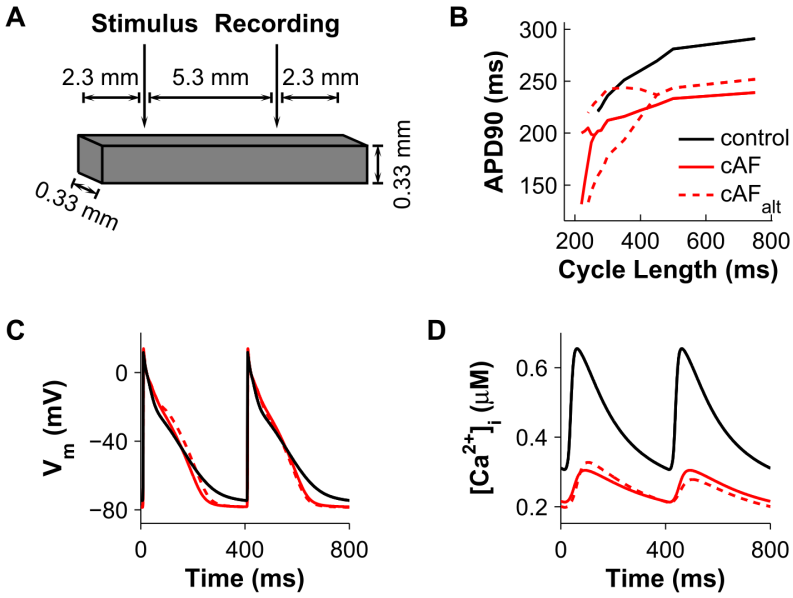

Tissue preparation setup and comparisons of control, cAF, and cAF_{alt} tissue during pacing. **A.** Atrial tissue mesh with stimulus and recording electrodes. **B.** APD restitution curves for control tissue (black), cAF-remodeled tissue [40] (red), and cAF_{alt} tissue with APD alternans onset and amplitude matching clinical data [18] (dotted red line). ki_{Ca} was reduced 50% in the cAF model to create the cAF_{alt} model. Action potentials (**C**) and Ca^{2+} transients (**D**) recorded from the last two beats at 400 ms pacing CL. Alternans is present in the cAF_{alt} tissue but not in control or cAF tissue.

3.3 Results

3.3.1 APD alternans in the human AF tissue model

The human atrial tissue model described in Section 3.2.1 was used to investigate ionic model parameters that contribute to the generation of atrial APD alternans at the tissue level. The sensitivity of APD alternans to 20 ionic model parameters (Table 3.1) was evaluated by varying parameters one at a time from LA cAF val-

ues [40] and applying the clinical pacing protocol used by Narayan *et al.* to induce APD alternans in AF patients [18] (see Section 3.2.2). For control, a model of normal human atrial tissue was also simulated. We then assessed the magnitude and onset pacing CL of APD alternans by analyzing voltage traces from the recording electrode (Fig. 3.1A), as outlined in Section 3.2.2.

In the control model, significant APD alternans did not occur before loss of capture at 260-ms CL (Fig. 3.1B). However, in the cAF-remodeled tissue preparation, significant APD alternans appeared at a CL of 240 ms (Fig. 3.1B). Varying RyR2 inactivation rate constant (ki_{Ca}) had the greatest effect on alternans onset CL in the human cAF-remodeled tissue (Fig. 3.2A). In fact, only reduction of ki_{Ca} resulted in alternans onset at CLs of 300 ms to 500 ms (Fig. 3.2B), matching alternans onset CLs observed in AF patients [18]. When other ionic model parameters were varied from their original cAF values, APD alternans either did not appear in the tissue model at CLs $\geq$ 300 ms (Fig. 3.2A, blue areas), appeared only at CLs $\leq$ 350 ms (Fig. 3.2A, red areas), or did not appear before loss of capture or conduction block occurred in the tissue (Fig. 3.2A, white spaces). These results suggest that altered RyR2 kinetics is the critical cellular component underlying the occurrence of APD alternans in AF patients at pacing rates near rest, and that ki_{Ca} plays a key role in this process.

We also tested whether differences between left and right atrial electrophysiology affect alternans susceptibility using a RA version of the cAF model [40] in tissue simulations. Results for RA tissue were very similar to those for LA tissue, demonstrating

Table 3.1: Ionic model parameters used in sensitivity analysis

Parameter	Description
$\bar{g}_{Na}$	maximum fast Na^+ current conductance
$\bar{g}_{NaL}$	maximum late Na^+ current conductance
$\bar{g}_{CaL}$	maximum L-type Ca^{2+} current conductance
τ_f	L-type Ca^{2+} current voltage-dependent inactivation time constant
τ_{fCa}	L-type Ca^{2+} current Ca^{2+}-dependent inactivation time constant
$\bar{g}_{K1}$	maximum inward rectifier K^+ current conductance
$\bar{g}_{Kr}$	maximum delayed rectifier K^+ current conductance
$\bar{g}_{Ks}$	maximum slowly activating delayed rectifier K^+ current conductance
$\bar{g}_{Kur}$	maximum ultra-rapid delayed rectifier K^+ current conductance
$\bar{g}_{to}$	maximum transient outward K^+ current conductance
$\bar{I}_{NCX}$	maximal Na^+/Ca^{2+} exchanger (NCX) current
k_s	SR Ca^{2+} release rate constant
ki_m	transition rate constant for RyR2
ko_m	transition rate constant for RyR2
ki_{Ca}	RyR2 inactivation rate constant
ko_{Ca}	RyR2 activation rate constant
k_{leak}	SR Ca^{2+} leak rate constant
$V_{maxSRCaP}$	V_{max} of SERCA pump
ec_{50SR}	EC_{50} for luminal Ca^{2+} dependence of RyR2
K_{mf}	K_m for SERCA pump in forward mode

Figure 3.2: Left atrial tissue parameter sensitivity analysis

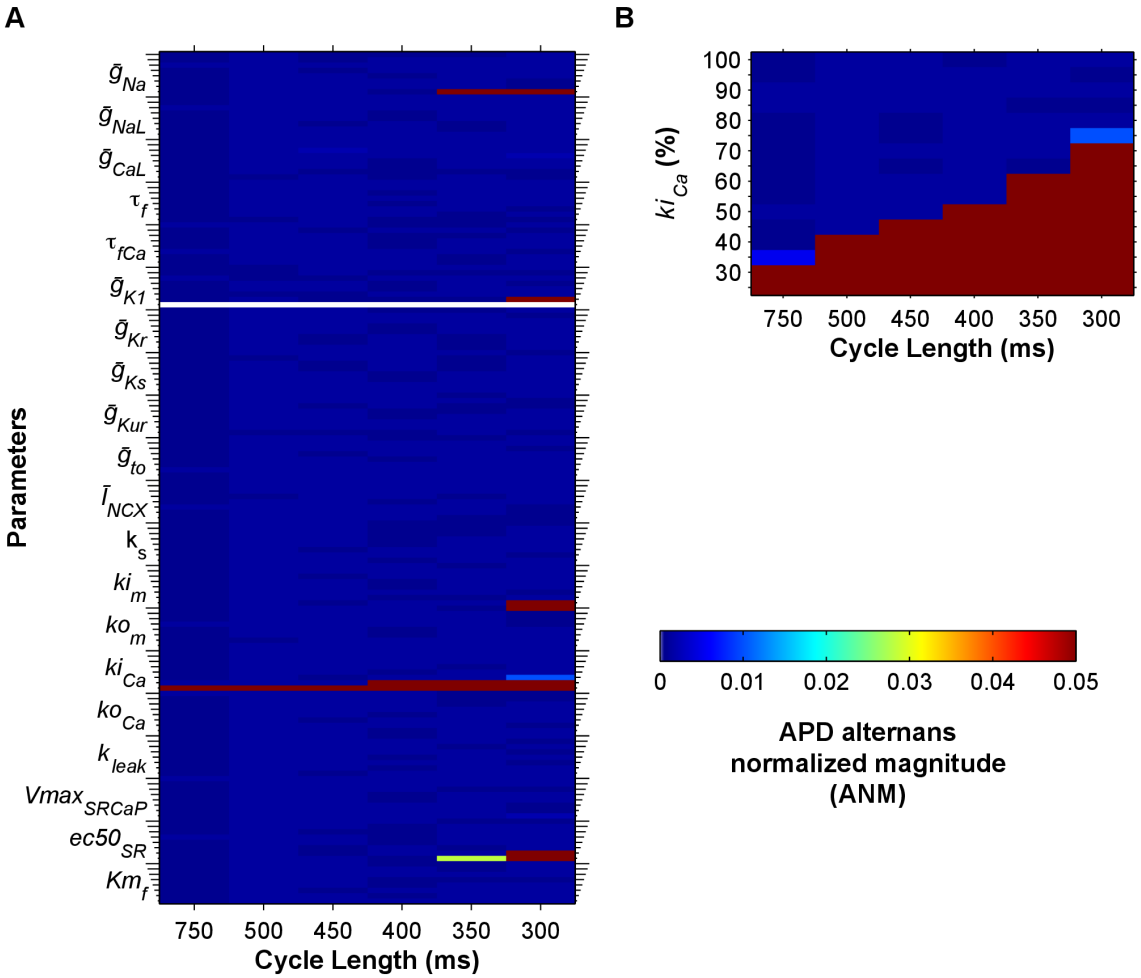

Parameter sensitivity analysis was performed in LA cAF tissue in order to identify ionic model parameters that influence alternans. **A.** Parameters were scaled one at a time between 25% (short ticks) and 200% (long ticks) of their cAF model values (25% increments). Only decreasing ki_{Ca} produced alternans at the longest CLs. **B.** ki_{Ca} was scaled between 25% and 100% in 5% increments, producing a range of APD alternans onset CLs between 300 ms to 750 ms. For (A) and (B), ANM is indicated by the colorbar (>0.05 considered significant). Simulations with loss of capture or conduction block are colored in white.

Figure 3.3: APD alternans onset comparison between model and patients

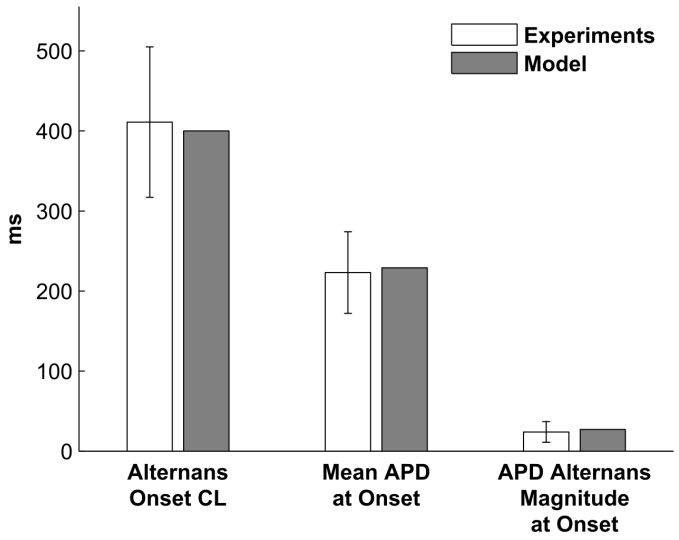

Comparison of alternans onset in persistent AF patients and in the cAF_{alt} tissue model. Mean $\pm$ SD alternans onset data during atrial pacing in persistent AF patients (white bars) were taken from Table 2 in Ref. [18]. When the cAF_{alt} tissue model was paced similarly, alternans onset CL, mean APD at onset, and APD alternans magnitude at onset were within one SD of clinical data (gray bars).

that modulation of ki_{Ca} could reproduce alternans observed at pacing rates near rest in both the LA and RA of AF patients [18] (Fig. 3.11).

When ki_{Ca} was decreased by 50% in the cAF model (we refer to this as the cAF_{alt} ionic model), APD alternans onset data from the human AF tissue model agreed well with data from persistent AF patients. Significant APD alternans began at 400-ms CL (Fig. 3.1B, dotted red line), mean APD at onset was 229 ms, and APD alternans magnitude at onset was 27 ms (Fig. 3.1C, dotted red line). These metrics were each within one standard deviation (SD) of clinical observations [18] (Fig. 3.3). The cAF_{alt} model also displayed noticeable alternans in $[Ca^{2+}]_i$ at the onset CL

(Fig. 3.1D). For both the cAF and cAF_{alt} models, mean APDs were shorter than in the control model (Fig. 3.1B–C), and diastolic and systolic $[Ca^{2+}]_i$ were lower than in control (Fig. 3.1D). At 400-ms CL in the cAF_{alt} model, on the odd (long) versus the even (short) beat (Fig. 3.4, blue vs. red), there was higher SR Ca^{2+} load before release (0.288 vs. 0.273 mM), higher peak RyR2 open probability (RyR_o) (9.0e−4 vs. 4.7e−4), a larger intracellular CaT amplitude ($\Delta[Ca^{2+}]_i = 0.13$ vs. 0.067 μM), similar I_{CaL} (integrated over one beat: 144 vs. 140 mC/F), and increased NCX current (I_{NCX}) (integrated over one beat: 98.4 vs. 74.5 mC/F). The positive coupling between V_m and Ca^{2+}, with I_{NCX} as the primary electrogenic current, is consistent with experimental findings [49]. Since the magnitude and onset of APD alternans in the cAF_{alt} model provided the best agreement with clinical APD alternans data (Fig. 3.3), we chose to use this model for subsequent investigations into the underlying causes of alternans occurrence.

3.3.2 SR Ca^{2+} release underlies alternans onset

Since APD alternans throughout the homogeneous cAF_{alt} tissue preparation was concordant and of similar magnitude (Fig. 3.12), electrotonic effects and CV restitution were excluded as factors influencing alternans. Indeed, APD and CaT alternans in the cAF_{alt} tissue model were very similar to alternans in the isolated single-cell cAF_{alt} model (Fig. 3.5, left column vs. Fig. 3.4, top row). We therefore concluded that cellular mechanisms gave rise to alternans in the cAF_{alt} tissue model and decided to

Figure 3.4: Alternans in cAF_{alt} tissue at the onset CL

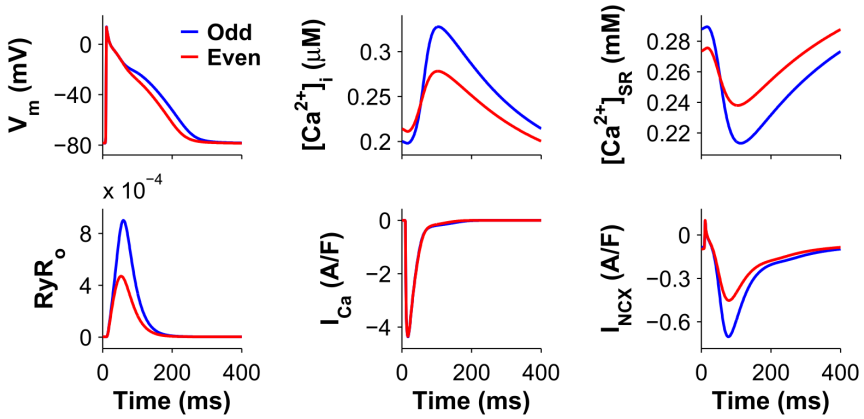

The odd (blue) and even (red) beats at the alternans onset CL (400 ms) are shown superimposed. Large Ca^{2+} release occurred during the long beat (blue traces). Top (left to right): transmembrane potential (V_m), intracellular Ca^{2+} concentration ($[Ca^{2+}]_i$), and SR Ca^{2+} concentration ($[Ca^{2+}]_{SR}$). Bottom (left to right): RyR2 open probability (RyR_o), L-type Ca^{2+} current (I_{CaL}), NCX current (I_{NCX}).

utilize single-cell simulations in order to investigate these mechanisms. We first used the ionic model variable clamping protocol described in detail in Section 3.2.4.1. The percent change in APD and CaT alternans magnitudes, when each ionic model variable was clamped to its trace from either the even (short) or odd (long) steady-state beat at the alternans onset CL (400 ms), are summarized in Figure 3.6. Variables which resulted in >99% reduction in APD and CaT alternans magnitudes for both even and odd beat clamps were considered essential for alternans.

Clamping V_m resulted in −61.8% and +6.6% change in CaT alternans magnitude for even and odd beat clamps, respectively, demonstrating that alternans was not voltage-driven (column 2 of Figs. 3.5 and 3.13). Clamping $[Ca^{2+}]_i$ enhanced APD

alternans (+55.2% and +75.8% for even and odd beat clamps, respectively, column 3 of Figs. 3.5 and 3.13). However, when SR Ca^{2+} ($[Ca^{2+}]_{SR}$) was clamped to either the even or odd beat waveforms, alternans in both APD and CaT was eliminated ($< -99\%$), demonstrating that alternans was driven by SR Ca^{2+} instability (column 4 of Figs. 3.5 and 3.13). In addition, four other variables could be clamped to the even or odd beat waveforms to eliminate APD and CaT alternans: RyR2 inactivated probability (RyR_i), RyR_o, junctional Ca^{2+} concentration ($[Ca^{2+}]_j$), and SR Ca^{2+} release flux ($J_{SRCa_{rel}}$) (Figs. 3.6, 3.14, and 3.15). All five of these variables were therefore critical for enabling alternans to occur at the onset CL. Furthermore, these variables directly impact SR Ca^{2+} release, implicating SR Ca^{2+} release as the underlying source of alternans in the cAF_{alt} model.

There were two ionic model components which greatly reduced but did not eliminate alternans when clamped: sub-sarcolemmal Ca^{2+} concentration ($[Ca^{2+}]_{sl}$) and sub-sarcolemmal NCX current (I_{NCXsl}). Clamping $[Ca^{2+}]_{sl}$ to the even beat eliminated all alternans; clamping to the odd beat greatly reduced APD and CaT alternans (-95.8% and -96.2%, respectively), although large alternation in SR load persisted (Fig. 3.6 and columns 1–2 of Fig. 3.16). Similarly, clamping $I_{NCX_{sl}}$ to the even beat waveform resulted in elimination of APD but not CaT alternans (+72.9%), while clamping to the odd beat waveform resulted in elimination of all alternans (Fig. 3.6 and columns 3–4 of Fig. 3.16). Hence, SR Ca^{2+}-driven instabilities produced alternans in Ca^{2+} cycling which positively coupled to voltage through $I_{NCX_{sl}}$ and $[Ca^{2+}]_{sl}$.

Figure 3.5: Clamping V_m and Ca^{2+} to odd beat waveforms

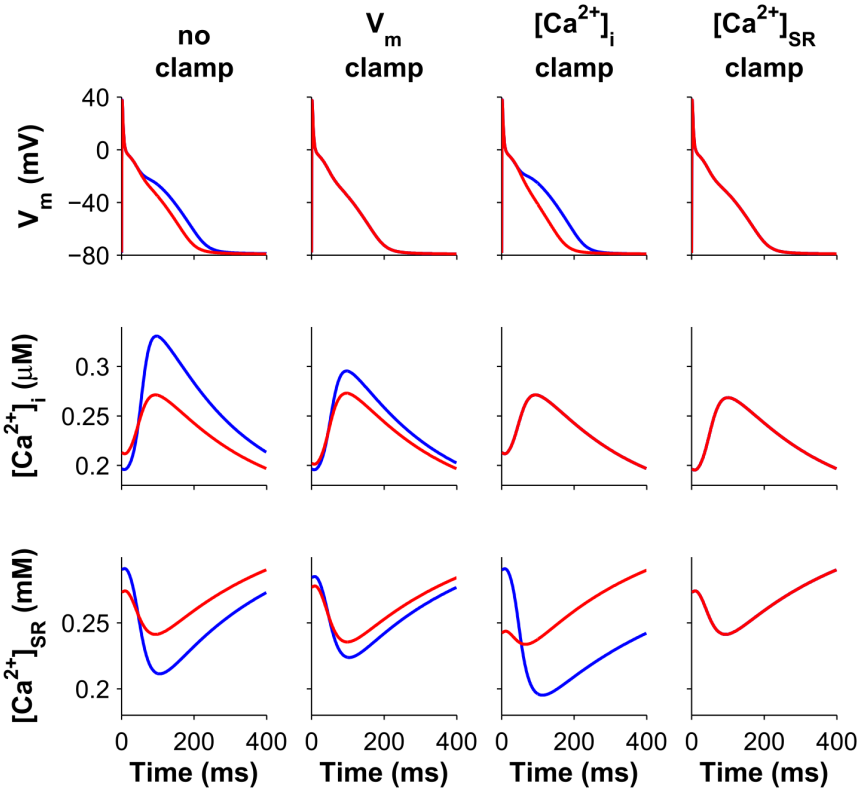

V_m or Ca^{2+} was clamped to odd beat waveforms in the cAF_{alt} single-cell model. Traces of transmembrane potential (V_m, row 1), intracellular Ca^{2+} concentration ($[Ca^{2+}]_i$, row 2), and SR Ca^{2+} concentration ($[Ca^{2+}]_{SR}$, row 3) from two consecutive beats are superimposed to show alternans between even (red) and odd (blue) beats. Column 1: the unclamped cAF_{alt} cell paced to steady state at 400 ms CL displayed alternans in V_m and Ca^{2+}. The red traces depicted in column 1 were used to clamp V_m (column 2), $[Ca^{2+}]_i$ (column 3), or $[Ca^{2+}]_{SR}$ (column 4). Alternans persisted when V_m or $[Ca^{2+}]_i$ was clamped, but clamping $[Ca^{2+}]_{SR}$ eliminated alternans.

Figure 3.6: Summary of ionic model variable clamping

Bar graphs show the percent changes in APD and CaT alternans magnitudes in the cAF_{alt} cell when ionic model variables were clamped to even or odd beat waveforms. Alternans were eliminated (>99% decrease in APD and CaT alternans magnitudes for both even and odd beat waveforms) only when SR release variables were clamped ($J_{SRCa_{rel}}$, RyR_o, RyR_i, $[Ca^{2+}]_{SR}$, and $[Ca^{2+}]_j$). Gating variable f (asterisk) displayed higher order instability when clamping to the even beat waveform, so the increase in alternans magnitude was considered infinitely large. Left column: SR fluxes and sarcolemmal currents. Right column: state variables.

(next page)

Figure 3.6: Summary of ionic model variable clamping

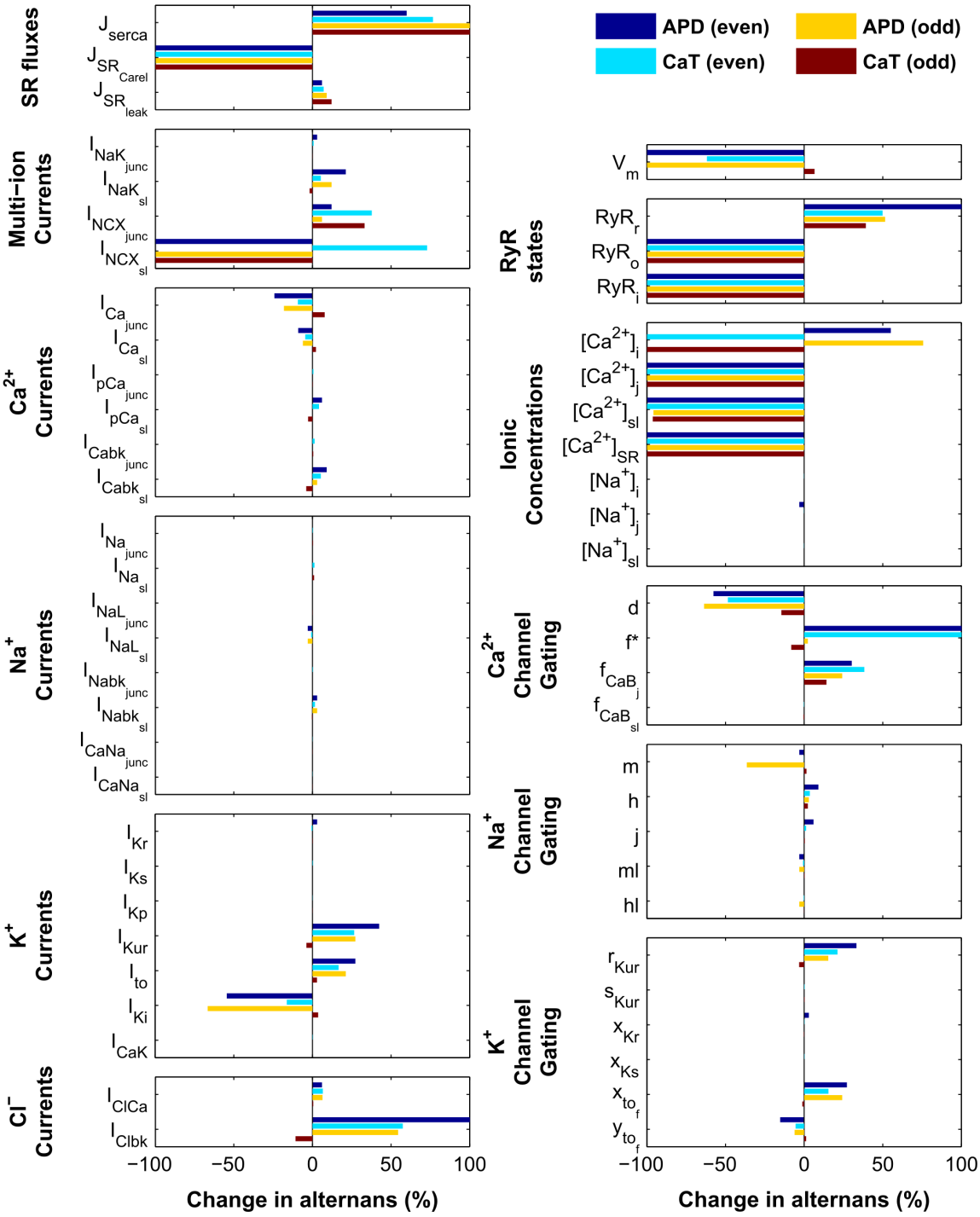

3.3.3 Steepening of the SR Ca^{2+} release slope results in alternans

Increased steepness of the SR release-load relationship is a well-known mechanism for CaT alternans [44, 50]. The importance of SR Ca^{2+} release variables for APD and CaT alternans, as demonstrated by the results in Figures 3.5, 3.6, 3.13, 3.14 and 3.15, led us to hypothesize that such a mechanism might give rise to Ca^{2+}-driven alternans in the cAF_{alt} model at pacing rates near rest. To test this, we compared the cAF and cAF_{alt} ionic models under AP voltage clamp conditions so that changes in CaT alternans would be due solely to changes in Ca^{2+} homeostasis rather than bidirectional coupling between V_m and Ca^{2+}. After clamping each ionic model at a CL of 400 ms until steady state was reached, we perturbed $[Ca^{2+}]_{SR}$ and tracked SR load and SR Ca^{2+} release on the subsequent clamped beats (see Section 3.2.4.2 for details). The SR release-load relationships for the cAF (black) and cAF_{alt} (red) ionic models are depicted in Fig. 3.7 (left column, row 1). The slope of the release-load relationship in the cAF_{alt} model (3.1) was much greater than the slope in the cAF model (1.7), confirming our hypothesis that differences between the cAF and cAF_{alt} ionic models led to a steepening of the SR Ca^{2+} release slope.

To better explain the differences between the cAF and cAF_{alt} ionic models that gave rise to different SR Ca^{2+} release slopes, we first compared $[Ca^{2+}]_{SR}$, RyR_o, $[Ca^{2+}]_j$, and cumulative Ca^{2+} release for the two models at steady state (Fig. 3.7, left

column, rows 2–5, solid lines). In the cAF_{alt} model, SR $[Ca^{2+}]$ at steady state was 19.7% lower than in the cAF model as a result of increased RyR2 opening (Fig. 3.7, left column, rows 2 and 3, red vs. black solid lines). Although this led to a 15.2% decrease in peak $[Ca^{2+}]_j$ in the cAF_{alt} model, the duration of the release event was prolonged (Fig. 3.7, left column, row 4, red vs. black solid lines). Consequently, though cumulative Ca^{2+} release in the cAF_{alt} model initially lagged behind, at $t \approx 90$ ms it actually surpassed the cumulative release in the cAF model, ultimately resulting in a 3.4% increase in total release by the end of the beat (Fig. 3.7, left column, row 5, red vs. black solid lines).

Figure 3.7: Effect of RyR2 inactivation on SR Ca^{2+} release slope

Left column: simulations using the original cAF (black) and cAF_{alt} (red) models. Right column: simulations in which the original RyR2 model, which included Ca^{2+}-dependent inactivation, was replaced with the Sato-Bers RyR2 model, which utilizes CSQN regulation instead (see Table 3.2). In the Sato-Bers model, the SR is divided into junctional (JSR) and network (NSR) compartments. Top row: Total Ca^{2+} released from the SR is plotted against SR Ca^{2+} load under AP voltage clamp conditions (CL = 400 ms). The line of best fit is also plotted, with its slope value (the SR Ca^{2+} release slope) shown next to the data points. (In column 2, the first beat was excluded.) Modulating RyR2 inactivation by reducing ki_{Ca} (left column) or k_{34} (right column) by 50% increased the SR Ca^{2+} release slope in both models. Rows 2–6: Traces from a similar set of AP voltage clamp simulations. After reaching steady state (solid lines), SR or NSR load was perturbed at the beginning of the beat by a large amount (+20 μM, dashed lines) to illustrate the changes affecting SR Ca^{2+} release slope. Row 2: SR or JSR Ca^{2+} ($[Ca^{2+}]_{SR/JSR}$). Row 3: RyR2 open probability. Row 4: junctional Ca^{2+} concentration. Row 5: total Ca^{2+} released. Row 6: the difference in total Ca^{2+} release between perturbed and unperturbed (steady state) simulations. Insets in column 2, rows 3–4 show traces from $t = 0$–50 ms.

(next page)

Figure 3.7: Effect of RyR2 inactivation on SR Ca^{2+} release slope

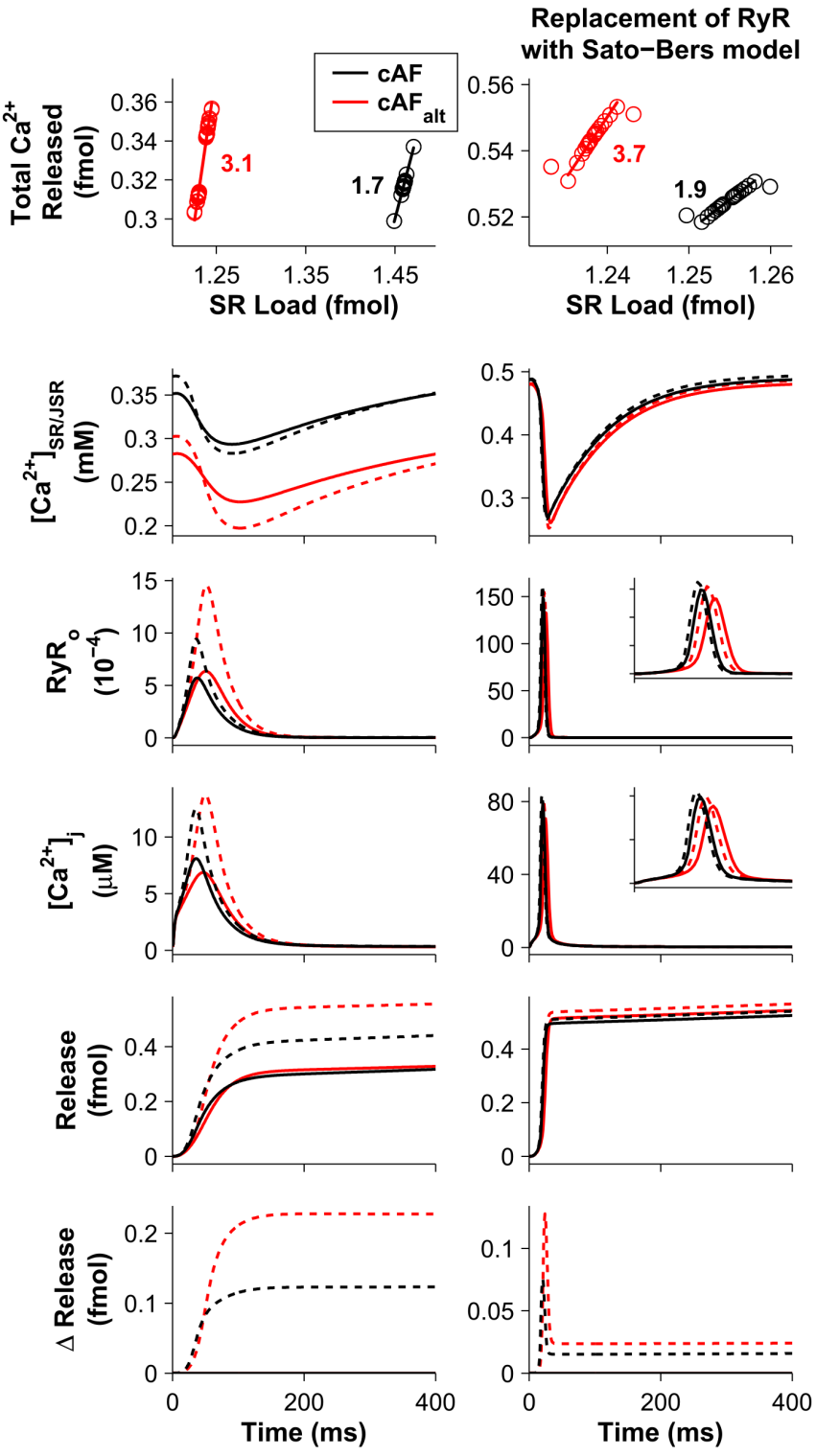

To illustrate how these differences between the cAF and cAF_{alt} ionic models impacted SR Ca^{2+} release slope, we applied a large perturbation to $[Ca^{2+}]_{SR}$ (+20 μM) at the beginning of a clamped beat and compared the unperturbed (steady state, solid line) and perturbed (dotted line) traces for each model (Fig. 3.7, left column, rows 2–6). Higher SR load at the beginning of the beat led to increased SR release flux due to luminal Ca^{2+} regulation of the RyR2 (causing more opening), as well as to the increased concentration gradient between the SR and junctional compartments. In both the cAF and cAF_{alt} models, these changes led to increased peak $[Ca^{2+}]_j$ (+54.4% and +100%, respectively) and RyR2 opening (+64.6% and +129%, respectively) as a result of more Ca^{2+}-induced Ca^{2+} release (Fig. 3.7, left column, rows 2–4). The positive feedback relationship between $[Ca^{2+}]_j$ and RyR2 opening was strong enough such that when SR load was increased (Fig. 3.7, left column, row 2, dotted vs. solid lines), this actually resulted in a lower minimum $[Ca^{2+}]_{SR}$ during release (−3.6% and −13.3% for cAF and cAF_{alt} models, respectively). However, the amount of positive feedback differed between the cAF and cAF_{alt} ionic models. Positive feedback amplifies changes in release inputs, such as SR load; therefore, in the cAF model, where $[Ca^{2+}]_j$ is higher and positive feedback is stronger, the increase in $[Ca^{2+}]_{SR}$ produced a slightly greater change in release (compared to the unperturbed, steady state simulation) during the rising phase of $[Ca^{2+}]_j$ ($t < 48$ ms) than in the cAF_{alt} model (Fig. 3.7, left column, row 6, black vs. red).

By contrast, termination of release occurs through a negative feedback process,

with RyRs inactivating upon the binding of junctional Ca^{2+}. Negative feedback attenuates changes in release so that robust, fast termination of release is achieved even when a disturbance (such as a transient increase in SR load) occurs. In the cAF_{alt} model, negative feedback is decreased both directly, via reduction of ki_{Ca}, and indirectly, via reduction in $[Ca^{2+}]_j$ that occurs as a result of decreased SR load. This causes prolongation of the Ca^{2+} release event and a larger peak $[Ca^{2+}]_j$ (Fig. 3.7, left column, row 4, red vs. black dotted lines). Consequently, when SR load was increased by the same amount in the cAF and cAF_{alt} models, although the cAF_{alt} model had a lesser initial change in release because of weaker positive feedback, it also had a greater final change in release, i.e. a steeper SR release-load relationship, because of weaker negative feedback (Fig. 3.7, left column, row 6, red vs. black).

The results in column 1 of Fig. 3.7 demonstrate how the steeper SR Ca^{2+} release slope in the cAF_{alt} ionic model (as compared to the cAF ionic model) depends upon RyR2 inactivation by junctional Ca^{2+}. However, recent work suggests that termination of release does not rely on direct Ca^{2+}-dependent inactivation of the RyR2 but rather on local SR Ca^{2+} depletion [51–54]. In order to test whether steepening of the SR Ca^{2+} release slope could occur in the cAF model by an alternative release termination mechanism, we implemented a version of the cAF model in which the RyR2 Markov model was replaced with that of Sato and Bers and the SR was divided into junctional (JSR) and network (NSR) compartments [55] (see Table 3.2 and Section 3.5.1.3). Termination of release in this alternative RyR2 model relies on

calsequestrin (CSQN) binding to the RyR2, which occurs as luminal [Ca^{2+}] decreases causing changes in RyR2 opening and closing rates.

The effects of decreased RyR2 termination in the Sato-Bers RyR2 model are shown in the right column of Fig. 3.7. When the CSQN-bound RyR2 closing rate k_{34} (analogous to the inactivation rate ki_{Ca} in the original model) is decreased from 100% to 50% (cAF_{alt}), steady-state Ca^{2+} concentrations change modestly as compared to the original RyR2 formulation (Fig. 3.7, black vs. red solid lines), but nevertheless display similar trends: SR [Ca^{2+}] decreases by 1.5% (vs. 19.7%, row 2), peak $[Ca^{2+}]_j$ is reduced by 10.5% (vs. 15.2%, row 4) and delayed, and total release increases by 3.6% (vs. 3.4%, row 5). When $[Ca^{2+}]_{NSR}$ is perturbed in the Sato-Bers models by +20 μM, Ca^{2+} release increases more in the cAF_{alt} model than in the cAF model (Fig. 3.7, right column, row 6, red vs. black dotted lines). Consequently, the SR Ca^{2+} release slope is steeper in the cAF_{alt} model (3.7 vs. 1.9, Fig. 3.7, right column, row 1). Thus, although changes in SR Ca^{2+} release slope in the original cAF model are caused by altered junctional Ca^{2+}-dependent inactivation, altered SR Ca^{2+}-dependent mechanisms of release termination can produce such changes in SR Ca^{2+} release slope as well.

Table 3.2: RyR2 and SR parameters

Parameters	Original cAF value [40]	Value used in Sato-Bers model [55]	Description
ko_{Ca} ($mM^{-2}ms^{-1}$)	30	-	RyR2 opening rate
K_u (ms^{-1})	-	15	CSQN-unbound RyR2 opening rate
K_b (ms^{-1})	-	0.015	CSQN-bound RyR2 opening rate
τ_b (ms)	-	0.164	CSQN binding time constant
τ_u (ms)	-	312	CSQN unbinding time constant
τ_{tr} (ms)	-	5	JSR refilling time constant
V_{SR} / V_{cell}	0.035	-	SR fractional volume
V_{JSR} / V_{cell}	-	0.0035	JSR fractional volume
V_{NSR} / V_{cell}	-	0.0315	NSR fractional volume
$V_{maxSRCaP}$ ($mM\,ms^{-1}$)	5.31e−3	5.04e−2	V_{max} of SERCA pump
k_s (ms^{-1})	25	134	SR Ca^{2+} release rate constant
$B_{max_{csqn}}$ (mM)	2.6	0.4	CSQN concentration
K_C (mM)	0.65	0.6	Ca^{2+}/CSQN dissociation constant

3.3.4 Iterated map analysis

Although SR Ca^{2+} release slope is an important component of Ca^{2+} homeostasis, other aspects of Ca^{2+} cycling, such as SR Ca^{2+} uptake, could also have a significant impact. In order to understand how both SR release and uptake contribute to CaT alternans onset at slow pacing rates in human cAF cells, we used an iterated map analysis for investigating Ca^{2+} cycling stability under AP voltage clamp conditions. Three factors affecting Ca^{2+} cycling stability were included in the analysis: SR release, SR uptake, and cellular Ca^{2+} flux across the sarcolemma. The latter factor was included because Ca^{2+} content in the human atrial cell model varied significantly enough to affect alternans threshold predictions.

For each version of the human atrial cell model (cAF and control), we calculated the SR Ca^{2+} release slope (m), the SR Ca^{2+} uptake factor (u), and the cellular Ca^{2+} efflux factor (κ) [7, 47] for a range of ki_{Ca} values and pacing rates and compared the value of m to the threshold for alternans. For a typical range of parameter values ($u + \kappa < 1$, see Section 3.5.1.4), the threshold value of m required for alternans is given by the following equation:

$$m_{thresh} = \frac{\kappa - 2}{2u + \kappa - 2} + 1 \tag{3.2}$$

Theoretical analysis predicts that the system is stable when $m < m_{thresh}$. Equation 3.2 is graphed for a range of κ values in Figure 3.8A–C (dotted lines). Each

curve represents the boundary between stable (no alternans) and unstable (alternans) Ca^{2+} cycling in the u–m plane for a particular value of κ. As κ increases (Fig. 3.8A–C, dark blue to dark red), the threshold curve steepens, indicating that increased Ca^{2+} extrusion from the cell has a protective effect, helping to restore Ca^{2+} content back to steady state following a perturbation. Thus, a higher value of m is required to reach alternans threshold for higher values of κ. Note that in this theoretical approach, increased Ca^{2+} efflux (κ) has the opposite effect as in Qu *et al.* [47], suppressing rather than promoting Ca^{2+} alternans.

The effects of changing CL and changing ki_{Ca} are explored for the cAF model in Fig. 3.8A. At the default ki_{Ca} value (100%), as CL is decreased from 700 ms to 200 ms (−10-ms increments), u decreases, m increases, and the system approaches the alternans threshold given by Equation 3.2. The change in κ values is non-monotonic, initially decreasing (orange to green) and then increasing (green to orange) as CL is decreased. However, the change in κ has a minimal effect at small u values, since the threshold curves for different κ values converge at $u = 0$. At CL < 220 ms, the cell begins to display alternans in Ca^{2+} cycling, coinciding with the iterated map parameter values residing very close to the theoretically predicted boundary given by Equation 3.2 (Fig. 3.8A, orange x's). When ki_{Ca} is set at 50% of the default cAF value (cAF_{alt} model), a similar trend is observed. However, the 50% ki_{Ca} cAF model reaches threshold at a lower pacing rate (CL = 390 ms for the 50% ki_{Ca} cAF model vs. 210 ms for the 100% ki_{Ca} cAF model, Fig. 3.8A, x's). This is primarily due to

m increasing as ki_{Ca} is decreased, illustrated by the trajectory of the system in the u–m plane as CL is held constant at 390 ms but ki_{Ca} is decreased from 100% to 50% (Fig. 3.8A).

We next performed the same iterated map analysis for the control atrial cell model with varying CL and ki_{Ca} values (Fig. 3.8B). When ki_{Ca} is at 100%, u decreases as CL is decreased. However, unlike in the cAF model, in the control case the value of m undergoes a net decrease as CL shortens from 700 ms to 200 ms. Ultimately, since both m and u decrease as CL is shortened, the control atrial cell (with ki_{Ca} at 100%) fails to reach threshold and remains in the stable, no alternans region. This suggests that alternans in control patients, which occur at CLs $<$250 ms [18], are driven by voltage rather than Ca^{2+}. As in the cAF model, the alternans threshold CL in the control model can be adjusted by modulating the value of ki_{Ca} (Fig. 3.8B, CL = 390 ms). However, in the control model, ki_{Ca} must be decreased much more than in the cAF model in order to reach m_{thresh} at a CL of 390 ms (ki_{Ca} reduced to 16% vs. 50%). The need for dramatic and possibly unrealistic reductions in ki_{Ca} to produce alternans at slow rates in control is consistent with the absence of alternans observed in control patients at CLs $\geq$ 250 ms [18].

To explain the difference in Ca^{2+} cycling properties of the cAF and control models, we examined the effects of cAF cellular remodeling on iterated map parameters. Stochastic ionic model parameter variation and regression analysis [56] (see Section 3.5.1.5) predicted that of the ten model parameters altered in the control

model to construct the cAF model, seven would have significant effects on alternans threshold CL (these are $\bar{g}_{CaL}$, ko_{Ca}, $\bar{g}_{Kur}$, $\bar{I}_{NCX}$, $\bar{g}_{to}$, $\bar{g}_{K1}$, and $\bar{g}_{Na}$, see Fig. 3.17). Of these seven parameters, three are involved in Ca^{2+} handling: maximum L-type Ca^{2+} current conductance ($\bar{g}_{CaL}$), RyR2 activation rate constant (ko_{Ca}), and maximal NCX current ($Ibar_{NCX}$). The effects of changing these three parameters from control to cAF values is depicted sequentially in Fig. 3.8C: starting with the default values for the control cell at a CL of 390 ms, first $\bar{g}_{CaL}$ is decreased and then $\bar{I}_{NCX}$ and ko_{Ca} are increased to cAF values, resulting in an overall decrease in u and m. Finally, when ki_{Ca} is decreased to the cAF_{alt} value (50%), the large increase in m causes the system to reach m_{thresh} and alternate (Fig. 3.8C, red X). This illustrates why the control cell is less susceptible to CaT alternans than the cAF cell: at a given ki_{Ca} value and pacing rate, SR uptake efficiency (u) is higher in the control model, thus requiring a large increase in the pacing rate (which decreases u) and/or a large decrease in ki_{Ca} (which increases m) in order to reach m_{thresh}. Of the three cAF parameters which decrease u, however, $\bar{g}_{CaL}$ is the most important for alternans onset, since remodeling of $\bar{I}_{NCX}$ and ko_{Ca} decreases m, while remodeling of $\bar{g}_{CaL}$ increases m. When $\bar{g}_{CaL}$ is remodeled and $\bar{I}_{NCX}$ and ko_{Ca} remain at control values, only a 28% decrease in ki_{Ca} is required to reach m_{thresh} (Fig. 3.8C).

Figure 3.8: Iterated map analysis of Ca^{2+} cycling

For each panel, SR Ca^{2+} release slope (m) is plotted against SR Ca^{2+} uptake factor (u), with cellular Ca^{2+} efflux factor (κ) values indicated in the colorbar. The boundaries between stable (no alternans) and unstable (alternans) regions in the u–m plane are denoted by dashed lines for different values of κ (see Eq. 3.2). Circles and x's indicate the absence and presence of alternans, respectively. **A.** Results for the cAF model. CL is varied, from 700 ms to 200 ms for the 100% ki_{Ca} model and from 700 ms to 300 ms for the 50% ki_{Ca} model (i.e., the cAF_{alt} model), in −10-ms increments. At a CL of 390 ms, ki_{Ca} is scaled from 100% to 50% in −2% increments. **B.** Same as in panel (A), except that the control cell model is used, and ki_{Ca} is scaled from 100% to 16%. **C.** Starting with the control cell parameter values, maximum L-type Ca^{2+} current conductance ($\bar{g}_{CaL}$), maximal NCX current ($Ibar_{NCX}$), and RyR2 activation rate constant (ko_{Ca}) are sequentially scaled to cAF values, resulting in net decreases in m and u. Finally, ki_{Ca} is scaled to 50% (as in the cAF_{alt} model), and increases sufficiently to reach the alternans boundary (red X). If only $\bar{g}_{CaL}$ is decreased to the cAF value, then alternans threshold is achieved at a higher ki_{Ca} value (72%, green X).

(next page)

Figure 3.8: Iterated map analysis of Ca^{2+} cycling

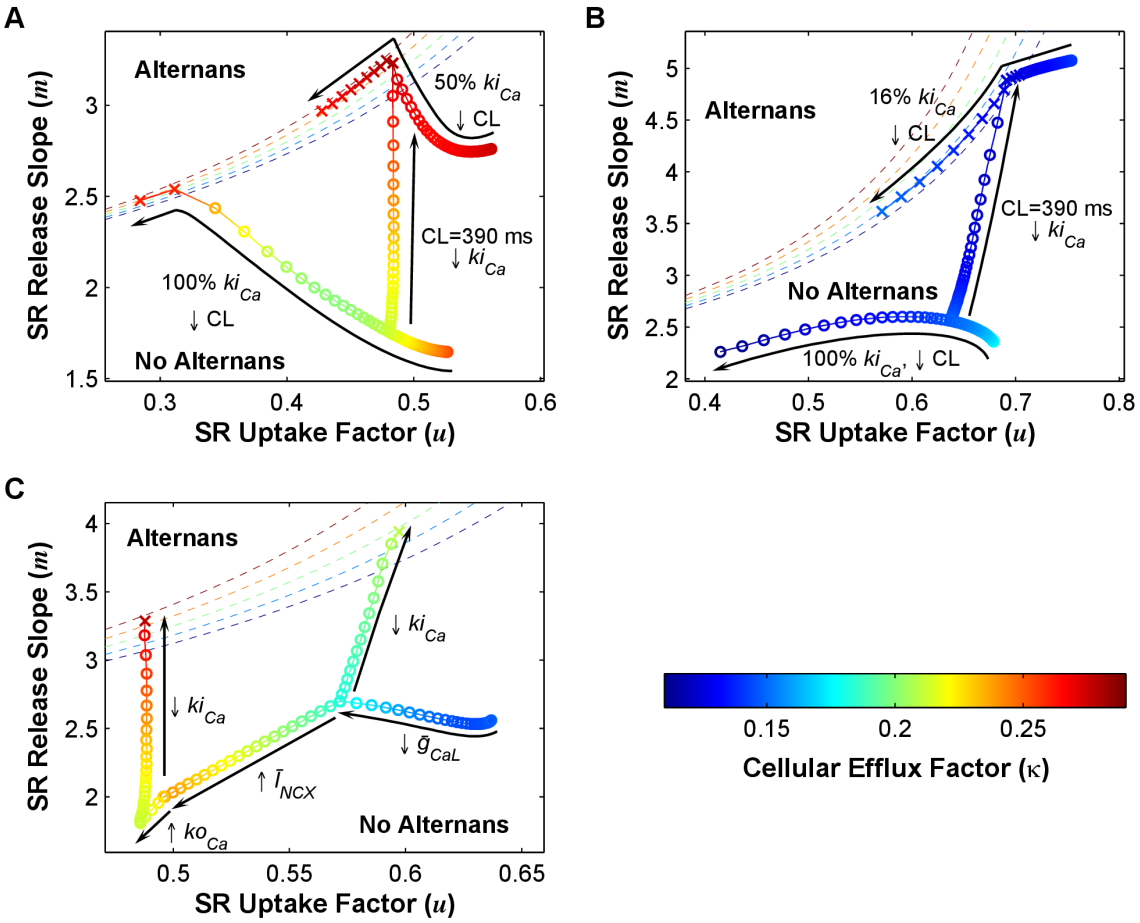

3.4 Discussion

3.4.1 Findings and significance

The first goal of this study was to identify the electrophysiological changes in human atrial cells that are responsible for the occurrence of APD alternans at heart rates near rest, as observed in AF patients. Using parameter sensitivity analysis, we found that of the 20 electrophysiological model variables tested, only changes in the RyR2 inactivation rate constant (ki_{Ca}) could produce APD alternans at relatively slow pacing rates in a tissue model of persistent/chronic AF. In particular, decreasing ki_{Ca} by 50% (the cAF_{alt} model) produced a good match to clinical data. We next aimed to provide mechanistic insight into why disruption of RyR2 kinetics, together with other electrophysiological changes occurring in AF, leads to alternans onset at pacing rates near rest. We established that alternans in the cAF_{alt} model at the onset CL were Ca^{2+}-driven rather than voltage-driven, and that they depended upon SR Ca^{2+} release. Furthermore, CaT alternans occurred in the cAF_{alt} model at relatively long CLs because of steep SR Ca^{2+} release slope and decreased SR Ca^{2+} uptake efficiency. Lastly, we demonstrated that the ability to generate alternans at slower pacing rates by modulating ki_{Ca} depended upon the negative feedback properties of SR Ca^{2+} release.

This study is the first to identify a possible mechanism for alternans occurring at slow heart rates in AF patients. Our novel findings show that alternans at slow

rates is Ca^{2+}-driven, brought about by AF-associated remodeling of the Ca^{2+} handling system in atrial cells. Clinical and experimental research has shown that atrial alternans is associated with disease progression in AF patients [18] and with increased AF susceptibility after myocardial infarction [57, 58] and atrial tachycardia [59, 60] in animal models. Additionally, CaT alternans have been studied in animal atrial myocytes [37, 38, 61] and in the intact atria of AF-prone mice [62]. However, the precise cellular mechanism underlying alternans at heart rates near rest in the remodeled human atria has not been previously identified, and a direct relationship between human AF and CaT alternans in the atria has not been established until now. Elucidating the mechanism driving alternans at slow rates is particularly important because APD oscillations appear to be closely linked to AF initiation [18]. If APD alternans play a direct role in AF initiation, the onset of alternans at slower pacing rates would indicate an increased susceptibility to arrhythmia in AF patients, consistent with clinical observations [18]. Identification of this mechanism would thus provide a significant scientific and clinical benefit, improving our understanding of arrhythmogenesis and aiding in the development of new targeted therapies for AF.

In this study, we demonstrate how different aspects of AF remodeling contribute to Ca^{2+}-driven alternans onset at slower heart rates using a theoretical analysis of Ca^{2+} cycling. This analysis allowed us to quantitatively assess CaT alternans threshold under AP voltage clamp conditions in a detailed electrophysiological model, providing valuable insights into the effects of AF electrophysiological remodeling on Ca^{2+} han-

dling and alternans. Furthermore, we identify a critical aspect of SR Ca^{2+} release—inactivation of the RyR2—which is necessary for CaT alternans to occur at slow heart rates. These findings extend mechanistic insight about proarrhythmic ventricular Ca^{2+} remodeling [35,63,64] to the atria and may inform new therapeutic strategies to target the RyR2 and suppress Ca^{2+}-driven alternans in the atria for the purposes of preventing or treating AF [62, 65].

3.4.2 RyR2 dysregulation in AF

The RyR2 has been the focus of several studies concerning trigger-mediated AF. In particular, disruption of RyR2 regulation has been shown to promote AF through increased RyR2 open probability, diastolic SR Ca^{2+} leak, and delayed afterdepolarizations [33, 65, 66]. Here we identify an additional pathological consequence of the disruption of RyR2 regulation in AF: Ca^{2+}-driven alternans. Similar to what has been demonstrated with regards to Ca^{2+} sparks and triggered activity [65], we found that CaT alternans is coupled to voltage primarily through upregulated I_{NCX}, thus driving the generation of APD alternans. RyR2's central role in both alternans and triggers has important clinical implications, given the proarrhythmic consequences of interaction between ectopic activity and the arrhythmogenic substrate created by voltage alternans [67]. New drug treatments to restore the normal function of the RyR2 and NCX, and thereby prevent arrhythmogenic triggers and alternans, have the potential to provide more effective alternatives to current AF drug therapies which

target voltage-gated ion channels and often have proarrhythmic side effects [65].

The signaling pathways involved in RyR2 dysfunction in AF have been the focus of much active research over the past several years [65, 66]. Possible molecular mechanisms which could account for reduced RyR2 inactivation include RyR2 hyperphosphorylation by CAMKII and PKA and dissociation of the RyR2 subunit FKBP12.6, which have been shown to increase RyR2 open probability and promote arrhythmia [68], although the exact role of these mechanisms in RyR2 dysregulation are still debated [69]. Calmodulin has also been shown to interact directly with the RyR2 to decrease its open probability [70]. Metabolic factors may play a role, since modulation of the RyR2 as a result of glycolytic inhibition has been linked to atrial alternans in non-AF animal models [36, 37, 61]. Such metabolic impairment is thought to contribute to profibrillatory remodeling in the atria [71–73]. The cAF_{alt} model, with its reduction in ki_{Ca}, can be considered a phenomenological representation of the various signaling pathway disruptions leading to alternans, which were not represented in the original cAF model. As more information becomes available, incorporation of these signaling mechanisms into computational models may provide additional insights into how reduction in RyR2 inactivation leads to Ca^{2+}-driven alternans at slow heart rates in AF patients.

3.4.3 The role of RyR2 refractoriness in CaT alternans

There is debate over whether CaT alternans depend primarily on SR Ca^{2+} load alternation or on RyR2 refractoriness [50, 67, 74]. Recent experiments [8, 38] and simulation studies [45, 75–77] have shown that RyR2 refractoriness can drive CaT alternans under conditions where near-identical SR loads produce different amounts of SR release. In some simulation studies, this phenomenon was restricted to limited parameter values, clamping conditions, and cycle lengths [75, 76], while in a more recent modeling study focusing on atrial cells, SR load-independent alternans occurred over a broad range of pacing rates when the number of T-tubules was reduced [77]. Of note is the fact that many of these studies [75–77] utilized the same RyR2 gating scheme as this current study, yet they identified various mechanisms for CaT alternans. This demonstrates that the relative importance of the various mechanisms, whether SR load-driven, RyR2 refractoriness-driven, or otherwise, is highly context-dependent.

Although exploring the issue of SR load versus RyR2 refractoriness was beyond the goals of the current study, our results suggest that in human cAF, both SR load alternation and RyR2 refractoriness are involved in alternans genesis at slower pacing rates. In our cAF_{alt} model, alternation in all SR Ca^{2+} release variables, including $[Ca^{2+}]_{SR}$, RyR2 open probability, and RyR2 inactivated probability, was necessary for alternans at the onset CL of 400 ms (Fig. 3.6). In addition, SR Ca^{2+} uptake flux

(J_{SERCA}) enhanced alternans when clamped (Fig. 3.6) and therefore suppressed alternans under normal pacing conditions, suggesting that SR load is indeed an important driver of CaT alternans in cAF and that upregulation of the sarco/endoplasmic reticulum Ca^{2+}-ATPase (SERCA) pump may be an important therapeutic strategy for diminishing alternans. We also showed that CaT alternans occurred in the cAF_{alt} model at slow pacing rates because decreased RyR2 inactivation resulted in steepening of the SR release-load relationship. Together, these results indicate that the interplay between SR load and RyR2 kinetics is responsible for alternans onset in human AF.

3.4.4 Other potential mechanisms for alternans susceptibility

The mechanisms for human atrial alternans susceptibility are likely to encompass a range of complex interactions at multiple scales of biology, which extend beyond the cellular-level mechanisms found here. In this study we examined the behavior of an atrial cell with well-developed T-tubules [40]. Research has shown that rat atrial cells have variable levels of T-tubule organization [78]. Such variation, if present in human atrial cells, would result in subcellular Ca^{2+} gradients which could make cells more susceptible to alternans [37, 79, 80]. Models of atrial myocytes incorporating detailed spatial descriptions [81] and local control of Ca^{2+} [13] will aid in future investigations

of the subcellular mechanisms of cAF-related alternans.

In addition, the complex structure of the atria, including its normal conduction pathways [41] and fibrotic remodeling in AF [82, 83], may promote heterogeneity and discordant alternans, which significantly affect alternans dynamics and reentry initiation [17, 84]. Consideration of these factors in the future will further enrich the mechanistic insight gained from this current study and will advance our understanding of the role that alternans play in AF arrhythmogenesis.

3.4.5 Limitations

In many cell models, the effective refractory period (ERP) is not consistent with ERP at the tissue level [85]. Electrotonic effects in tissue and the whole heart can shorten or lengthen APD depending on which structures and cell types are coupled to each other. Furthermore, alternans in single cell models may not be predictive of alternans in tissue, where conduction alternans can occur. This was the case for the control atrial tissue model, in which loss of capture occurred at a CL of 260 ms before reaching the very fast pacing rates at which APD alternans were observed in human control patients (CL = 218±30 ms) [18]. However, alternans onset at clinically observed rates occurred in the single-cell control model (200-ms CL, Fig. 3.18, black curve) and when ki_{Ca} was reduced by 5% (230-ms CL, Fig. 3.18, red curve). This suggests that the ionic model may not be well-constrained for tissue simulations at very fast rates. However, this issue did not affect the study of alternans onset at

slower pacing rates, as was observed in AF patients.

Our ionic model variable clamping protocol, which involved separately clamping the even or odd beat waveforms, was used to test for model variables which could robustly suppress alternans when clamped to either of two very different waveforms. An alternative approach would be to clamp model variables to the single unstable, non-alternating waveform obtained using a control algorithm [86]. This approach would allow more precise assessment of fixed point stability, since clamping is done at the point of instability rather than during the bistable (alternans) endpoint. However, for the purposes of quantifying the most important variables influencing instability, the clamping protocol used in this study was sufficient to identify the central role of SR Ca^{2+} release, which was later confirmed through iterated map analysis.

Recent experimental evidence points towards local SR Ca^{2+} depletion, rather than Ca^{2+}-dependent RyR2 inactivation, as the main mechanism of SR release termination [51–54]. Although alternans in the cAF_{alt} model relied on Ca^{2+}-dependent RyR2 inactivation, other termination mechanisms which rely on SR Ca^{2+} (used in the Sato-Bers RyR2 model) may have similar effects on SR Ca^{2+} release slope and alternans susceptibility (Fig. 3.7, column 2). However, with the Sato-Bers RyR2 model, alternans and other complex oscillations began at the baseline pacing rate (750-ms CL, Fig. 3.19) and did not display the same rate dependence observed in patients [18]. In addition, large oscillations in CaT amplitude did not couple as strongly to voltage as with the original RyR2, and oscillations were also attenuated in tissue (Fig. 3.19).

Further work is needed to develop atrial cell models which incorporate current mechanistic understanding of SR Ca^{2+} release and which can also reproduce AF-related alternans rate dependence in tissue.

3.4.6 Conclusion

AF is associated with progressive changes in alternans onset in the human atria, with alternans occurring at slower heart rates as AF severity worsens. We found that the differences in alternans onset between AF and control patients could be accounted for by changes in the inactivation rate of the RyR2 in a model of human atrial cAF-remodeled tissue. Single-cell simulations revealed that alternans at these slow heart rates were driven by abnormal Ca^{2+} handling and the development of CaT alternans, and that changes in CaT alternans threshold resulted from steepening of the SR Ca^{2+} release slope, decreased SR Ca^{2+} uptake efficiency, and decreased inactivation of the RyR2. These findings provide important insight into the mechanisms underlying proarrhythmic APD alternans occurring at slow heart rates in AF patients. Such insight may aid in the development of targeted therapies and new treatment strategies for AF in the future.

3.5 Appendix

3.5.1 Supplemental Methods

3.5.1.1 Modifications to the GPV model

The Grandi-Pandit-Voigt human atrial action potential model (GPV) model failed to propagate robustly when paced at faster rates (Fig. 3.9, black trace). We substituted fast Na^+ current (I_{Na}) kinetics of the original model with the formulation from the Luo-Rudy dynamic model (LRd) [87] to achieve normal propagation, as done previously [88] (Fig. 3.9, blue trace). Maximum fast Na^+ current conductance ($\bar{g}_{Na}$) was set to 14 mS/μF to reproduce maximum upstroke velocity (208 V/s) and action potential amplitude (105 mV) values reported previously [89, 90]. In addition, we reduced the number of state variables in the GPV model using a rapid equilibrium approximation for Ca^{2+} and Na^+ buffers with fast kinetics (Section 3.5.3.1). This decreased the computation time for tissue simulations by about 6X. The modified GPV model (GPVm) with LRd I_{Na} kinetics and fewer state variables was used for all simulations in this study unless otherwise indicated.

3.5.1.2 Inter-atrial heterogeneity and cAF remodeling

For the modified GPV model (GPVm) model, we implemented the changes described by Grandi *et al.* for the LA and RA [40]. In normal cells, maximum ultra-

Figure 3.9: Comparison of GPV and GPVm models

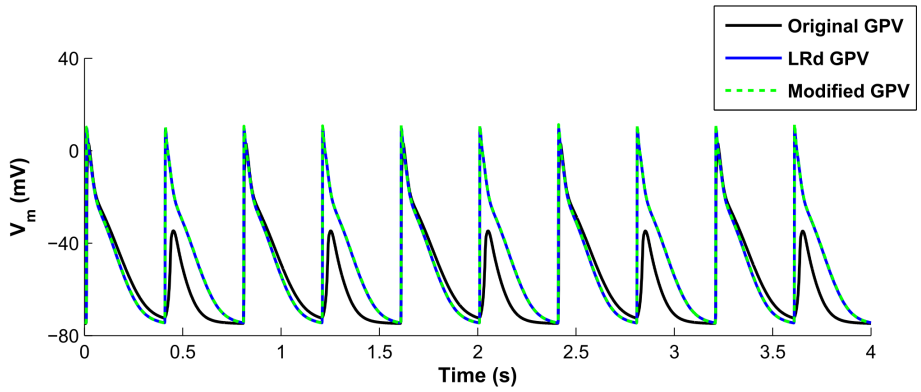

At 400-ms CL, the original GPV model did not propagate robustly in tissue (black line). When fast Na^+ current (I_{Na}) kinetics was replaced with the kinetics from the Luo-Rudy dynamic model (LRd), normal propagation occurred (blue line). Applying the fast equilibrium approximation to select buffers (Section 3.5.3.1) had a negligible effect on simulation results (dotted green line).

rapid delayed rectifier K^+ current conductance ($\bar{g}_{Kur}$) is increased by 20% in the RA as compared to the LA. In cAF cells, $\bar{g}_{Kur}$ and maximum transient outward K^+ current conductance ($\bar{g}_{to}$) are differentially downregulated from their normal levels, with $\bar{g}_{Kur}$ decreased by 45% and 55% and $\bar{g}_{to}$ decreased by 45% and 80% in the LA and RA, respectively. Additionally, modifications of the action potential under conditions of cAF included the following changes that occurred in both LA and RA: a 10% decrease in $\bar{g}_{Na}$, addition of a late component to the sodium current (I_{NaL}), a 50% decrease in $\bar{g}_{CaL}$, a 40% increase in $\bar{I}_{NCX}$, a 3-fold increase in ko_{Ca}, a 25% increase in SR Ca^{2+} leak, a 2-fold increase in maximum slow delayed rectifier K^+ current conductance ($\bar{g}_{Ks}$), and a 2-fold increase in maximum inward rectifier K^+ current conductance ($\bar{g}_{K1}$).

3.5.1.3 Sato-Bers RyR model implementation

Model parameters which were modified for implementation of the Sato-Bers RyR2 model [55] are listed in Table 3.2. The SR was divided into junctional (JSR) and network (NSR) compartments, the former of which contained the Ca^{2+} buffer CSQN. Equations for CSQN buffering in the Sato-Bers model were derived from Restrepo et al. [45] (Section 3.5.3.2). RyR2 equations were updated as described in Sato and Bers [55] (Section 3.5.3.3).

3.5.1.4 Iterated map derivation

Figure 3.10: Schematic of Ca^{2+} cycling used in iterated map analysis

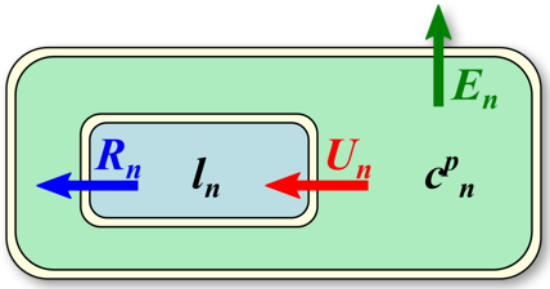

R_n is the total amount of SR Ca^{2+} release on beat n, which depends on SR load (l_n) (Eq. 3.3). U_n is the total amount of SR Ca^{2+} uptake on beat n, which depends on peak cytoplasmic Ca^{2+} ($c^p{}_n$) (Eq. 3.4). E_n is the net Ca^{2+} efflux from the cell on beat n, which depends on peak cytoplasmic Ca^{2+} ($c^p{}_n$) (Eq. 3.7).

We used an iterated map analysis to derive Ca^{2+} cycling stability criteria. For small SR load perturbations near steady state, total SR release (R_n) and uptake (U_n)

on each beat changed linearly from beat to beat [7, 44]:

$$\Delta R_n = m\Delta l_n \tag{3.3}$$

$$\Delta U_n = u\Delta {c^p}_n \tag{3.4}$$

m is the SR Ca^{2+} release slope, u is the SR Ca^{2+} uptake factor, and Δl_n and $\Delta {c^p}_n$ are the changes in total SR load and peak cytoplasmic Ca^{2+}, respectively, from beats $n-1$ to n. We did not consider Ca^{2+}-induced Ca^{2+} release (CICR) and SR leak separately since both were linearly dependent on SR load near steady state and their effects added linearly. Peak cytoplasmic Ca^{2+} was defined as:

$${c^p}_n = b_n - l_n + R_n \tag{3.5}$$

where b_n is the total Ca^{2+} content in the cell at the start of beat n. Equations 3.3–3.5 were used to construct the first mapping equation describing the change in SR load [7, 44, 47]:

$$\Delta l_{n+1} = \Delta l_n - m\Delta l_n + u\left(\Delta b_n - \Delta l_n + m\Delta l_n\right) \tag{3.6}$$

Note that we did not assume Δb_n to be zero. We also incorporated a new equation for net Ca^{2+} efflux from the cell (E_n), which depended linearly on peak cytoplasmic

Ca^{2+} for small perturbations near steady-state:

$$\Delta E_n = \kappa \Delta {c^p}_n \tag{3.7}$$

κ is the sarcolemmal Ca^{2+} efflux factor. Equations 3.3, 3.4, and 3.7 were used to find the linear least squares fit values of m, u, and κ based on R_n, U_n, E_n, ${c^p}_n$, and l_n.

The Ca^{2+} efflux term (Eq. 3.7) was used to construct the second mapping equation describing the change in total Ca^{2+} content [47]:

$$\Delta b_{n+1} = \Delta b_n - \kappa \left(\Delta b_n - \Delta l_n + m \Delta l_n \right) \tag{3.8}$$

Though iterated map analysis lacking this second mapping equation has been previously used [44], the addition of the second equation provided more accurate theoretical predictions of Ca^{2+} alternans thresholds in our simulations.

From Eq. 3.6 and 3.8, we obtained the following Jacobian matrix for the system [45, 47]:

$$\mathbf{J} = \begin{bmatrix} (1-m)(1-u) & u \\ \kappa(1-m) & 1-\kappa \end{bmatrix} \tag{3.9}$$

The criteria for stability are that both eigenvalues of the Jacobian have absolute value

less than 1:

$$\frac{1}{2}\left|(1-m)(1-u)-\kappa+1\pm\sqrt{((1-m)(1-u)-(1-\kappa))^2+4u\kappa(1-m)}\right|<1 \tag{3.10}$$

Under physiological conditions where the iterated map parameters are positive and u and κ are less than 1, the iterated map parameters must satisfy

$$m<\frac{\kappa-2}{2u+\kappa-2}+1 \quad , \quad 2u+\kappa<2 \tag{3.11}$$

and

$$m<\frac{1}{u+\kappa-1}+1 \quad , \quad u+\kappa>1 \tag{3.12}$$

for Ca^{2+} cycling to be stable.

3.5.1.5 Regression analysis

We used multivariable regression analysis methods from Sobie *et al.* to estimate the contribution of model parameters to the alternans threshold pacing CL [56]. Twenty model parameters (Table 3.1) were scaled (from control LA values) stochastically and independently according to a lognormal distribution with a median of 1 and $\sigma = 0.2$. A total of 500 sets of parameter scaling values were generated and used in single-cell simulations.

To determine the alternans threshold CL (output) for a given set of parameter

scaling values (input), each cell was first paced to steady state at a CL of 400 ms. Then CL was progressively increased or decreased by 1 ms every 100 beats until APD alternans ceased (alternans $\leq 1\%$) or began (alternans $> 1\%$), depending on whether alternans was present at a CL of 400 ms or not. Alternans threshold CL was defined as the shortest CL at which alternans did not occur. Any cell in which alternans persisted at CLs up to 750 ms or in which alternans was absent at CLs down to 100 ms was excluded from the analysis. Input and output matrices were log-transformed, then mean-centered and normalized by SDs (column-wise), before performing linear regression [56]. The regression coefficients obtained by this method indicate which parameters the model is most sensitive to with regards to alternans threshold CL, under assumptions of linearity. Linear regression was performed using MATLAB's LinearModel.fit function. Each parameter coefficient was considered significant if the p-value of its t-statistic was <0.05. To evaluate the predictive ability of the regression analysis, we multiplied the regression coefficients by parameter scaling values for the cAF model (log-transformed, mean-centered, and normalized) to obtain the predicted contribution of each parameter to changes in alternans CL [91].

3.5.2 Supplemental Figures

Figure 3.11: Right atrial tissue parameter sensitivity analysis

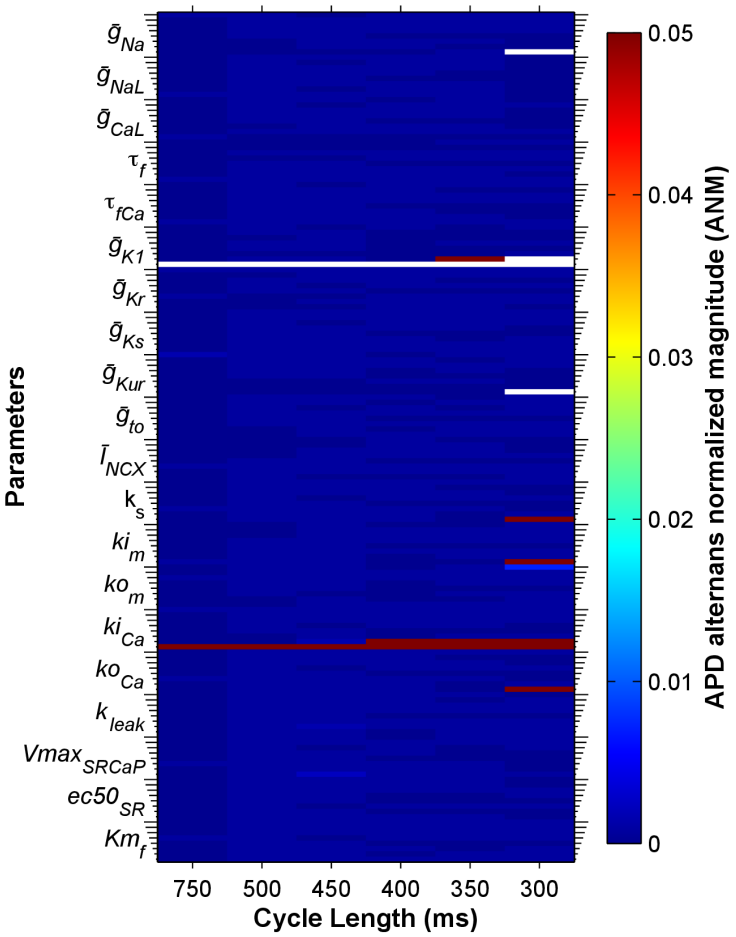

Parameter sensitivity analysis was performed in tissue with the right atrium version of the GPVm model incorporating cAF remodeling, in order to identify ionic model parameters that influence alternans. Parameters were scaled one at a time between 25% (short ticks) and 200% (long ticks) of their cAF model values (25% increments). Results were similar to those obtained with the LA version of the model (see Fig. 3.2A), with alternans occurring at the longest CLs only when ki_{Ca} was decreased. ANM is indicated by the colorbar (<0.05 considered significant). Simulations with loss of capture or conduction block are colored in white.

Figure 3.12: Concordant APD alternans in cAF_{alt} tissue

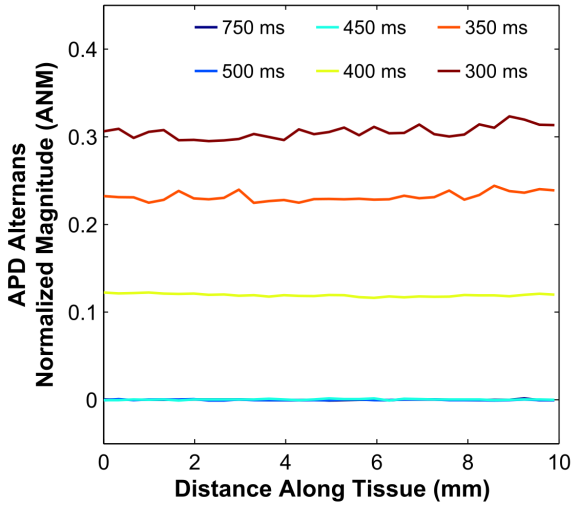

The tissue preparation was paced from the stimulus electrode (see Fig. 3.1A), and APD alternans normalized magnitude (ANM) was quantified at each CL for every node along the tissue. When significant alternans was present in the tissue (ANM > 0.05), all nodes had concordant alternans of similar magnitude.

Figure 3.13: Clamping V_m and Ca^{2+} to even beat waveforms

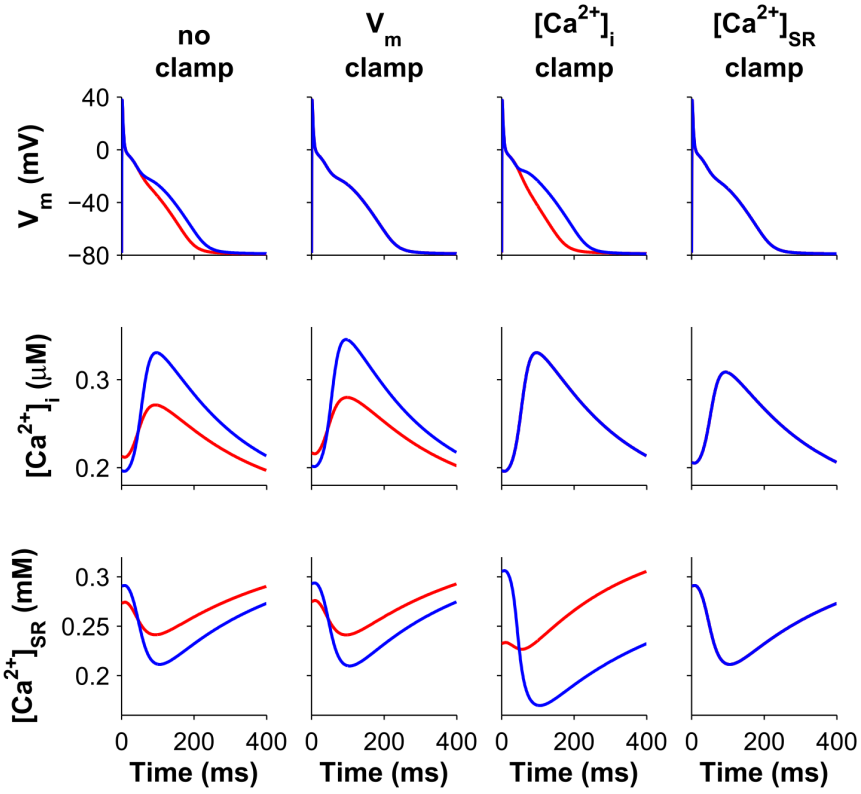

V_m or Ca^{2+} was clamped to even beat waveforms in the cAF_{alt} single-cell model. Traces of transmembrane potential (V_m, row 1), intracellular Ca^{2+} concentration ($[Ca^{2+}]_i$, row 2), and SR Ca^{2+} concentration ($[Ca^{2+}]_{SR}$, row 3) from two consecutive beats are superimposed to show alternans between even (red) and odd (blue) beats. Column 1: the unclamped cAF_{alt} cell paced to steady state at 400 ms CL displayed alternans in V_m and Ca^{2+}. The blue traces depicted in column 1 were used to clamp V_m (column 2), $[Ca^{2+}]_i$ (column 3), or $[Ca^{2+}]_{SR}$ (column 4). Alternans persisted when V_m or $[Ca^{2+}]_i$ was clamped, but clamping $[Ca^{2+}]_{SR}$ eliminated alternans.

Figure 3.14: Clamping SR Ca^{2+} release parameters to even beat waveforms

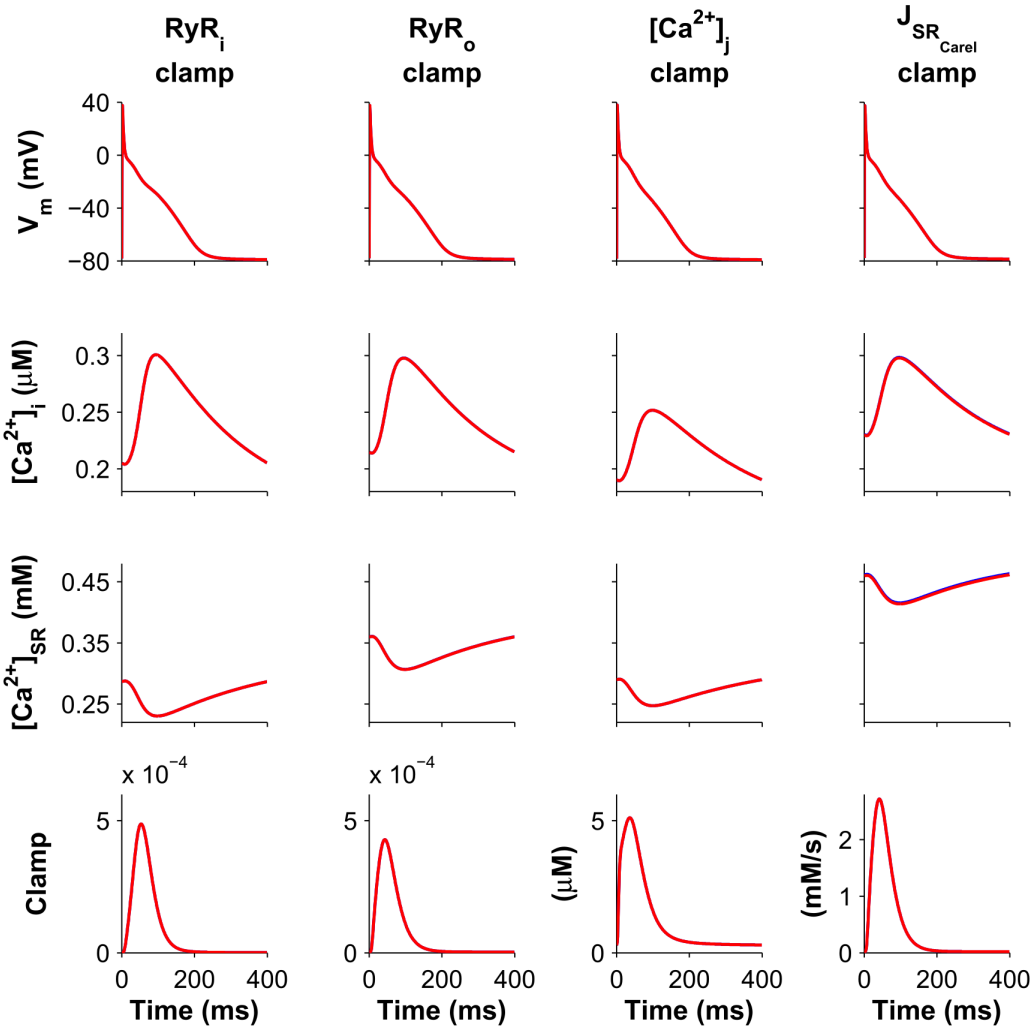

SR Ca^{2+} release parameters were clamped to even beat waveforms in the cAF_{alt} single-cell model. Traces of transmembrane potential (V_m, row 1), intracellular Ca^{2+} concentration ($[Ca^{2+}]_i$, row 2), and SR Ca^{2+} concentration ($[Ca^{2+}]_{SR}$, row 3) from two consecutive beats are superimposed to show alternans between even (red) and odd (blue) beats. Traces from the even beat at 400 ms CL pacing were used to clamp the relevant variable and are shown in row 4. Clamping RyR2 inactivated probability (RyR_i, column 1), RyR2 open probability (RyR_o, column 2), junctional Ca^{2+} concentration ($[Ca^{2+}]_j$, column 3), or SR Ca^{2+} release flux ($J_{SRCa_{rel}}$, column 4) eliminated alternans in V_m and Ca^{2+}.

Figure 3.15: Clamping SR Ca^{2+} release parameters to odd beat waveforms

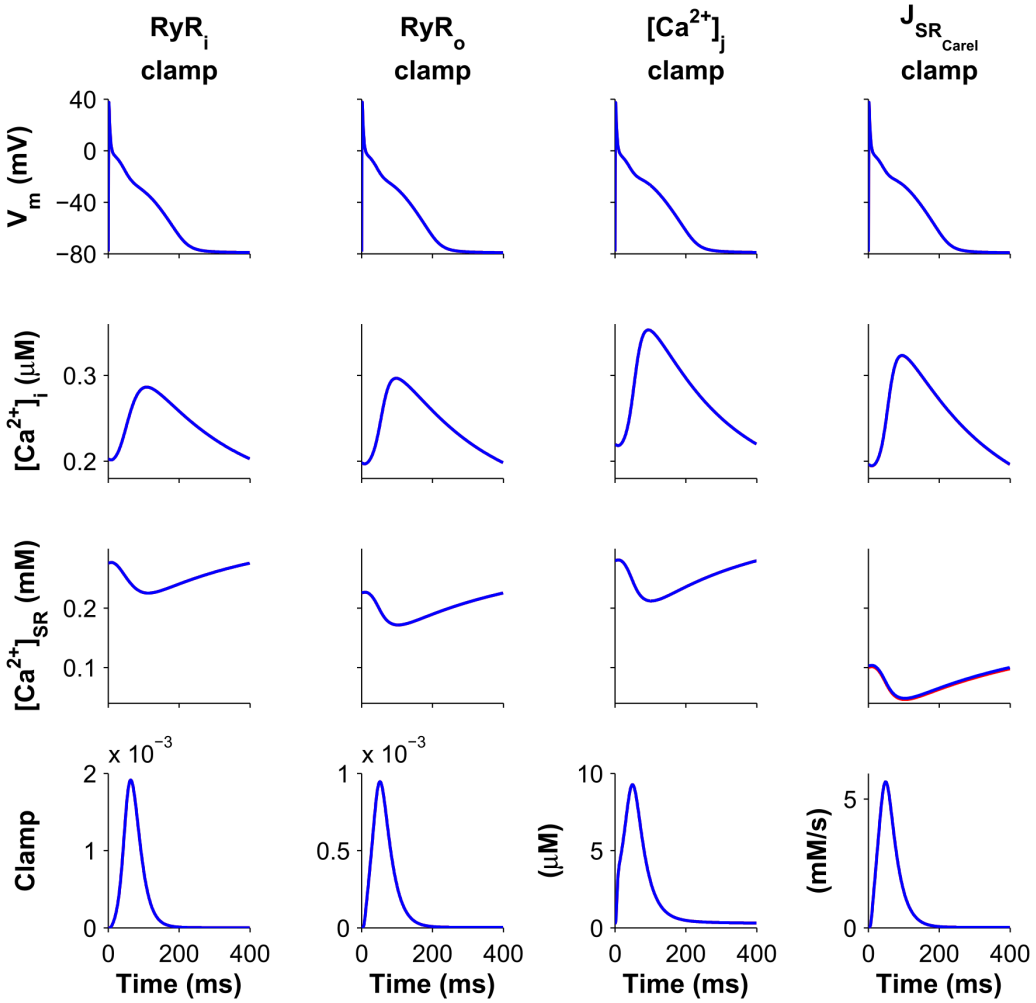

SR Ca^{2+} release parameters were clamped to odd beat waveforms in the cAF_{alt} single-cell model. Traces of transmembrane potential (V_m, row 1), intracellular Ca^{2+} concentration ($[Ca^{2+}]_i$, row 2), and SR Ca^{2+} concentration ($[Ca^{2+}]_{SR}$, row 3) from two consecutive beats are superimposed to show alternans between odd (red) and odd (blue) beats. Traces from the odd beat at 400 ms CL pacing were used to clamp the relevant variable and are shown in row 4. Clamping RyR2 inactivated probability (RyR_i, column 1), RyR2 open probability (RyR_o, column 2), junctional Ca^{2+} concentration ($[Ca^{2+}]_j$, column 3), or SR Ca^{2+} release flux ($J_{SRCa_{rel}}$, column 4) eliminated alternans in V_m and Ca^{2+}.

Figure 3.16: Clamping sub-sarcolemmal parameters

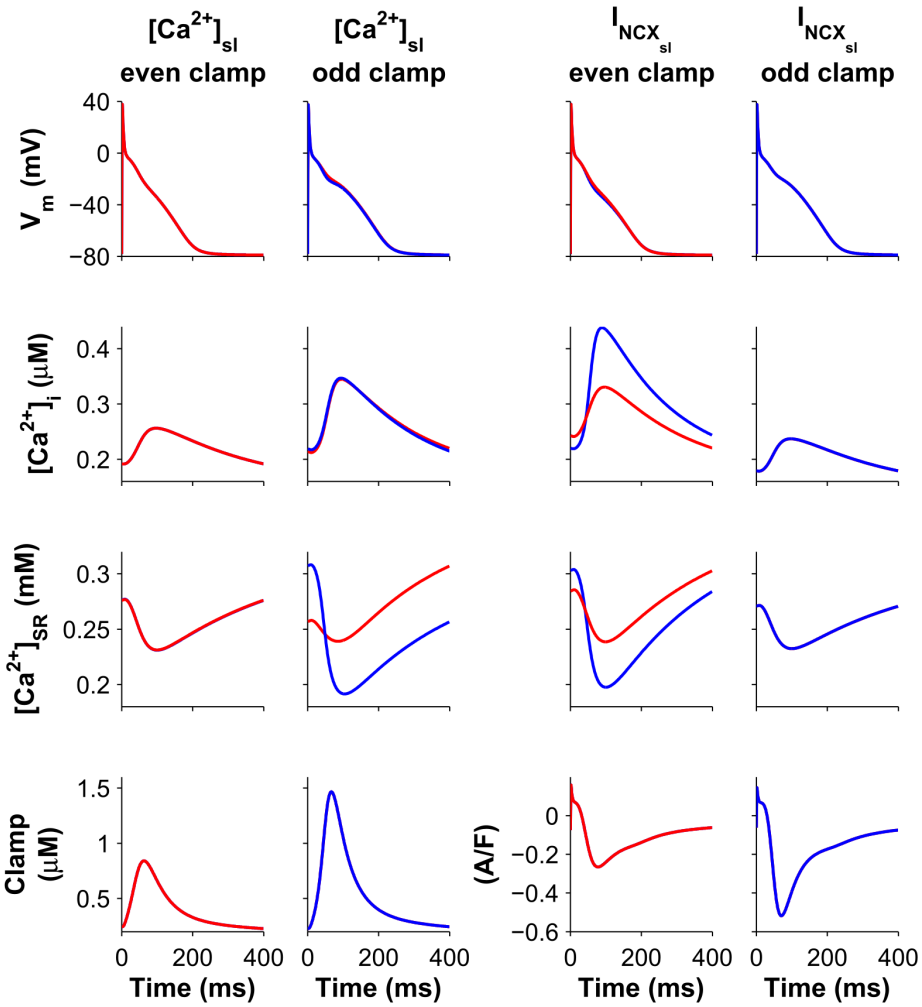

Sub-sarcolemmal parameters were clamped to even or odd beat waveforms in the cAF_{alt} single-cell model. Traces of transmembrane potential (V_m, row 1), intracellular Ca^{2+} concentration ($[Ca^{2+}]_{\text{i}}$, row 2), and SR Ca^{2+} concentration ($[Ca^{2+}]_{\text{SR}}$, row 3) from two consecutive beats are superimposed to show alternans between odd (red) and odd (blue) beats. Traces from the odd beat at 400 ms CL pacing were used to clamp the relevant variable and are shown in row 4. Clamping sub-sarcolemmal Ca^{2+} concentration ($[Ca^{2+}]_{\text{sl}}$) to the even beat (column 1) eliminated alternans in V_m and Ca^{2+}, but clamping $[Ca^{2+}]_{\text{sl}}$ to the odd beat (column 2) produced small alternans in V_m and $[Ca^{2+}]_{\text{i}}$ and large alternans in $[Ca^{2+}]_{\text{SR}}$. Clamping sub-sarcolemmal NCX current ($I_{NCX_{sl}}$) to the even beat (column 3) eliminated alternans in V_m but produced large alternans in $[Ca^{2+}]_{\text{i}}$ and $[Ca^{2+}]_{\text{SR}}$. Clamping $I_{NCX_{sl}}$ to the odd beat (column 4) eliminated alternans in V_m and Ca^{2+}.

Figure 3.17: Multivariable regression parameter sensitivity analysis

Multivariable regression was used to assess the contribution of ionic model parameters to alternans threshold CL. **A.** Bar graph of regression coefficient magnitudes. Twenty ionic model parameters were varied stochastically over 500 simulations to assess their effects on alternans threshold CL. Of the 500 simulations, 83 were excluded from the analysis because alternans threshold CL was below 100 ms or above 750 ms. Linear regression coefficients for each of the parameters are plotted in order of decreasing magnitude, with positive values plotted in red and negative values plotted in blue. Asterisks indicate $p < 0.05$ for the t-statistic. **B.** Bar graph of the predicted contribution of parameters to alternans threshold CL in the cAF-remodeled cell. Ten of the twenty parameters used in the regression analysis were altered from control values to represent cAF remodeling (increases and decreases indicated by upward and downward arrows, respectively). Parameters whose changes were predicted to increase (decrease) the alternans CL are plotted in red (blue). Some unaltered parameters had nonzero predicted contributions to alternans threshold CL due to nonzero sample means from the regression analysis. The alternans threshold CL predicted by regression analysis (245 ms) was very close to the actual alternans threshold CL determined by simulation (244 ms).

(next page)

Figure 3.17: Multivariable regression parameter sensitivity analysis

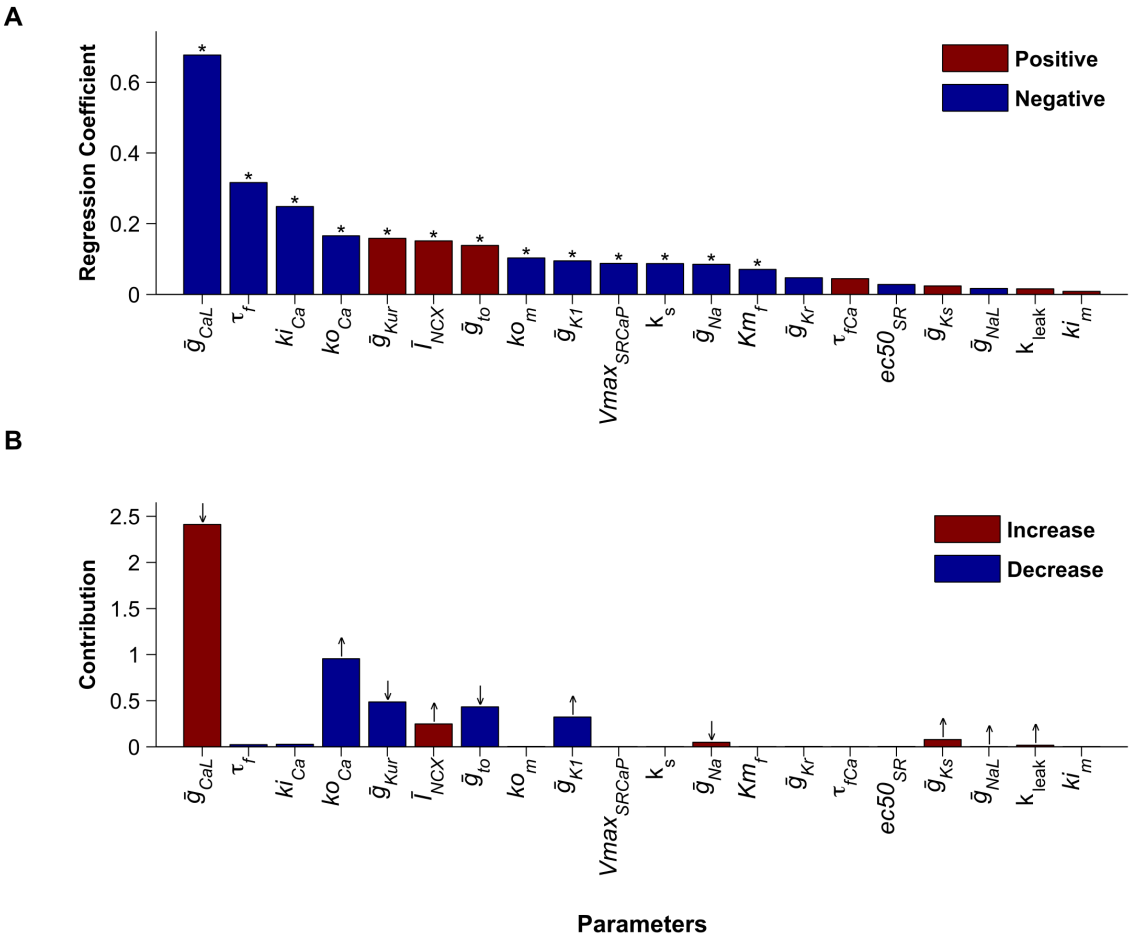

Figure 3.18: APD restitution in control single cell model

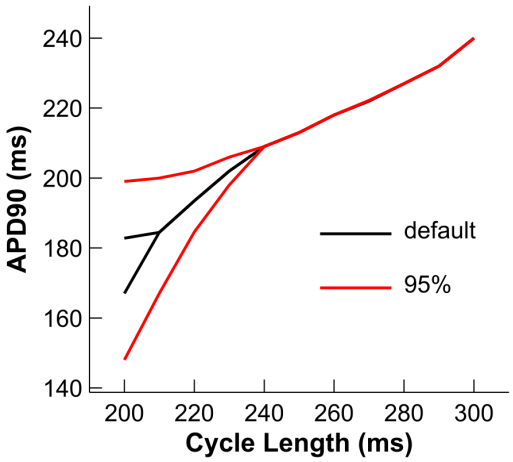

With default model parameter values, APD alternans occurred at 200 ms CL (black). When the RyR2 inactivation rate constant (ki_{Ca}) was reduced to 95%, alternans occurred at slightly longer CLs (red). These results were comparable to alternans onset data from control patients [18].

Figure 3.19: APD and CaT oscillations with Sato-Bers RyR2 model

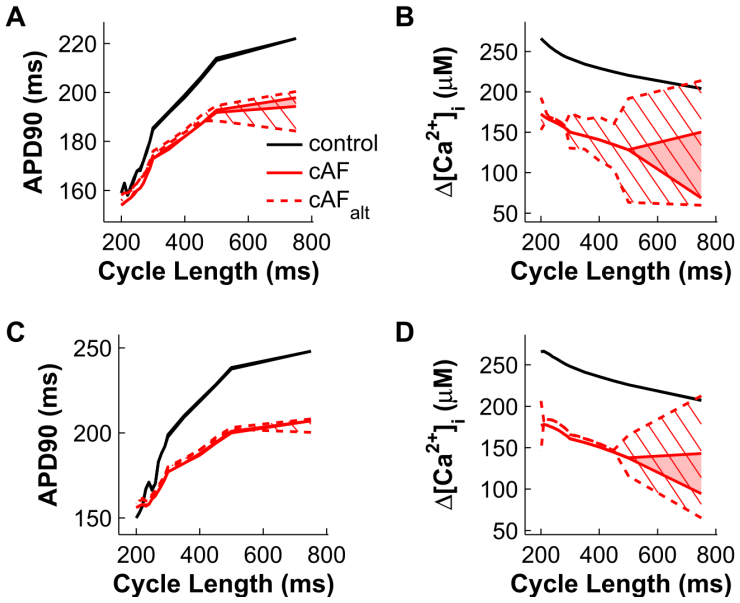

Control (black), cAF (red), and cAF_{alt} (dotted red line) versions of the model using the Sato-Bers RyR2 [55] were implemented in single cell (**A** and **B**) and in tissue (**C** and **D**). In the cAF_{alt} model, the CSQN-bound RyR2 closing rate (k_{34}) was decreased by 50%. APD (**A** and **C**) and CaT (**B** and **D**) restitution data are plotted showing the mean $\pm$ SD range (control, gray shading, not visible; cAF, pink shading; cAF_{alt}, red hatching). Oscillations in APD and CaT included but were not limited to alternans. Oscillations exhibited the reverse of the rate dependence observed in models using the original RyR2 formulation, with larger oscillations at longer CLs. APD oscillations in these models were diminished as compared to the original models (see Fig. 3.1), and both APD and CaT oscillations were attenuated in tissue.

3.5.3 Supplemental Equations

3.5.3.1 Rapid equilibrium approximation

Ca_i compartment (CaM and SRB):

$$J_{CaB_{cytosol}} = \dot{TnC_l} + \dot{TnC_{h_C}} + \dot{Myo_C} \tag{3.13}$$

$$\beta_{Ca_i} = \left(1 + \frac{B_{max_{CaM}} \frac{k_{off_{CaM}}}{k_{on_{CaM}}}}{\left(\frac{k_{off_{CaM}}}{k_{on_{CaM}}} + Ca_i\right)^2} + \frac{B_{max_{sr}} \frac{k_{off_{sr}}}{k_{on_{sr}}}}{\left(\frac{k_{off_{sr}}}{k_{on_{sr}}} + Ca_i\right)^2}\right)^{-1} \tag{3.14}$$

$$\dot{Ca_i} = \beta_{Ca_i}\left(-J_{SERCA}\frac{V_{SR}}{V_{myo}} - J_{CaB_{cytosol}} + \frac{J_{Ca_{slmyo}}}{V_{myo}}\left(Ca_{sl} - Ca_i\right)\right) \tag{3.15}$$

Ca_j compartment (SLL_j , SLH_j):

$$\beta_{Ca_j} = \left(1 + \frac{B_{max_{SL_{low_j}}} \frac{k_{\mathrm{off}_{sl_l}}}{k_{\mathrm{on}_{sl_l}}}}{\left(\frac{k_{\mathrm{off}_{sl_l}}}{k_{\mathrm{on}_{sl_l}}} + Ca_j\right)^2} + \frac{B_{max_{SL_{high_j}}} \frac{k_{\mathrm{off}_{sl_h}}}{k_{\mathrm{on}_{sl_h}}}}{\left(\frac{k_{\mathrm{off}_{sl_h}}}{k_{\mathrm{on}_{sl_h}}} + Ca_j\right)^2}\right)^{-1} \tag{3.16}$$

$$\begin{aligned}\dot{Ca_j} = \beta_{Ca_j}\Bigg(&-I_{Ca_{tot_{junc}}}\frac{C_m}{2FV_{junc}} + \frac{J_{Ca_{juncsl}}}{V_{junc}}\left(Ca_{sl} - Ca_j\right) \\ &+ J_{SR_{Ca_{rel}}}\frac{V_{sr}}{V_{junc}} + J_{SR_{leak}}\frac{V_{myo}}{V_{junc}}\Bigg)\end{aligned} \tag{3.17}$$

Ca_{sl} compartment (SLL_{sl} , SLH_{sl}):

$$\beta_{Ca_{sl}} = \left(1 + \frac{B_{max_{SL_{low_{sl}}}} \frac{k_{\mathrm{off}_{sl_l}}}{k_{\mathrm{on}_{sl_l}}}}{\left(\frac{k_{\mathrm{off}_{sl_l}}}{k_{\mathrm{on}_{sl_l}}} + Ca_{sl}\right)^2} + \frac{B_{max_{SL_{high_{sl}}}} \frac{k_{\mathrm{off}_{sl_h}}}{k_{\mathrm{on}_{sl_h}}}}{\left(\frac{k_{\mathrm{off}_{sl_h}}}{k_{\mathrm{on}_{sl_h}}} + Ca_{sl}\right)^2}\right)^{-1} \tag{3.18}$$

$$\dot{Ca_{sl}} = \beta_{sl}\left(-I_{Ca_{tot_{sl}}}\frac{C_m}{2FV_{sl}} + \frac{J_{Ca_{juncsl}}}{V_{sl}}\left(Ca_j - Ca_{sl}\right) + \frac{J_{Ca_{slmyo}}}{V_{sl}}\left(Ca_i - Ca_{sl}\right)\right) \tag{3.19}$$

Ca_{SR} compartment ($Csqn_b$):

$$\beta_{Ca_{SR}} = \left(1 + \frac{B_{max_{csqn}}\frac{k_{\text{off}_{csqn}}}{k_{\text{on}_{csqn}}}}{\left(\frac{k_{\text{off}_{csqn}}}{k_{\text{on}_{csqn}}} + Ca_{SR}\right)^2}\right)^{-1} \tag{3.20}$$

$$\dot{Ca_{SR}} = \beta_{Ca_{SR}}\left(J_{serca} - \left(J_{SR_{leak}}\frac{V_{myo}}{V_{sr}} + J_{SR_{Ca_{rel}}}\right)\right) \tag{3.21}$$

Na_j compartment (Na_{B_j}):

$$\beta_{Na_j} = \left(1 + \frac{B_{max_{Na_j}}\frac{k_{\text{off}_{Na}}}{k_{\text{on}_{Na}}}}{\left(\frac{k_{\text{off}_{Na}}}{k_{\text{on}_{Na}}} + Na_j\right)^2}\right)^{-1} \tag{3.22}$$

$$\dot{Na_j} = \beta_{Na_j}\left(-I_{Na_{tot_{junc}}}\frac{C_m}{2FV_{junc}} + \frac{J_{Na_{juncsl}}}{V_{junc}}\left(Na_{sl} - Na_j\right)\right) \tag{3.23}$$

Na_{sl} compartment ($Na_{B_{sl}}$):

$$\beta_{Na_{sl}} = \left(1 + \frac{B_{max_{Na_{sl}}}\frac{k_{\text{off}_{Na}}}{k_{\text{on}_{Na}}}}{\left(\frac{k_{\text{off}_{Na}}}{k_{\text{on}_{Na}}} + Na_{sl}\right)^2}\right)^{-1} \tag{3.24}$$

$$\dot{Na_{sl}} = \beta_{sl}\left(-I_{Na_{tot_{sl}}}\frac{C_m}{2FV_{sl}} + \frac{J_{Na_{juncsl}}}{V_{sl}}\left(Na_j - Na_{sl}\right) + \frac{J_{Na_{slmyo}}}{V_{sl}}\left(Na_i - Na_{sl}\right)\right) \tag{3.25}$$

3.5.3.2 Alternative CSQN buffering

$$\beta_{JSR} = \left(1 + \frac{B_{max_{csqn}} \left(K_c n + \frac{\partial n}{\partial Ca_{JSR}} \left(K_c + Ca_{JSR}\right)\right)}{\left(K_c + Ca_{JSR}\right)^2}\right)^{-1} \tag{3.26}$$

$$n = \hat{M} n_M + \left(1 - \hat{M}\right) n_D \tag{3.27}$$

$$\hat{M} = \frac{\left(1 + 8\rho B_{max_{csqn}}\right)^{\frac{1}{2}} - 1}{4\rho B_{max_{csqn}}} \tag{3.28}$$

$$\rho = \frac{\rho_\infty {Ca_{JSR}}^{h_{sr}}}{K^{h_{sr}} + {Ca_{JSR}}^{h_{sr}}} \tag{3.29}$$

3.5.3.3 Alternative RyR2 model

$$k_{12} = \frac{K_u {Ca_j}^2}{{K_{cp}}^2 + {Ca_j}^2} + w \tag{3.30}$$

$$k_{43} = \frac{K_b {Ca_j}^2}{{K_{cp}}^2 + {Ca_j}^2} + w \tag{3.31}$$

$$k_{21} = 0.5 \text{ ms}^{-1} \tag{3.32}$$

$$k_{34} = 3.3 \text{ ms}^{-1} \tag{3.33}$$

$$k_{14} = \frac{\hat{M} {\tau_b}^{-1} B_{max_{csqn}}}{B^0_{CSQN}} \tag{3.34}$$

$$k_{23} = \frac{\hat{M} {\tau_b}^{-1} B_{max_{csqn}}}{B^0_{CSQN}} \tag{3.35}$$

$$k_{41} = {\tau_u}^{-1} \tag{3.36}$$

$$k_{32} = \frac{k_{41}k_{12}k_{23}k_{34}}{k_{43}k_{14}k_{21}} \tag{3.37}$$

Equation 3.37 was modified from Ref. [55] to satisfy detailed balance.

Chapter 4

Calcium-driven alternans and arrhythmia vulnerability

4.1 Introduction

Decreased wavelength in the atria is a well-established mechanism of atrial fibrillation (AF) that supports conditions for reentry and thereby promotes AF initiation and maintenance [34]. Recently, efforts to understand the mechanisms of AF have focused increasingly on other aspects of AF remodeling, such as Ca^{2+} handling abnormalities [33] and alternans [17], the beat-to-beat alternation in cardiac electrical signals. Clinical evidence suggests that atrial alternans may play an important role in human AF [17]; however, it remains difficult to determine experimentally whether alternans as a secondary consequence of atrial remodeling in patients has a significant

effect on arrhythmogenesis. Understanding the role of atrial alternans in arrhythmogenesis will be critical for advancing our understanding of AF mechanisms and for developing new AF therapies in the future.

In Chapter 3, we demonstrated that Ca^{2+}-handling abnormalities occurring secondary to AF remodeling could underlie the action potential duration (APD) alternans observed during atrial pacing of AF-cardioverted patients. In this chapter, we present our investigation on the effects of Ca^{2+}-driven alternans (CDA) on arrhythmia initiation. For this study, we utilized a realistic 3D computer model of the human atria incorporating the cellular mechanisms identified in Chapter 3. We demonstrate that elevated CDA propensity leads to increased arrhythmia vulnerability due increased repolarization heterogeneity resulting from discordant alternans. Our findings suggest that CDA secondary to AF-induced electrical remodeling may play a significant role in the initiation of AF.

4.2 Methods

4.2.1 Human atria model

We used an anatomically realistic computer model of the human atria to investigate the effect of increased CDA propensity on arrhythmia initiation and maintenance in the atria. Model geometry was based on the Visible Human female dataset [92], which has been used previously to investigate mechanisms of arrhythmogenesis related

to AF [93]. To explore the effects of CDA secondary to AF-induced electrical remodeling on arrhythmogenesis, we tested two atria with chronic AF-induced structural and electrical remodeling. Structural changes were modeled by scaling anisotropic heterogeneous tissue conductivities to produce an average conduction velocity (CV) of 40 cm/s (Table 4.1), consistent with slowed conduction in chronic AF [94]. Electrical remodeling was based on a human atrial action potential (AP) model described by Grandi *et al.*, which produced APD shortening as observed in chronic AF [40]. These parameters led to alternans onset at fast pacing rates in the first atria model, ALT_{fast}. The second atria model,ALT_{slow}, incorporated an additional remodeling feature: reduction of ryanodine receptor (RyR2) inactivation rate by 50%, which we showed in Chapter 3 results in increased propensity to CDA, matching alternans onset at slower pacing rates observed clinically [18] (Fig. 4.1A, see Section 4.5.1). Regional AP heterogeneity between the left atrium (LA) (Fig. 4.1B) and the right atrium (RA) (Fig. 4.1C) were included in both ALT_{fast} and ALT_{slow} models (Fig. 4.1D), as described by Grandi *et al.* [40].

4.2.2 Numerical methods

A monodomain formulation was used to represent electrical propagation throughout the human atria model [23]. The monodomain and AP model equations were solved together by a finite element approach using the Cardiac Arrhythmia Research Package (CARP; Cardiosolv, LLC) [24, 48]. A time step of 20 μs was used for all

Figure 4.1: Human atria model

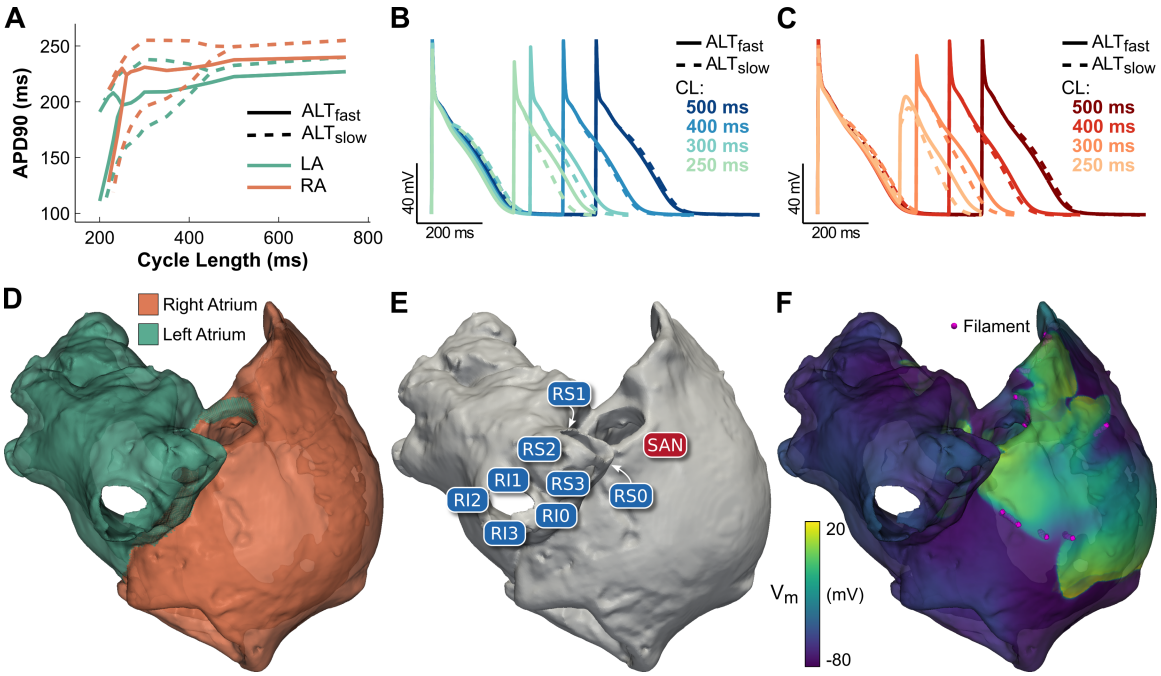

A. Single cell APD restitution for ALT_{fast} (solid line) and ALT_{slow} (dashed line) AP models, using LA (green) or RA (orange) parameter values for chronic AF (cAF) from Ref. [40]. **B.** LA cell APs for the ALT_{fast} and ALT_{slow} models at different pacing cycle lengths (CLs). **C.** RA cell APs for the ALT_{fast} and ALT_{slow} models at different pacing CLs. **D.** LA and RA regions in the human atria model. **E.** Stimulus locations. **F.** Detection of filaments during arrhythmia.

simulations. The mesh contained 2198425 nodes and 3005729 elements with a mean edge length of 330 μm.

4.2.3 Arrhythmia induction protocol

An S1–S2 pacing protocol was used to assess arrhythmia vulnerability due to an ectopic beat. Dynamic pacing was performed to reach the S1 pacing CL (300 ms). All nodes in the model were first initialized using steady-state values from a single cell paced at 750-ms CL. The atria were paced from the SAN region at 750-ms CL for 20 beats (Fig. 4.1E), and then for 32 beats at each subsequent pacing CL (500 ms to 300 ms in 50-ms decrements). After the 16^{th} even or odd beat at 300-ms CL pacing (S1), we ceased SAN pacing and applied an ectopic stimulus (S2) to one of eight locations in pulmonary veins at eleven different coupling intervals (CIs), ranging from 250 ms to 300 ms. Figure 4.1E shows location of the S2 stimuli, in the right superior pulmonary veins (RS0–3) or the right inferior pulmonary veins (RI0–3). Post-S2 activity was simulated for 2 s or until activity terminated, whichever came first.

4.2.4 Quantification of APD alternans

APD was calculated as the time from maximal upstroke velocity to 90% repolarization of transmembrane potential (V_m) from phase 2 amplitude. Alternans magnitude

was quantified as the mean change in APD from beat to beat over the last 10 pairs of beats (11 beats total) at a given pacing CL [18].

4.3 Results

4.3.1 Discordant alternans promotes reentry after an ectopic beat

We examined the effect of increased propensity to CDA on arrhythmia vulnerability in 3D models of the human atria incorporating both electrical (shortened AP) and structural (decreased conductivity) remodeling associated with AF. Two human atria models were compared: $\mathrm{ALT}_{\mathrm{fast}}$, with alternans only at fast pacing rates ($\mathrm{CL} \leq 270$ ms), and $\mathrm{ALT}_{\mathrm{slow}}$, with alternans at slower pacing rates ($\mathrm{CL} \leq 400$ ms) resulting from reduced RyR2 inactivation (see Section 4.2.1). An S1–S2 pacing protocol was performed in both models to induce arrhythmia. During S1 pacing at 300-ms CL, large-magnitude discordant APD alternans was evident in $\mathrm{ALT}_{\mathrm{slow}}$ but was absent in $\mathrm{ALT}_{\mathrm{fast}}$ (Fig. 4.2A). Accordingly, the distribution of repolarization times in the $\mathrm{ALT}_{\mathrm{fast}}$ model remained the same from beat to beat. In contrast, the distribution and spatial pattern of repolarization times in the $\mathrm{ALT}_{\mathrm{slow}}$ model changed noticeably between the even and odd beats (Fig. 4.2B). In particular, the even beat in the $\mathrm{ALT}_{\mathrm{slow}}$ model displayed the most heterogeneity, with areas of early (purple) and late (red)

Figure 4.2: Discordant APD alternans during S1 pacing

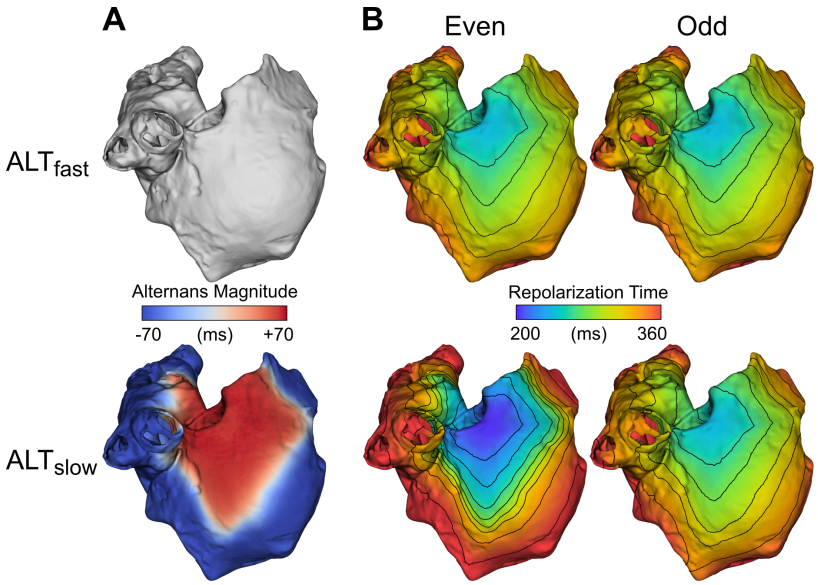

A. APD alternans magnitude. Regions of opposite phase are shown in different colors (red vs. blue). **B.** Time to 90% repolarization after even (left) and odd (right) paced beats. Top: ALT_{fast}. Bottom: ALT_{slow}.

repolarization separated by closely spaced isochrones.

When an S2 beat was delivered to the right superior pulmonary vein (RSPV) at a CI of 280 ms after the even beat, refractory tissue around the pulmonary vein blocked conduction towards the LA in both ALT_{fast} and ALT_{slow} models (Fig. 4.3). The wavefronts propagated first into the RA and eventually back around the RSPV into the LA (Fig. 4.3A). In ALT_{fast}, propagation around the RSPV was fast, resulting in the wavefront colliding with the refractory tail of the S2 wave and terminating the reentrant activity (Fig. 4.3B top). In ALT_{slow}, however, propagation towards the RA was fast while propagation around the RSPV was slow, due to the steep repolarization gradients from the previous S1 beat (Fig. 4.2B). This resulted in the

Figure 4.3: Induction of reentry by an S2 stimulus

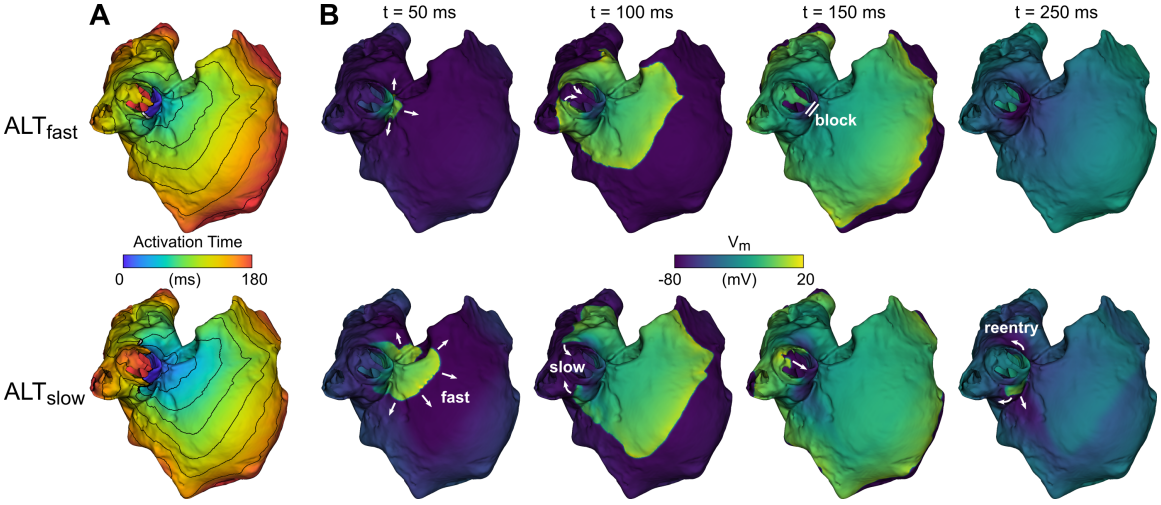

A. Activation time maps after an S2 stimulus was delivered at RS0 (see Fig. 4.1E), at a CI of 280 ms following an even S1 beat. **B.** V_m maps showing conduction block and reentry following S2 stimulus in panel A. Top: ALT_{fast}. Bottom: ALT_{slow}.

wavefront reaching the RSPV later than in ALT_{fast}, after refractory tissue from the S2 wave had already recovered, thus allowing reentry to continue around the RSPV for several cycles (Fig. 4.3B bottom).

4.3.2 CDA leads to increased arrhythmia vulnerability

The S1–S2 protocol was repeated for eight different stimuli locations in the right pulmonary veins, at 11 different CIs following an even or odd S1 beat, for both the ALT_{fast} and ALT_{slow} models (352 atrial simulations total, Fig. 4.4). As expected, outcomes for ALT_{fast} simulations were identical following even and odd beats, since

repolarization patterns did not change from beat to beat (Figs. 4.4A and 4.2A). Most ectopic beat locations and CIs did not produce reentrant activity in ALT_{fast}. Ectopic beats at three locations (RS0, RS1, and RS3) resulted in post-S2 reentry over a narrow range of CIs, which did not sustain for more than one reentrant cycle. In contrast, all eight ectopic beat locations produced post-S2 reentrant activity in ALT_{slow} (Fig. 4.4B). After the odd beat, any post-S2 activity in ALT_{slow} terminated after one reentrant beat, as in the ALT_{fast} simulations. After the even beat, however, more than one reentrant cycle was induced at two S2 stimulus locations in ALT_{slow} (RS0 and RS1). At RS0, three CIs resulted in reentry that broke up into multiple wavelets after about three cycles. In one simulation (RS0, CI = 270 ms), arrhythmia sustained >2 s after the S2 stimulus, during which the initial reentry around the RSPV eventually terminated and an unstable scroll wave later appeared and meandered in the RA. These results demonstrate that repolarization heterogeneity induced by CDA resulted in increased atrial vulnerability to arrhythmia induction by ectopic beats.

Figure 4.4: Vulnerability of atria to reentry

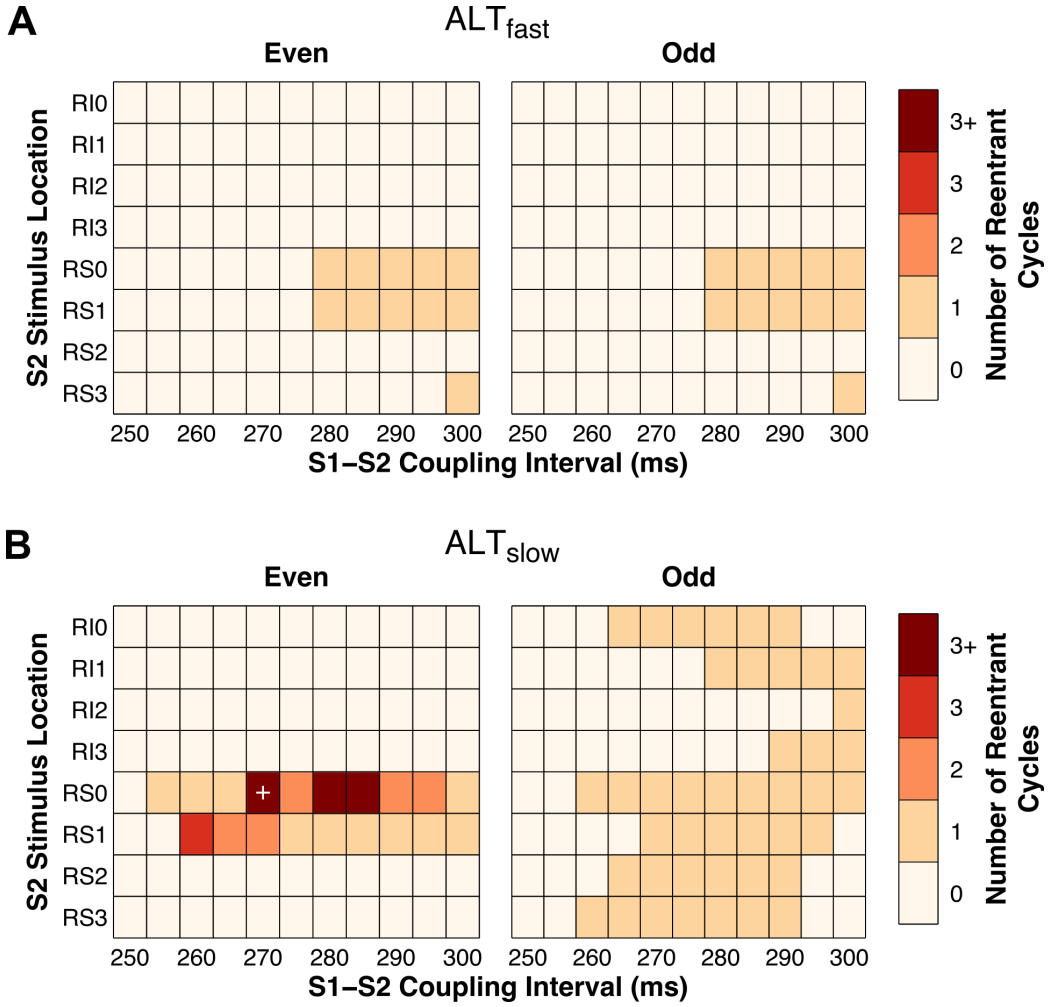

Summary of results for ALT_{fast} (**A**) and ALT_{slow} (**B**) simulations. When post-S2 reentrant activity lasted longer than three cycles, arrhythmia broke up into multiple wavelets (labeled "3+"). The simulation indicated by the white plus sign had arrhythmia lasting longer than 2 s.

4.4 Discussion

APD alternans has been observed at pacing rates as slow as 100–120 beats per minute in the atria of cardioverted AF patients undergoing electrophysiological study [17]. In Chapter 3, we examined the underlying cellular mechanisms driving APD alternans in remodeled atrial myocytes, showing that altered RyR2 kinetics and down regulation of L-type Ca^{2+} current induced by AF remodeling can lead to CDA at slower pacing rates. In this study, we addressed whether alternans occurring due to the Ca^{2+}-dependent mechanisms we identified previously can affect arrhythmia vulnerability in the atria.

Our results demonstrate that CDA occurring at slow pacing rates in remodeled atrial myocytes can increase the vulnerability of the atria to reentry. In a biophysically detailed, anatomically realistic model of the human atria, we found that shortened APD and reduced CV alone were not sufficient to render the atria vulnerable to reentry initiation by an ectopic beat from the pulmonary veins. In contrast, when CDA propensity was increased in the atria via reduction in RyR2 inactivation (see Section 3.3.4), reentry could be induced at two out of the eight right pulmonary vein locations tested. CDA created a vulnerable substrate defined by steep repolarization gradients, which allowed these ectopic beats to induce reentry. This mechanism might explain clinical observations of premature beats initiating AF in patients during slow pacing rates when APD alternans was present [18].

This study establishes a mechanistic link between Ca^{2+} handling instability, alter-

nans, and arrhythmia initiation in a model of the human atria. Previous investigations using computational modeling have addressed the role of alternans on arrhythmia initiation but in different contexts. Gong *et al.* tested the effect of electrically driven alternans on AF initiation in a computer model of paroxysmal AF, in which upregulation of L-type Ca^{2+} current (I_{CaL}) caused in APD prolongation and steepening of APD restitution slope [95]. However, APD and I_{CaL} are unchanged in paroxysmal AF [13] and are decreased in chronic AF [96], so the clinical relevance of their findings may be limited. The mechanisms explored in this study stem from a more current understanding of the role of Ca^{2+} handling abnormalities in human AF [25] and may thus provide better insight into the pathophysiological mechanisms underlying arrhythmogenesis in patients.

These findings demonstrate that CDA can help initiate arrhythmia in the atria. Identifying atrial alternans in patients may provide valuable insight into the arrhythmogenic substrate, but it remains to be determined whether CDA also plays a role in helping to maintain arrhythmia. This question has important implications for the understanding and treatment of AF and will be addressed in Chapter 5.

4.5 Appendix

4.5.1 Human atria model

Membrane kinetics in the human atria model was represented by the modified Grandi-Pandit-Voigt human atrial action potential model (see Section 3.5.1.1). Rule-based fiber orientation was included in the human atria model to produce realistic activation patterns [97]. Anisotropic conductivity ratios varied regionally as specified by Krueger *et al.* [97], with conductivities scaled uniformly to produce slow conduction consistent with measurements in AF patients [94] (Table 4.1).

Table 4.1: Human atria model regional conductivities

Region	Monodomain conductivity	Ref. [97] value (S/m)	Model value (S/m)	g_l / g_t	CV (m/s)
myocardium, appendages	g_t	0.075	0.04748	3.83	0.27
	g_l	0.28125	0.18188		0.66
valve rings	g_t	0.075	0.04748	3.71	0.27
	g_l	0.27225	0.17622		0.64
isthmus	g_t, g_l	0.075	0.04748	1	0.27
Bachmann's bundle	g_t	0.181	0.11489	3.97	0.50
	g_l	0.70228	0.45584		1.1
crista terminalis	g_t	0.075	0.04748	6.68	0.27
	g_l	0.492	0.31730		0.9
pectinate muscles	g_t	0.03	0.01905	23.77	0
	g_l	0.6975	0.45284		1.1
sinoatrial node	g_t, g_l	0.275	0.17796	1.00	0.65

Chapter 5

Calcium-driven alternans and arrhythmia maintenance

5.1 Introduction

Alternans, the beat-to-beat alternation in cardiac electrical signals, has been observed in the atria of cardioverted patients who experience atrial fibrillation (AF) [17], but its implications for arrhythmogenesis and AF treatment have not been fully explored. Alternans resulting from steep cardiac restitution properties can promote both initiation and termination of arrhythmias, by increasing the frequency of wave-break but at the same time destabilizing spiral waves [98]. Understanding the effects of atrial alternans on both the initiation and termination of arrhythmia is needed to enhance our understanding of AF mechanisms and aid in the development of new AF

treatments.

Our results in Chapter 4 demonstrate a plausible mechanistic link between atrial alternans and AF initiation, arising from the Ca^{2+} handling mechanisms explored in Chapter 3. In this chapter, we investigate the influence of Ca^{2+}-driven alternans (CDA) on arrhythmia complexity and persistence, utilizing the same computer model of the human atria described in Chapter 4. Results show that increased propensity to CDA leads to more frequent wavebreak and increased arrhythmia complexity. Furthermore, frequent wavebreak in CDA-prone atria also helps to sustain arrhythmia. Our findings suggest that CDA in the atria promotes arrhythmia maintenance by increasing arrhythmia disorganization and complexity and that atrial alternans may present a promising therapeutic target for AF.

5.2 Methods

5.2.1 Human atria model

The human atria model used in this study was identical to that used in Chapter 4 and described in detail in Sections 4.2.1 and 4.5.1. Briefly, two versions of the human atria model were compared to assess the effects of CDA. Both versions included AF-induced electrical and structural remodeling that resulted in action potential duration (APD) shortening and decreased conduction velocity (CV). In the first version (ALT_{fast}), CDA occurred only at fast pacing rates (cycle length (CL) ≤ 270 ms). In

the second version (ALT_{slow}), CDA began at slow pacing rates ($CL \leq 400$ ms) as a consequence of a 50% decrease in ryanodine receptor (RyR2) inactivation rate constant (ki_{Ca}), as detailed in Chapter 3.

5.2.2 Numerical methods

A monodomain formulation was used to represent electrical propagation throughout the human atria model [23]. The monodomain and action potential (AP) model equations were solved together by a finite element approach using the Cardiac Arrhythmia Research Package (CARP; Cardiosolv, LLC) [24, 48]. A time step of 20 μs was used for all simulations. The mesh contained 2198425 nodes and 3005729 elements with a mean edge length of 330 μm.

5.2.3 Arrhythmia induction protocol

To compare arrhythmia characteristics between ALT_{fast} and ALT_{slow} models, we induced arrhythmia using a dynamic pacing protocol similar to one used clinically [18]. All nodes in the model were initialized using steady-state values from a single cell paced at 750-ms CL. The atria were paced from the SAN region at 750-ms CL for 20 beats (Fig. 4.1E), and then for 32 beats at each subsequent pacing CL: from 500 ms to 300 ms in 50-ms decrements, then from 290 ms to 250 ms in 10-ms decrements.

5.2.4 Quantification of APD alternans

APD was calculated as the time from maximal upstroke velocity to 90% repolarization of transmembrane potential (V_m) from phase 2 amplitude. Alternans magnitude was quantified as the mean change in APD from beat to beat over the last 10 pairs of beats (11 beats total) at a given pacing CL [18].

5.2.5 Filament dynamics

Phase singularities (PSs) are points where the phase of the AP is undefined, occurring at locations of wavebreak or at the tip of a reentrant spiral wave. In 3D, PSs form the vortex filaments of reentrant scroll waves. To robustly detect filaments in our simulations despite variations in AP morphology [99], we developed a novel method for filament localization, which involves constructing phase maps from activation times (see Section 5.5.1). To gain insight into filament dynamics, we tracked at 1-kHz resolution each filament's birth, death, and interactions with other filaments, splitting (bifurcation) or merging (amalgamation) to form new filaments. A filament tree (FT) was defined as the set of filaments that interact with each other over time. Spurious filaments associated with brief wavebreak were not included in the dataset to allow interpretation of the temporal branching structure of filament interactions. An example snapshot of filament localization during arrhythmia is shown in Figure 4.1F. Details on filament detection can be found in Section 5.5.1.

5.2.6 Statistical analysis

Adjusted box-whisker plots were used to compare skewed distributions and detect outliers [100]. Chi-squared tests of independence without correction were used to assess differences in filament interaction [101]. The Mann-Whitney U statistic was used to test for differences in distribution location, with $p < 0.05$ considered significant. Pearson's correlation coefficient r was used to quantify the linear dependence between variables. Significance of Pearson correlations and their differences (Δr) was assessed using a percentile bootstrap method to estimate 95% confidence intervals (Wilcox-Muska confidence intervals) in the independent case, and using the HC4 method in the overlapping dependent case [102]. These methods have been shown to perform well under conditions of nonnormality and heteroscedasticity [103].

5.3 Results

5.3.1 CDA leads to increased arrhythmia complexity

We investigated the effect of CDA on arrhythmia complexity in the ALT_{fast} and ALT_{slow} atria models. Complexity was quantified by tracking filaments, which are the organizing centers of scroll waves where PSs occur (see Section 5.2.5). We paced the atria from the SAN region at progressively faster rates to induce arrhythmia.

Figure 5.1: Discordant APD alternans and filaments during fast pacing

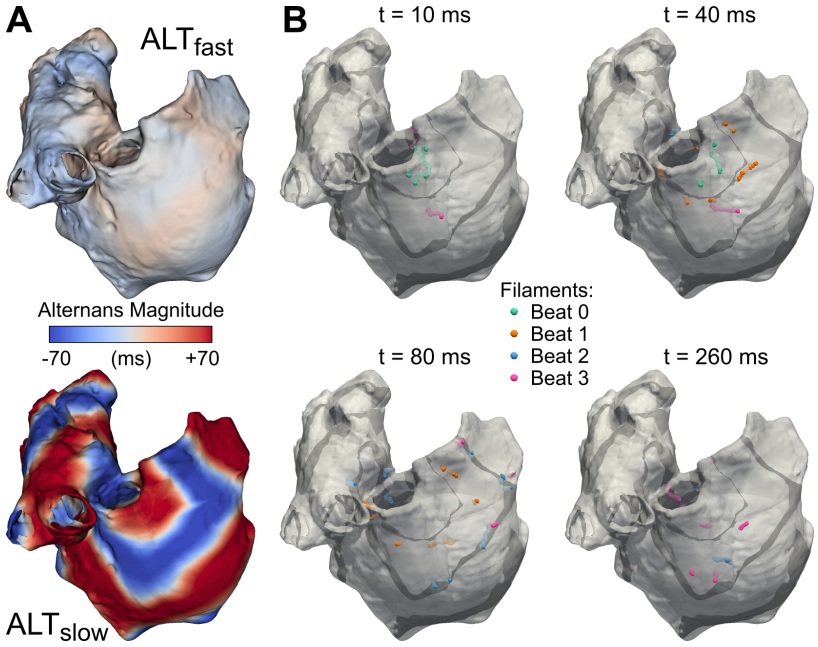

A. APD alternans magnitude in ALT_{fast} (top) and ALT_{slow} (bottom) during pacing at 270-ms CL. Regions of opposite phase are shown in different colors (red vs. blue). **B.** Nodal surfaces (black) and filaments (color) in ALT_{slow} during 260-ms CL pacing. Snapshots show filament locations at different times after a paced beat from sinoatrial node (SAN) region. Filaments from the first four beats are shown in different colors on the same snapshot for comparison.

Discordant APD alternans developed at 270- and 350-ms CL pacing in ALT_{fast} and ALT_{slow}, respectively. During 270-ms CL pacing, several discordant regions were present in both models, but APD alternans magnitude was noticeably larger in ALT_{slow} (red and blue regions, Fig. 5.1A). As pacing rate increased to 260-ms CL, this repolarization heterogeneity in ALT_{slow} led to wavebreak and filament formation near nodal lines, where regions with alternans of opposite polarity meet (Fig. 5.1B). Filaments appeared earlier (during 270-ms CL pacing) and were present longer in the ALT_{slow} model (Fig. 5.2A). During arrhythmia (i.e. at time points when filaments were present), ALT_{slow} tended to have significantly more filaments than ALT_{fast} (median was 2 and 6 filaments for ALT_{fast} and ALT_{slow}, respectively), indicating that CDA increased the complexity of arrhythmia (Fig. 5.2B and 5.1).

We investigated two possible contributors to the increased number of filaments in ALT_{slow}: additional new filament formation or increased filament duration. Figure 5.2C compares new filament formation during fast pacing (270-ms to 250-ms CL) in ALT_{fast} and ALT_{slow}. New filaments appeared steadily during 260-ms and 250-ms CL pacing in ALT_{slow} but slowed in ALT_{fast} after about 10 beats. Thus, to a large degree, new filament formation accounted for the increased number of filaments present in ALT_{slow}.

We also compared differences in individual filament persistence during fast pacing. The total number of filaments during this pacing period was 527 and 3197 for ALT_{fast} and ALT_{slow}, respectively. Short-lived filaments dominated both ALT_{fast} and ALT_{slow}

Figure 5.2: Filament dynamics during fast pacing

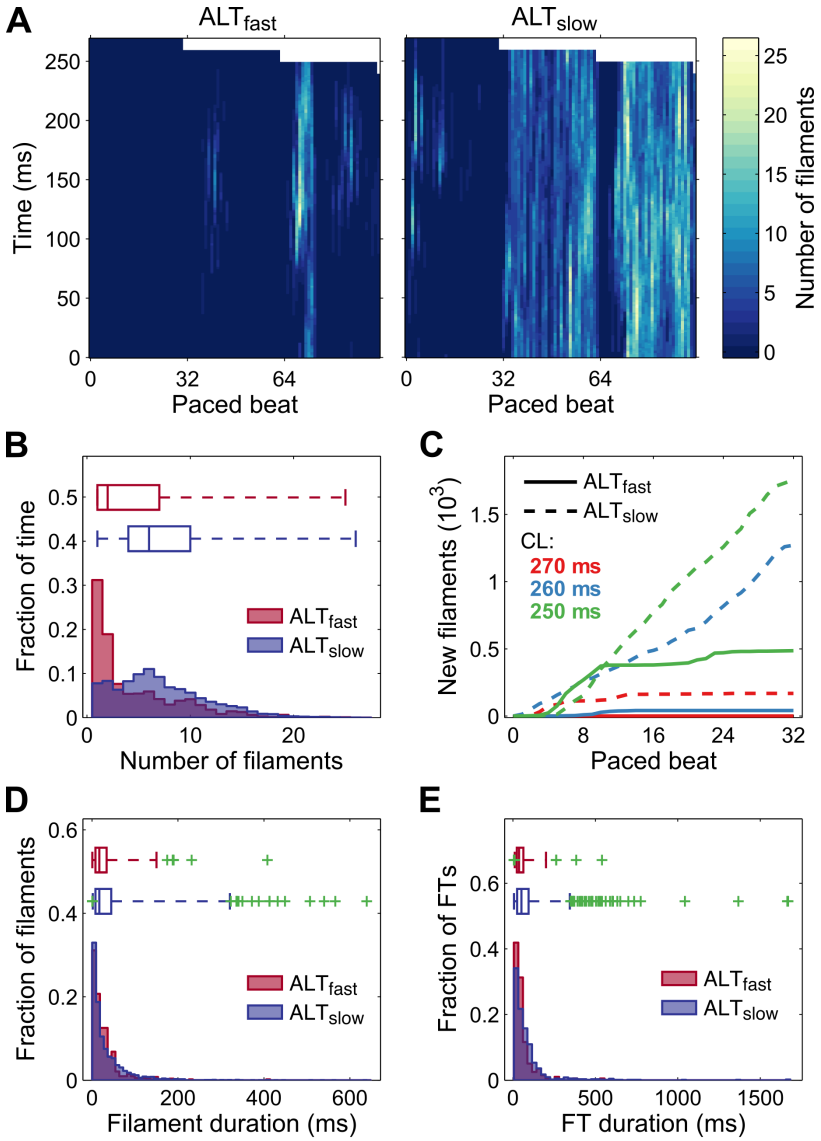

A. Heat maps of the number of distinct filaments present over time in ALT_{fast} (left) and ALT_{slow} (right). **B**, **D**, and **E**: Histograms and adjusted box-whisker plots for ALT_{fast} (red) and ALT_{slow} (blue). Green crosses indicate outliers. **B.** Number of filaments during arrhythmia (time points when filaments were present). **C.** Cumulative number of new filaments formed in ALT_{fast} (solid line) and ALT_{slow} (dotted line) at pacing CLs of 270 ms (red), 260 ms (blue), and 250 ms (green). **D.** Filament duration. **E.** FT duration.

Table 5.1: Filament and FT metrics during fast pacing

Mean values for the ALT_{fast} and ALT_{slow} simulations are reported for all metrics except for duration of arrhythmia, number of filaments, and number of FTs. Differences in distribution between the human atria model with alternans onset at fast rates (ALT_{fast}) and human atria model with alternans onset at slow rates (ALT_{slow}) simulations were assessed with the Mann-Whitney U statistic, with $p < 0.05$ considered significant.

	ALT_{fast}	ALT_{slow}	U	p
Duration of arrhythmia (ms)	3328	15894	-	-
Number of filaments during arrhythmia	4.50	7.07	16111484.5	$<10^{-6}$
Number of filaments	527	3197	-	-
Filament duration (ms)	28.4	35.2	808583	0.14
Number of FTs	198	976	-	-
FT duration (ms)	56.0	84.8	82880.5	0.002
FT composition metrics				
Mean filament duration (ms)	33.8	40.8	92282.5	0.32
Number of filaments	2.66	3.28	84377.5	<0.001
Max filament duration (ms)	47.8	63.3	84714	0.006
Sum of filament durations (ms)	75.6	115.3	82306.5	<0.001

Figure 5.3: Phase singularity density during fast pacing

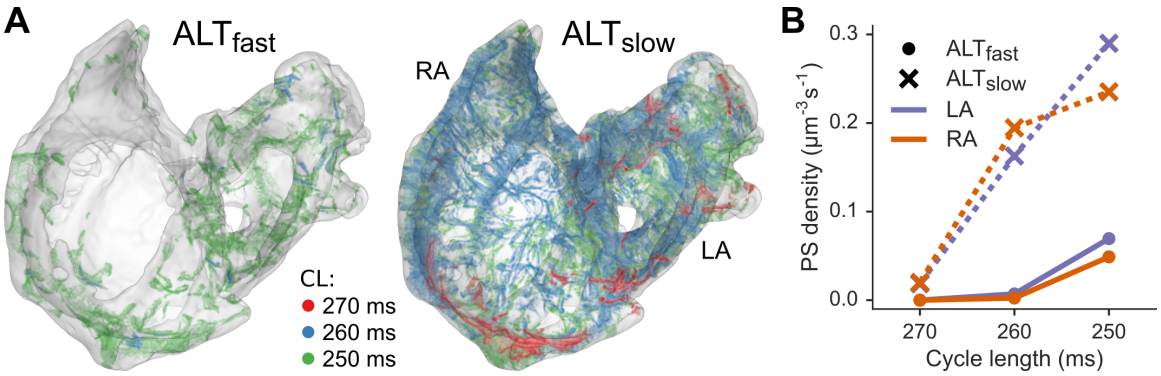

A. Locations of PS points in ALT_{fast} (left) and ALT_{slow} (right) during pacing at CLs of 270 ms (red), 260 ms (blue), and 250 ms (green). **B.** Mean density of points at which PSs occurred over time in the LA (purple) and RA (orange) for ALT_{fast} (circles) and ALT_{slow} (x's).

filament duration distributions (median duration was 17 ms for both simulations, Fig. 5.2D), and the difference in filament durations was not significant (5.1). However, the distribution of filament durations in ALT_{slow} was more right-skewed than in ALT_{fast} (Fig. 5.2D, top). Furthermore, nine of the fourteen long-lived filament outliers in the ALT_{slow} simulation persisted longer than 400 ms, whereas only one of the six long-lived outliers did so in the ALT_{fast} simulation. Thus, long lasting filaments occurred more frequently during fast pacing in atria with increased propensity to CDA.

Regional differences in the density of points at which PSs occurred over time were observed during fast pacing. In ALT_{fast}, there was higher PS density in the left atrium (LA) than in the right atrium (RA) (Fig. 5.3). In ALT_{slow}, PS density was higher in the RA than in the LA except during 250-ms CL pacing, when the reverse was true.

This was perhaps due to shorter APD in the LA (Fig. 4.1A), which allowed the LA to support more scroll waves.

5.3.2 CDA leads to increased arrhythmia persistence

New filaments can form when wavebreak creates new scroll waves, or when preexisting scroll waves interact or break up, resulting in the bifurcation and/or amalgamation of filaments. The proportion of filaments that formed from preexisting filaments during fast pacing (270-ms to 250-ms CL) was higher for ALT_{slow} (0.57 vs. 0.51, $\chi^2 = 6.02$, $p = 0.014$). Likewise, the proportion of filaments that were involved in forming new filaments was also higher for ALT_{slow} (0.55 vs. 0.50, $\chi^2 = 3.87$, $p = 0.049$). This suggested that increased filament interaction contributed to arrhythmia maintenance in ALT_{slow}.

To further characterize the dynamics of filament formation and persistence, we analyzed FTs, defined as the set of filaments that interact with each other spatiotemporally. During fast pacing, there were 198 and 976 total FTs in ALT_{fast} and ALT_{slow}, respectively. In both simulations, most FTs were short-lived (median duration was 37.5 ms and 52 ms for ALT_{fast} and ALT_{slow}, respectively) (Fig. 5.2E), but FT duration tended to be longer in ALT_{slow} (Table 5.1). The distribution of FT durations in ALT_{slow} was more right-skewed, with many more long-duration FT outliers (Fig. 5.2E,

Figure 5.4: Examples of FTs during fast pacing

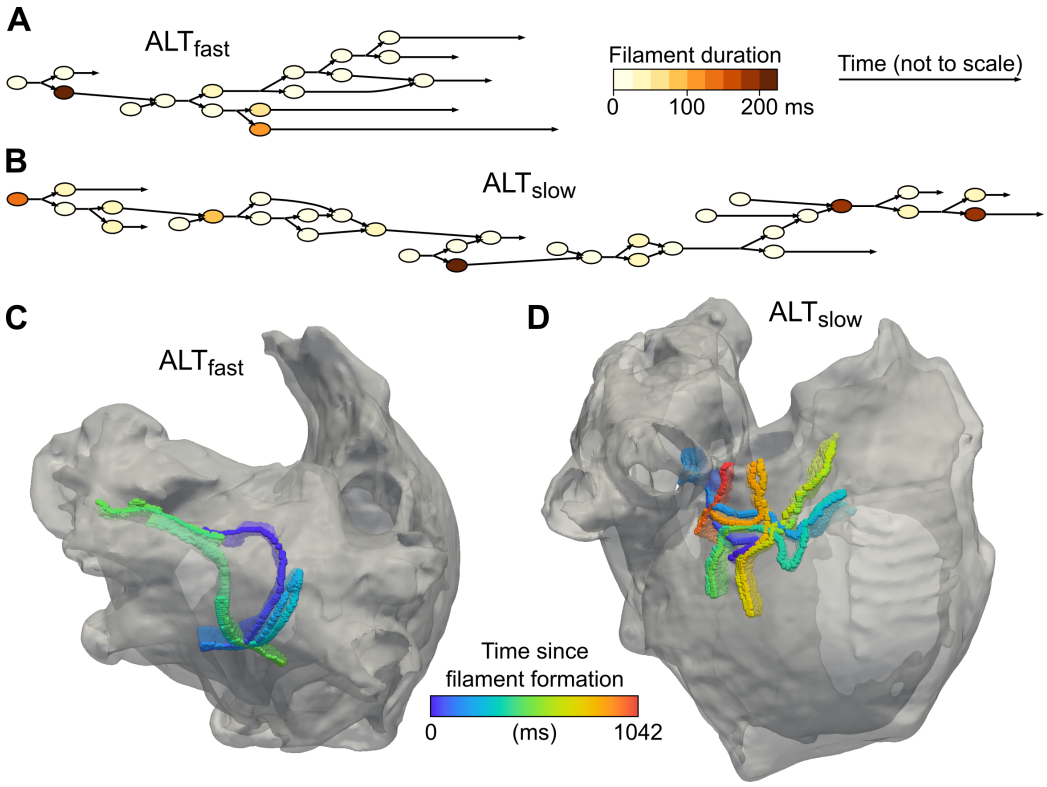

Graphs of FT branching structure from two example FTs in ALT_{fast} (**A**) and ALT_{slow} (**B**) simulations. Filament duration is indicated by node colors; time is not drawn to scale. Trajectories of FTs from panels A and B are shown in **C** and **D**, respectively.

top).

Two examples of long-lived FT outliers from ALT_{fast} and ALT_{slow} are presented in Figure 5.4. Although the branching patterns of FTs could be quite complex, several FTs displayed an overall linear structure (Fig. 5.4A–B), indicating that each FT was dominated by a single scroll wave. The lifetimes of these scroll waves were often punctuated by wavebreak, resulting in the branching of a single filament into several short-lived filaments (<25 ms). The ALT_{fast} scroll wave meandered around

Table 5.2: Pearson correlation analysis of FTs

Pearson correlations between FT duration and FT composition metrics for the ALT_{fast} and ALT_{slow} simulations and the difference in ALT_{fast} and ALT_{slow} correlations (Δr) were assessed during fast pacing (CLs of 270 ms to 250 ms). Confidence intervals at 95% are shown in brackets.

	ALT_{fast}	ALT_{slow}	Δr
Mean duration	0.37 [0.27 0.51]	0.34 [0.29 0.43]	0.03 [-0.11 0.18]
Number of filaments	0.61 [0.48 0.74]	0.70 [0.64 0.75]	-0.08 [-0.22 0.05]
Maximum duration	0.96 [0.92 0.98]	0.83 [0.80 0.89]	0.13 [0.06 0.17]
Sum of durations	0.92 [0.87 0.96]	0.95 [0.93 0.96]	-0.03 [-0.08 0.02]

the left atrial roof and lasted 540 ms (Fig. 5.4C). During its lifetime, one wavebreak occurred, separating the FT into two long-duration filaments (>100 ms, Fig. 5.4A). The ALT_{slow} scroll wave meandered in a limited region on the right atrial wall near the superior vena cava and lasted 1043 ms, substantially longer than the ALT_{fast} FT (Fig. 5.4D). Four wavebreak episodes occurred, separating the ALT_{slow} FT into five long-duration filaments (>75 ms, Fig. 5.4B). Thus, these patterns suggested that wavebreak contributed to increased persistence of scroll waves in ALT_{slow} as compared to ALT_{fast}.

In order to evaluate how representative these FTs were of general differences in FT composition between ALT_{fast} and ALT_{slow}, we assessed four different FT composition metrics: mean filament duration, number of filaments, maximum filament duration, and sum of filament durations. The averages of each of these metrics over all FTs

Table 5.3: Comparison of FT composition correlations

Pearson correlation between FT duration and mean filament duration was compared to the correlation between FT duration and other FT composition metrics for the ALT_{fast} and ALT_{slow} simulations during fast pacing (CLs of 270 ms to 250 ms). Confidence intervals at 95% are shown in brackets.

	ALT_{fast}	ALT_{slow}
Number of filaments	0.25 [-0.15 0.64]	0.36 [0.14 0.58]
Maximum duration	0.59 [0.44 0.74]	0.49 [0.37 0.62]
Sum of durations	0.55 [0.24 0.86]	0.61 [0.48 0.74]

within a simulation, and statistical tests of the differences between simulations, are reported in Table 5.1. For all FT composition metrics, ALT_{slow} tended to have larger values than ALT_{fast}, with statistical significance in all metrics except mean filament duration. Not surprisingly, these metrics were also positively correlated with longer FT duration (Table 5.2).

Figure 5.5 illustrates the relationship between FT duration and FT composition metrics. Although a modest linear trend was present in the relationship between FT duration and mean filament length, FTs with the longest duration deviated significantly from this trend, having very short mean filament duration (Fig. 5.5, column 1). FT duration was more strongly correlated with the total number of filaments per FT (column 2), with the maximum filament duration within each FT (column 3), and with the sum of filament durations within each FT (column 4) (Table 5.3).

These statistical trends were consistent with observations in the two example

Figure 5.5: FT composition during fast pacing

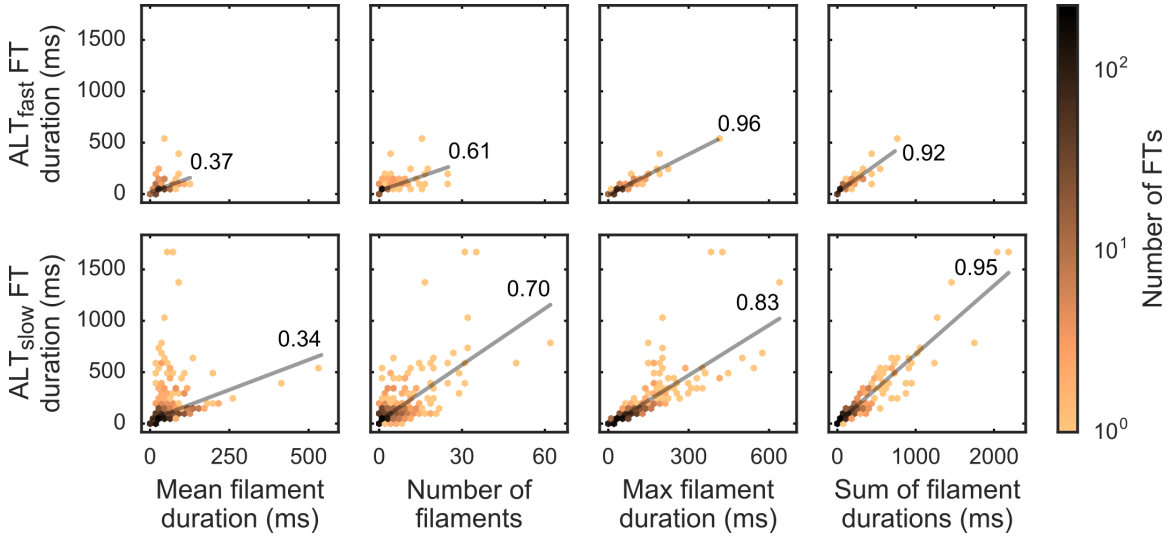

Top: ALT_{fast}. Bottom: ALT_{slow}. Left to right: mean filament duration, number of filaments, maximum filament duration, and sum of filament durations. Linear best fit lines and Pearson correlation coefficients are shown in each plot.

FTs from Figure 5.4. In general, the longest-lived FTs were composed of a few long-duration filaments (>75 ms) preceded and/or followed by the numerous short-duration filaments (<25 ms) that formed during wavebreak. Therefore, mean filament duration was weakly correlated with FT duration, but the number of filaments and the sum of filament durations were strongly correlated with FT duration (Table 5.2 and Fig. 5.5). Additionally, maximum filament duration was more strongly correlated with FT duration in ALT_{fast} than in ALT_{slow} ($r = 0.13$ [0.06, 0.17], Table 5.2). This was because long-lived FTs in ALT_{fast} tended to be composed of only one or two long-duration filaments, while long-lived FTs in ALT_{slow} tended to be composed of many long-duration filaments, due to the occurrence of several wavebreak episodes

in each FT's lifetime. Thus, the above results demonstrate that increased wavebreak resulting from increased propensity to CDA in ALT_{slow} helped to sustain arrhythmia in the remodeled atria during fast pacing.

5.4 Discussion

Many remodeling changes secondary to AF are profibrillatory, leading to a cycle of worsening AF susceptibility over time (the idea that "AF begets AF"). In particular, shortened APD and decreased CV promote reentry and can thus stabilize scroll waves to help maintain AF [104]. Since alternans promotes breakup and destabilizes scroll waves, the initiation and persistence of the arrhythmia in the presence of alternans depends critically on restitution properties [98]. In Chapter 3, we showed that APD alternans likely arises from Ca^{2+} handling instabilities caused by altered RyR2 kinetics in atrial myocytes. In Chapter 4, we showed that CDA can increase the vulnerability of the atria to reentry. In this chapter, we addressed the profibrillatory nature of CDA, investigating whether elevated CDA propensity ultimately promotes or prevents the maintenance of arrhythmia in the atria.

Our results show that CDA-prone atria display more frequent wavebreak at fast pacing rates, resulting in more complex arrhythmia. Frequent wavebreak at fast pacing rates was also associated with longer-duration scroll waves, suggesting that increased wavebreak due to Ca^{2+} handling instability ultimately led to increased

arrhythmia persistence, by producing more scroll waves that helped maintain the arrhythmia. Thus, preventing alternans by targeting the Ca^{2+} handling mechanisms underlying it may have significant antiarrhythmic benefit.

Three-dimensional computer models of atrial anatomy and electrophysiology provide a powerful tool for dissecting the mechanisms involved in AF arrhythmogenesis [19, 105]. Previous computational studies have examined the arrhythmogenic role of decreased wavelength due to AF remodeling, namely shortened APD and/or decreased CV [82, 93, 106]. The mechanisms explored in this work stem from a more current understanding of the role of Ca^{2+} handling abnormalities in human AF [25] and may thus provide better insight into the pathophysiological mechanisms underlying arrhythmogenesis in patients.

Increased propensity to CDA at slower pacing rates increased the complexity and persistence of arrhythmias occurring during fast pacing. Arrhythmias were characterized by unstable scroll waves which meandered over large areas and frequently broke up, similar to those observed clinically with electrocardiogram imaging [16]. Frequent wavebreak due to underlying Ca^{2+} instability helped perpetuate arrhythmia in the remodeled atria, supporting the view that abnormal Ca^{2+} handling may play a significant role in the AF substrate of patients with elevated alternans propensity.

The main mechanisms in AF are much debated, with one of the central controversies being whether AF occurs primarily due to organized reentrant drivers or multiple wavelets [107]. Although several lines of evidence suggest that organized reentrant

drivers underlie arrhythmias in many AF patients and may be targeted to effectively terminate arrhythmia [108], patients with longer-duration continuous AF usually do not respond to ablation therapy [16]. Although exploring AF termination was beyond the scope of this study, we speculate that the disorganized, multiple-wavelet arrhythmia occurring due to increased CDA propensity in our model would be more difficult to terminate. Thus, CDA may reflect some of the progressive changes that occur in the underlying substrate during long-standing AF which make standard therapies ineffective. However, in the present study, we modeled fibrotic changes due to AF as a global decrease in tissue conductivity, without taking into account specific patterns of structural heterogeneity that can influence arrhythmia organization [109–111]. Further work is needed to determine how interaction of structural and functional mechanisms affect arrhythmia organization in AF [112–114], particularly in patients that do not respond to ablation therapy.

Recent efforts to identify mechanisms and potential pharmacological targets in AF have shown that suppressing CDA may have significant antiarrhythmic benefits. Ca^{2+} transient alternans and abnormal Ca^{2+} release events have been observed in mouse [62] and canine [115] models of AF. Treatment with S107 in mouse [62] and dantrolene in canine hearts [116] appeared to stabilize RyR2 and effectively reverse abnormal changes in Ca^{2+} handling to prevent arrhythmia. Our results suggest that similar mechanisms may be at play in human AF as well, since increased propensity to CDA driven by RyR2 dysfunction led to increased arrhythmia vulnerability, complex-

ity, and persistence in our model. Recent evidence for this comes from experiments in human atrial myocytes of control and AF patients, which identified a link between adenosine signaling, alternans, and Ca^{2+} handling instability, potentially mediated by protein kinase A regulation of RyR2 [117]. However, the main mechanisms of RyR2 regulation are extremely complex [118] and controversial [69]. Further work needs to be done to clarify the mechanisms of RyR2 regulation and to explore the antiarrhythmic benefits of RyR2-targeting therapies that address the dual role of Ca^{2+} as both an initiating trigger and vulnerable substrate in AF [33].

Although the present study focused on the role of alternans in chronic AF, elevated propensity to APD alternans has been observed in paroxysmal AF patients as well [18, 30, 32]. However, the mechanisms underlying alternans may differ, since Ca^{2+} handling is altered between paroxysmal and chronic AF [13]. In paroxysmal AF, evidence suggests that SK channels [119], acetylcholine-activated K^+ current [120], and late Na^+ current [121] may play a more prominent role in alternans propensity and arrhythmogenesis. Given the arrhythmogenic implications of APD alternans presented in this and other studies, these differences in the fundamental mechanisms underlying APD alternans in paroxysmal versus chronic AF underscore the need for further research on the diversity of AF mechanisms [11], in order to develop better targeted, patient-specific therapies.

In conclusion, alternans driven by Ca^{2+} handling abnormalities secondary to AF-induced remodeling appears to play a significant role in arrhythmia maintenance.

We found that increased repolarization heterogeneity due to discordant CDA led to increased arrhythmia complexity and persistence in a computer model of the human atria. The mechanisms explored in this study may be particularly relevant to long-standing or permanent AF cases that are unresponsive to standard therapies. Consideration of these mechanisms will be important for the development of new approaches to AF treatment in the future.

5.5 Appendix

5.5.1 Filament calculations and filtering

We developed an algorithm to find filaments using activation time data. When V_m of a particular node, n_i, crossed above the activation threshold (-40 mV), an activation time value (ATV) of 1 was assigned to n_i for that time point. Any activations occurring within 50 ms of a previous activation at the same node were discarded. To generate smooth activation wavefronts, if any adjacent node (sharing the same element) activated within the 20 ms after the activation of n_i, then n_i was assigned an ATV of 1 from the time of its own activation up to and including the time of the last activation of an adjacent node. For the subsequent 20 ms, the ATV at n_i was decremented by 0.05/ms. n_i was assigned an ATV of 0 at all other times. Phase singularities were located as described by Iyer and Gray [122]. The phase of n_i (θ_{n_i})

at each time point (t) was computed by the following function:

$$\theta_{n_i}(t) = \text{arctan2}\left(\text{ATV}_{n_i}(t+\tau) - \text{ATV}^*, \text{ATV}_{n_i}(t) - \text{ATV}^*\right) \tag{5.1}$$

where $\tau = 1$ ms and $\text{ATV}^* = 0.5$. The choice of these parameters followed naturally from the prescribed time course of the ATV variable after activation. PSs were identified by calculating the line integral of the phase around every face in the model [123]. All nodes of any face containing a PS (line integral $= \pm 2\pi$) were assigned as being associated with a PS. A filament was identified as the set of adjacent nodes associated with PSs.

Filaments were tracked spatiotemporally at a resolution of 1 kHz, as described by Clayton and Holden [124]. If only one filament from the current time step shared nodes with or was adjacent to exactly one filament from the previous time step, it was considered the same filament. However, when a filament shared nodes with or was adjacent to more than one filament from the previous time step, the filament in the current time step was considered a new filament generated from the merging of the filaments of the previous time step. Conversely, when multiple filaments shared nodes with or were adjacent to a filament from the previous time step, the filaments in the current time step were considered new filaments generated from the splitting of the filament in the previous time step. A FT was defined as the set of filaments that interacted over time.

To simplify analysis of filament populations, we removed spurious filaments, defined as any filament lasting <6 ms which did not arise from previous filaments and did not generate new filaments. At the beginning or end of a FT, these were associated with complex conduction block patterns that were not of interest in this study. In the middle of a FT, these were often associated with minute wavebreaks. When multiple filaments merged into one, or one filament split into multiple, spurious filaments were removed from the set of multiple filaments such that the longest-lived filament (whether spurious or not) always remained. In the event that at this branching point, all but one filament was removed, the filament before and after this point would be considered the same filament (i.e. the branching point disappeared).

Chapter 6

Conclusion

In this thesis work, we investigated both the mechanistic underpinnings and the arrhythmogenic consequences of atrial alternans related to atrial fibrillation (AF). Using biophysically detailed computer models of the human atria, we have shown that altered Ca^{2+} release is mechanistically linked to increased arrhythmia risk via alternans. In Chapter 3, we presented a detailed investigation into the AF-related cellular mechanisms underlying action potential duration (APD) alternans occurring at clinically observed pacing rates. We showed that decreased ryanodine receptor (RyR2) inactivation leads to Ca^{2+} cycling instabilities that result in Ca^{2+}-driven alternans (CDA). In Chapter 4, we evaluated the effects of these mechanisms on arrhythmia vulnerability in a realistic human atria model. Simulations demonstrated that repolarization heterogeneity resulting from discordant CDA renders the atria inducible to sustained reentry from a properly timed and located ectopic beat. Lastly, in Chap-

ter 5, we assessed the influence of CDA on arrhythmia complexity and persistence in the human atria model. We found that CDA led to more frequent wavebreak, which resulted in more complex and longer-lasting arrhythmia. Thus, alternans appears to have a significant impact on the AF substrate, influencing both the initiation and maintenance of reentrant arrhythmia in the atria.

These findings have several important implications. First, these simulations predict that stabilizing the RyR2 through drug targeting should provide significant antiarrhythmic benefit in human, as has been previously shown in animal models. Experiments to characterize the effects of RyR2-targeting drugs in human atrial myocytes will be needed to help validate modeling predictions and strengthen the argument for developing these drugs to treat AF. Second, our findings suggest that CDA can lead to changes in arrhythmia organization in the atria and may thus impact the efficacy of currently available AF treatments. Improving methods to detect and characterize atrial alternans in patients may aid in the development of personalized, mechanism-based therapies. Lastly, we have demonstrated the utility of biophysically detailed computer models for providing valuable insights into clinically relevant mechanisms of arrhythmogensis. This type of analysis, spanning the cellular to organ scale, would be extremely difficult to achieve in experimental settings and is at present only possible using a computational approach. As experiments uncover new insights into the complex regulation of RyR2 in the atria, incorporation of such findings into computer models will advance the understanding and treatment of AF in the future.

Appendix A

Conduction block and defibrillation with high-frequency electric fields

This section presents additional work that was completed during the Ph.D. It has been published in *Science Translational Medicine* [125] and *Heart Rhythm* [126].

A.1 Introduction

Ventricular fibrillation (VF) is a lethal arrhythmia which currently can only be treated by brief, high-voltage direct current (DC) or biphasic shocks. Though effective, these strong electric shocks damage the myocardium and cause pain. Alternative methods of defibrillation are needed.

The goal of this study was to explore the use of high-frequency alternating current

(HFAC) electric fields to block conduction and thereby terminate arrhythmia in the ventricles.

A.2 Methods

A.2.1 Rabbit ventricular model

Simulations were performed using a previously validated anatomical model of rabbit ventricles incorporating realistic geometry and fiber orientation [127–129]. A bidomain representation was used to model the electrical behavior of the tissue, including its response to external field stimulation [130]. Membrane kinetics were represented by the Luo-Rudy ionic model [131], which was modified for modeling responses to external electric field stimulation, and to promote wavebreak and fibrillation, as previously described [132–135]. Bidomain conductivities and Luo-Rudy model modifications are given in Table A.1.

A.2.2 Numerical methods

Solutions to the bidomain and membrane equations were computed numerically using the Cardiac Arrhythmia Research Package (CARP) [23]. To reduce the extensive computation time required for these simulations, the CARP software was run in parallel mode [23] on the IBM iDataPlex cluster at the Institute for Computational

Table A.1: Computational model parameters used in rabbit heart simulations.[1]

Description	Parameter	Value	Units
Bidomain conductivities			
Intracellular, longitudinal to fiber direction	g_{il}	1.74	mS/cm
Intracellular, transverse to fiber direction	g_{it}	0.19	mS/cm
Extracellular, longitudinal to fiber direction	g_{el}	6.25	mS/cm
Extracellular, transverse to fiber direction	g_{et}	2.38	mS/cm
Perfusing bath	G_0	0.80	mS/cm
Modified Luo-Rudy model parameters			
Maximum fast Na^+ current conductance	$\bar{g}_{Na}$	16	mS/cm^2
Maximum delayed rectifier K^+ current conductance	$\bar{g}_{Kr}$	0.426	mS/cm^2
Maximum slow inward (Ca^{2+}) current (I_{Ca}) conductance	g_{Ca}	0.062	mS/cm^2
I_{Ca} activation-gate (d) time constant speed-up factor		1.5	-
I_{Ca} inactivation-gate (f) time constant speed-up factor		1.5	-

[1] From H. Tandri, S. H. Weinberg, K. C. Chang, R. Zhu, N. A. Trayanova, L. Tung, and R. D. Berger, "Reversible cardiac conduction block and defibrillation with high-frequency electric field." *Science translational medicine*, vol. 3, no. 102, p. 102ra96, sep 2011. Reprinted with permission from AAAS.

Medicine at Johns Hopkins University. Details on the numerical techniques used by CARP can be found elsewhere [24, 48, 136, 137]. A time step of 20 μs was used.

A.2.3 Protocol for testing high-frequency defibrillation

VF was induced using an S1-S2 protocol described previously [128]. Briefly, the ventricles were paced from the apex to steady state at a cycle length (CL) of 300 ms, and a 10-ms monophasic shock (9.3 V/cm, tilt = 62%) was delivered 200 ms after the last paced beat across left and right plate electrodes. HFAC field pulses of varying field strength were then delivered across the same plate electrodes at nine different coupling intervals (CIs) after the S2 shock (500, 600, 750, 900, 1000, 1100, 1250, 1400, and 1500 ms). Simulations were run for 500 ms after the end of the HFAC pulse.

A.2.4 Protocol for quantification of conduction block

VF was induced with a cross-stimulation protocol. The ventricles were paced from the apex at basic CL of 300 ms, and then a 10-ms, 6-V/cm monophasic shock (62% tilt) was applied 190 ms after the last paced beat, via parallel plate electrodes located in the surrounding bath. Sinusoidal HFAC field pulses (50–500 Hz, 5–25 V/cm, 1 s) were then delivered from plate electrodes at 11 different CIs following VF initiation (500–1500 ms, in 100-ms intervals). After HFAC field pulse end, simulations were run

for an additional 500 ms to assess defibrillation outcome. The VF termination rate over all CIs was determined for each field strength and frequency combination.

A.2.5 Data analysis

We defined a conduction block metric as follows: transmembrane potential (V_m) power spectrum at each node was calculated before and during the HFAC field by Fast Fourier Transform. V_m power spectra before and during the field were computed over 500-ms time windows ending at the time of field onset and offset, respectively. V_m traces from the windows before and during the field are shown in red and blue, respectively, in Figure A.2. Electrical conduction during both sinus rhythm and fibrillation is typically in the range of 1–30 Hz. Therefore, the areas under the power spectrum curve in the "conduction" frequency range of 1–30 Hz were computed for time windows before and during the HFAC field. The loss of conduction power (LCP) at each pixel was calculated as the percentage decrease in the conduction power during field application, compared with that before application, such that:

$$\text{LCP} = \frac{Area_{Before} - Area_{During}}{Area_{Before}} \tag{A.1}$$

For a given field strength and frequency, we defined two global values: 1) the average LCP and 2) the conduction block (CB) size. 1) LCP values were calculated at each node as described above, and an average LCP value was computed for a given

field strength and frequency by obtaining a weighted average over relevant nodes for each CI (weighting each nodal value by the volumes of attached elements, see Section A.2.6), and then averaging over all CIs. 2) CB was identified as occurring at site where LCP was >90%. The size of CB regions was expressed as a percentage of the total ventricular volume with LCP >90% (see Section A.2.6).

To investigate the effect of HFAC fields on CB location and LCP distribution, we considered the fact that the majority of the V_m change induced by an external field resulting from current entering the tissue is contained within one space constant [138]. Since the space constant in the direction transverse to cardiac fibers is approximately 300 μm [139], most of the field-induced surface polarization is contained within the surface layer of elements in the model (average internodal distance of 507 μm). Thus, we considered surface nodes, defined as nodes exposed to the external bath (consisting of 24% of all nodes), separately from sub-surface (interior) nodes, defined as nodes only connected to other tissue nodes (76%). Additionally, we analyzed the epicardial and endocardial surface nodes separately.

A.2.6 Computing weighted averages

Since the computational mesh is composed of linear tetrahedral elements, average V_m over a given volume may be computed by weighting the volume of each element contained within the total volume by the average V_m of attached nodes, summing the weighted volumes, and normalizing by the total volume. However, interpolation

and integration of LCP over element volumes is not as straightforward, since LCP is a nonlinear function of V_m. Therefore, in lieu of a true volume average, and since segmentation of the mesh into surface and sub-surface regions was done by nodes rather than by elements, we used a weighted average of nodal LCP values (weighted by the volumes of attached elements and normalized by total counted volume) to assess average LCP throughout the surface and sub-surface regions:

$$\overline{\mathrm{LCP}}_S = \frac{\sum_{n\in S}\sum_{e\in E_n} \mathrm{LCP}_n V_e}{\sum_{n\in S}\sum_{e\in E_n} V_e} \tag{A.2}$$

where S is the subset of nodes on either the surface or sub-surface, E_n is the subset of elements connected to node n, LCP_n is the LCP value at node n, and V_e is the volume of element e. A global LCP value for each field strength and frequency combination was then obtained by averaging over all CIs. CB size was calculated in the same manner, except with nodal LCP values replaced by 1 or 0 for $\mathrm{LCP} > 90\%$ or $\leq 90\%$, respectively, and normalized as a percentage of the total number of nodes. CB size is therefore a proxy measure for CB volume, as determination of the actual volume would have required continuous interpolation and integration of LCP over the each element. Nonetheless, our metric is an estimate that provides a basis for future prediction and comparison.

The number of regions without conduction block was determined by separating all nodes with $\mathrm{LCP} \leq 90\%$ into groups of continuous nodes (see Fig. A.5). Each group

was considered one region. The size of each region was determined using the same weighted average formula as above, except with the nodal values replaced by 1 if a node fell within the region and 0 otherwise, and this was summed over all nodes in the mesh and normalized as a percentage of the total number of nodes.

A.2.7 Statistical methods

All summary values are expressed as mean ± standard error and compared using the Student's t test. Pearson's correlation coefficient r was computed to assess linear correlation. William's formula was used to test for statistically significant differences between dependent correlations [140]. For all tests, $p < 0.05$ was considered to be significant.

A.3 Results

A.3.1 Conduction block and defibrillation by HFAC

We examined the effect of HFAC fields in the rabbit ventricular model (Fig. A.1A, Section A.2.1), using the protocol described in Section A.2.3. Consistent with experimental results [125], the model demonstrated that HFAC fields (25 V/cm) elevated V_m (Fig. A.1B) and induced oscillations in V_m of opposite polarity at closely spaced sites on the epicardial surface at the HFAC field frequency of 200 Hz (Fig. A.1C). This

extinguished all pre-existing fibrillatory wavefronts, completely blocking propagation in some tissue regions and evoking slow activity in other regions, perhaps because of variable blockade of Na^+ channels (Fig. A.1A). At the cellular level, in regions of conduction block, V_m, Ca^{2+} current (I_{Ca}), K^+ current (I_K), and intracellular Ca^{2+} (Ca_i) approached persistently elevated oscillating levels; whereas the Na^+ current (I_{Na}) was completely absent, coincident with the onset of the HFAC field at time 0 (Fig. A.1D).

Excitability is a post-shock property that depends on the amount of available tissue with V_m below the Na^+ channel activation threshold. It affects the success of a defibrillation shock [129, 141] and varies greatly during VF. During HFAC field application, the amount of inexcitable tissue (tissue with V_m elevated above the Na^+ channel activation threshold) was maintained at an oscillating, elevated steady state (Fig.A.1E), thereby reducing the likelihood of reinitiation of fibrillation after field offset. Application of sufficiently strong HFAC fields successfully terminated VF 100% of the time (9/9 different timings for HFAC field application) (Fig.A.1F). Although the phase of application of HFAC was variable, termination was achieved in all the trials using sufficient HFAC field, demonstrating that defibrillation success depends on the state of the heart at field offset, regardless of the initial conditions at field onset.

APPENDIX A.

Figure A.1: Computer simulation of HFAC field application in a bidomain model of a rabbit heart[2]

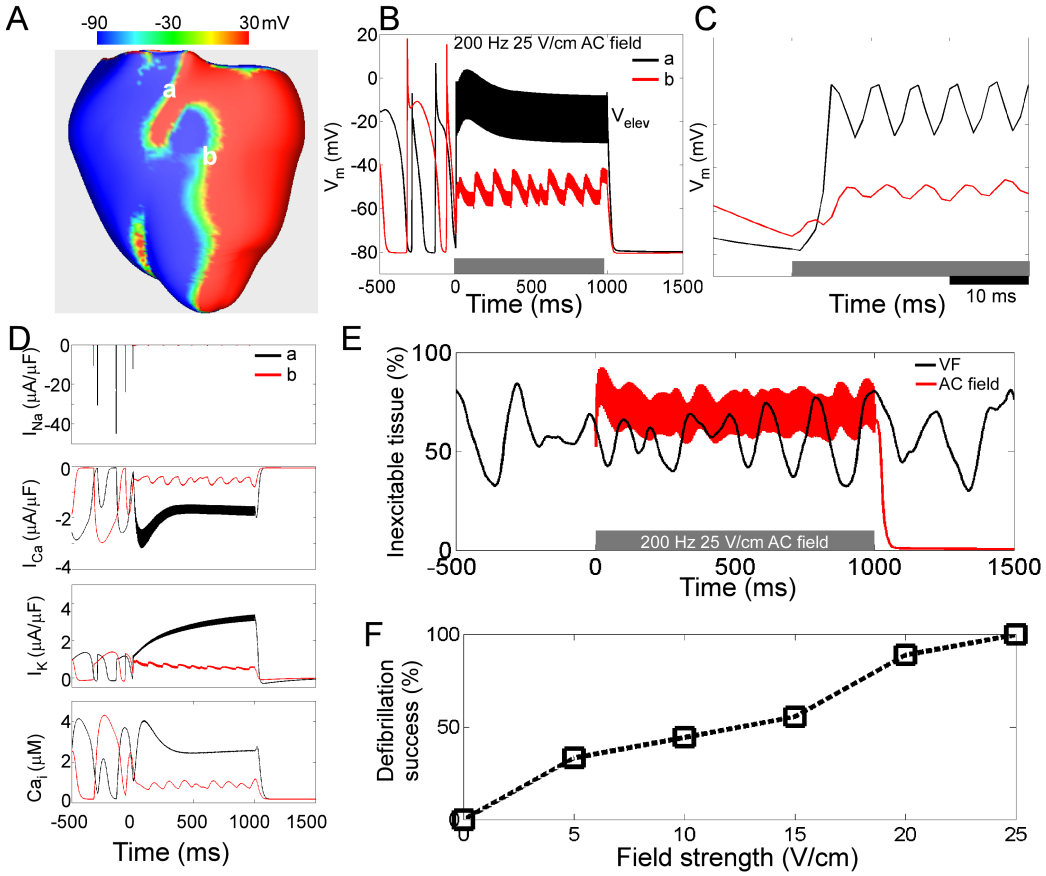

A. Simulated transmembrane potential (V_m) map during a 200-Hz HFAC field application at field offset (t = 1000 ms). **B.** V_m traces before, during (gray area), and after HFAC field (25 V/cm). **C.** V_m traces from panel B at expanded time scale to show oscillations at 200 Hz, with regions of opposite polarization. **D.** Na^+ (I_{Na}), Ca^{2+} (I_{Ca}), and delayed rectifier K^+ (I_K) currents and intracellular Ca^{2+} concentration (Ca_i) during HFAC field application. **E.** Percentage of inexcitable tissue before, during (gray area), and after HFAC field (red trace). Trace for a VF episode without HFAC field application (black) is also shown. Black and red traces overlap before HFAC field. **F.** Defibrillation success rate, plotted as a function of field strength for 200-Hz HFAC fields lasting 1 s.

[2]From H. Tandri, S. H. Weinberg, K. C. Chang, R. Zhu, N. A. Trayanova, L. Tung, and R. D. Berger, "Reversible cardiac conduction block and defibrillation with high-frequency electric field." *Science translational medicine*, vol. 3, no. 102, p. 102ra96, sep 2011. Reprinted with permission from AAAS.

A.3.2 Degree and location of conduction block in 3D ventricles

We utilized simulations with an anatomically accurate model to assess CB in the 3D rabbit ventricles, both on the epicardial and endocardial surface, and in the interior sub-surface regions. Protocols are described in Section A.2.4. In a simulation of VF with an applied 200-Hz, 15-V/cm field (Fig. A.2), we observed that the HFAC field only blocked conduction in some regions, i.e. incomplete CB. Consistent with experiments, V_m traces in regions of CB (sites a and d) were elevated and oscillating during HFAC with either no or small-amplitude activations, while areas of impeded propagation (sites b, c, and e) had smaller V_m elevation and larger-amplitude activations (Fig. A.2A).

Spatial maps of LCP on the epicardial surface (Fig. A.2A, sites a and b) were consistent with experiments [126], showing areas of high LCP values surrounding a central region of lower values. A short-axis slice of the ventricles showed that larger LCP values (>95%) were also observed over much of the endocardial surface, while most of the sub-surface myocardium had a much lower LCP (Fig. A.2A, sites c–e). Maps during failed defibrillation showed larger regions of low LCP values, especially in interior regions (Fig A.2B).

We next calculated the multilinear regression for surface and sub-surface LCP and VF termination. First, we found that sub-surface myocardial LCP was more closely

correlated with VF termination ($r = 0.98$, PVE $= 0.97$, $p < 10^{-13}$) than with surface LCP ($r = 0.81$, PVE $= 0.66$, $p < 10^{-4}$; the difference between correlations was also significant, $p < 10^{-5}$) (Fig. A.3). We found similar correlation values between surface LCP and VF termination as in optical mapping experiments of isolated hearts [126] ($p = 0.68$, not significantly different). These findings demonstrate that while both surface and sub-surface LCP were correlated with defibrillation success, LCP in the sub-surface myocardium was a better predictor of defibrillation success compared with LCP in the surface myocardium.

We additionally analyzed average LCP from the epicardial and endocardial surfaces separately. Mean values for the endocardial LCP are in general slightly smaller than the epicardial LCP, although the values are very close and the linear regression curves are almost the same (Fig. A.4, green and black circles, dotted lines). These results justify the collective analysis of the surface LCP values, as opposed to separate consideration of the epicardial and endocardial surfaces, and are consistent with sub-surface LCP as the best predictor of defibrillation success.

Figure A.2: Conduction block on the surface and sub-surface myocardium during HFAC fields[3]

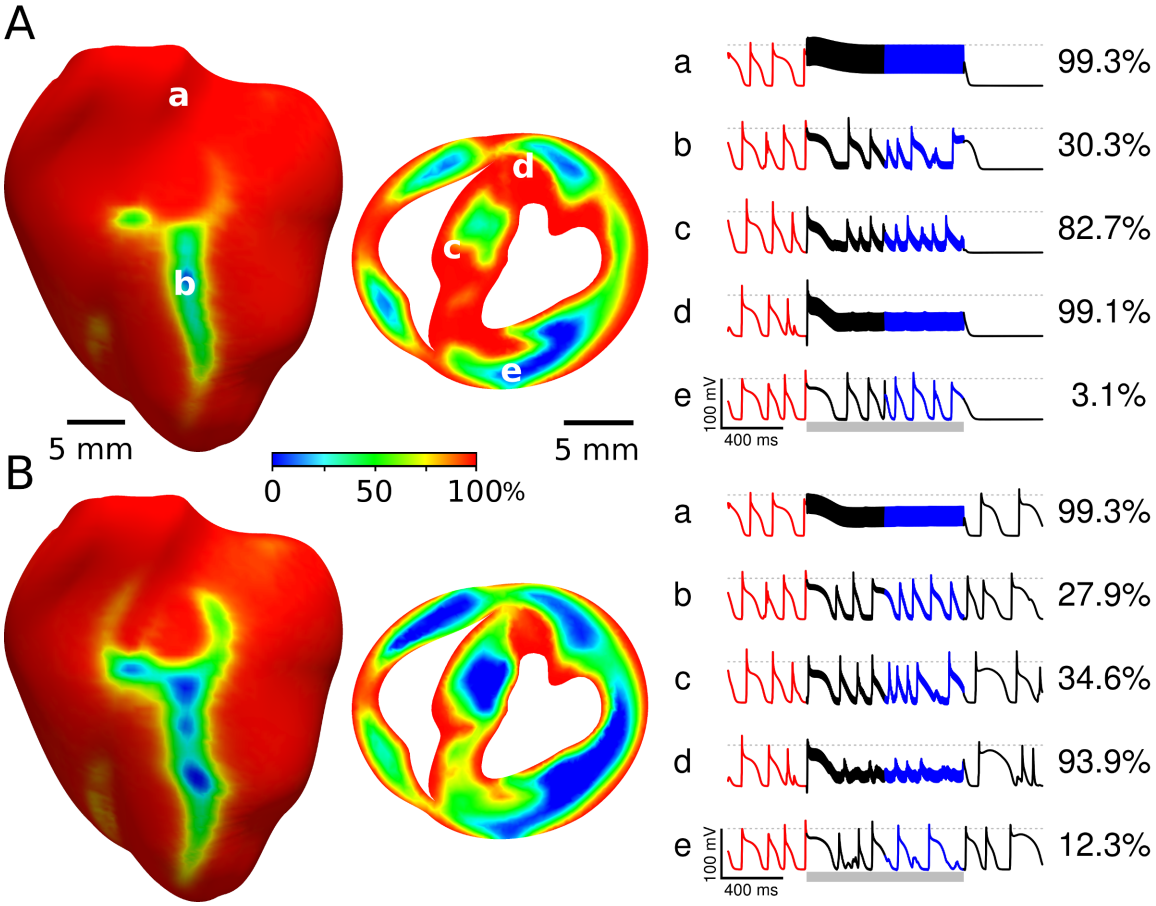

A. Successful and **B.** failed termination of ventricular fibrillation (VF). Spatial maps of loss of conduction power (LCP) on (left) the epicardial surface and (middle) a short-axis slice. (Right) V_m traces at sites a–e, shown in the spatial maps in panel A, with corresponding LCP values. Grey bar indicates time of the HFAC field. The time windows used for LCP analysis before and during the HFAC field are shown in red and blue, respectively.

[3]Reprinted from S. H. Weinberg, K. C. Chang, R. Zhu, H. Tandri, R. D. Berger, N. A. Trayanova, and L. Tung, "Defibrillation success with high frequency electric fields is related to degree and location of conduction block," *Heart Rhythm*, vol. 10, no. 5, pp. 740–748, may 2013, with permission from Elsevier.

Figure A.3: Surface and sub-surface conduction block and ventricular fibrillation vulnerability[4]

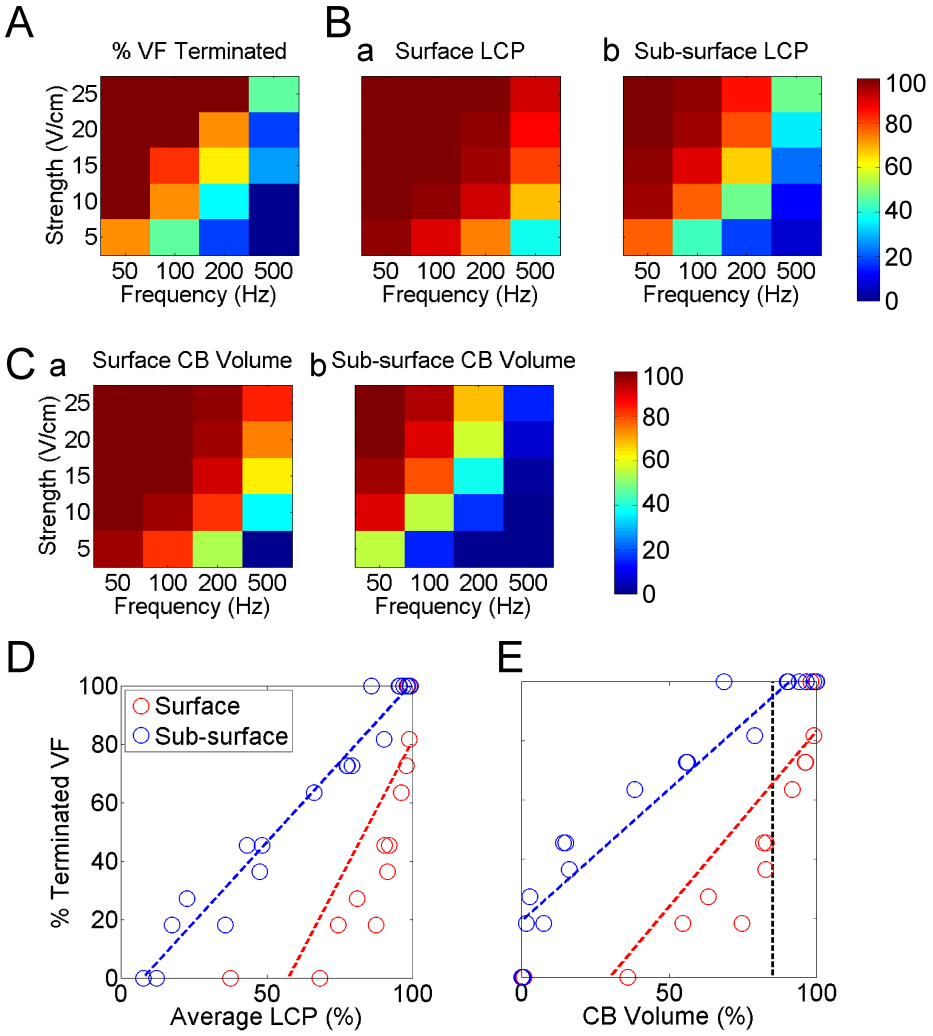

A. Percentage of simulations terminating ventricular fibrillation (VF), **B.** average (a) surface and (b) sub-surface loss of conduction power (LCP) values, and **C.** average (a) surface and (b) sub-surface conduction block (CB) size, as a function of field frequency and voltage. Correlation between **D.** average loss of conduction power (LCP) or **E.** CB size on the surface (red) or sub-surface (blue) myocardium and the percentage of simulations terminating VF.

[4]Reprinted from S. H. Weinberg, K. C. Chang, R. Zhu, H. Tandri, R. D. Berger, N. A. Trayanova, and L. Tung, "Defibrillation success with high frequency electric fields is related to degree and location of conduction block," *Heart Rhythm*, vol. 10, no. 5, pp. 740–748, may 2013, with permission from Elsevier.

Figure A.4: Relationships between average epicardial, endocardial and sub-surface loss of conduction power and ventricular fibrillation termination[5]

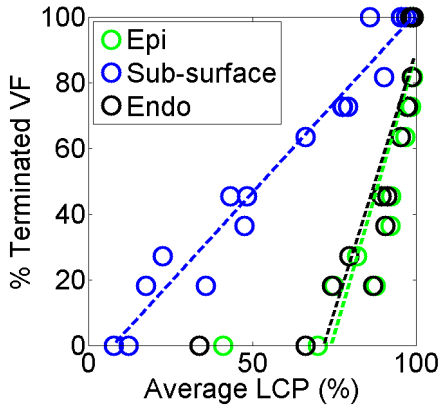

Correlation between the percentage of simulations terminating ventricular fibrillation (VF) and average loss of conduction power (LCP) in the epicardial (green), endocardial (black), and sub-surface (blue) myocardium.

A.3.3 Coupling and size of regions without conduction block in simulations

The simulations suggested that HFAC fields terminate arrhythmias by isolating regions in the sub-surface myocardial tissue without CB, thereby preventing reentrant waves from continuing after the applied field offset. To assess the field effect, we quantified the average number and size of regions without CB, as a function of field strength and frequency (Fig. A.5A). The uncoupling of these regions, as well as their

[5]Reprinted from S. H. Weinberg, K. C. Chang, R. Zhu, H. Tandri, R. D. Berger, N. A. Trayanova, and L. Tung, "Defibrillation success with high frequency electric fields is related to degree and location of conduction block," *Heart Rhythm*, vol. 10, no. 5, pp. 740–748, may 2013, with permission from Elsevier.

Figure A.5: Coupling and size of regions without conduction block[6]

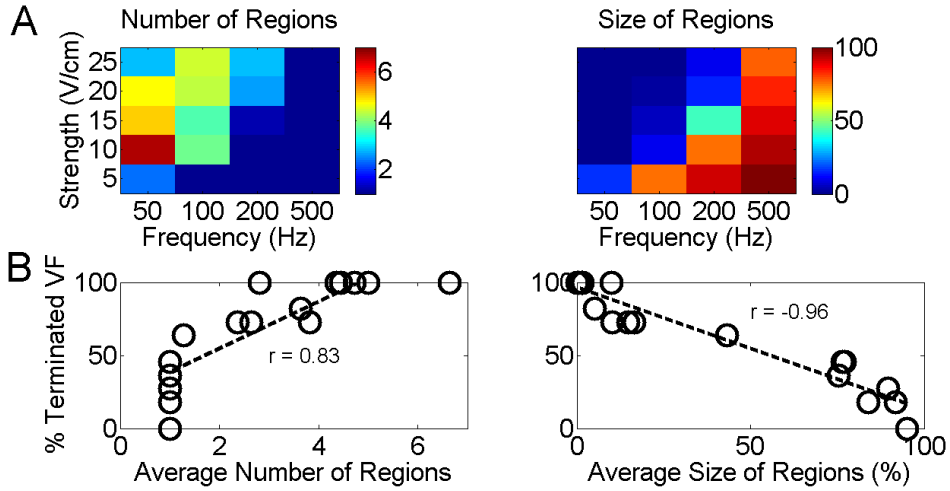

A. Average number and size of regions without conduction block (CB) as a function of field strength and frequency. **B.** Correlation between the average number and size of regions without CB and the percentage of simulations terminating ventricular fibrillation (VF).

size, depended greatly on field parameters. In general, at high field frequencies and low field strengths, there were fewer regions, but they were larger in size. As frequency decreased, these regions decreased in size, because total CB volume increased and because more regions became uncoupled from the main large compartment, resulting in a greater number of regions. Similar trends occurred as field strength increased, except that for 50-Hz HFAC fields, the number of regions decreased as field strength increased above 10 V/cm. This was due to the fact that smaller regions eventually disappeared as areas of CB expanded.

[6]Reprinted from S. H. Weinberg, K. C. Chang, R. Zhu, H. Tandri, R. D. Berger, N. A. Trayanova, and L. Tung, "Defibrillation success with high frequency electric fields is related to degree and location of conduction block," *Heart Rhythm*, vol. 10, no. 5, pp. 740–748, may 2013, with permission from Elsevier.

These trends were correlated with rates of successful defibrillation. Reentry during HFAC field was difficult to track in the simulations, as propagation arose from both preexisting reentrant wavefronts and from new activations occurring as a result of virtual electrode polarization (VEP). However, regardless of the source, defibrillation success increased as the total volume of block increased (Fig. A.3), and as the remaining tissue without CB became increasingly uncoupled into a larger number of smaller compartments (Fig. A.5B, $r = 0.83$ correlation between percentage of VF termination with number of regions; $r = -0.96$, size of regions). This suggests that successful HFAC fields defibrillate by surrounding sufficiently small excitable areas with regions of block, essentially "trapping" wavefronts and preventing them from "escaping" and initiating reentry.

A.4 Conclusion

HFAC fields terminate VF by maintaining V_m at an elevated, depolarized level that inactivates Na^+ channels and blocks conduction. Defibrillation success depends on the degree of conduction block on both the surface and sub-surface myocardium, and conduction block of sub-surface myocardium is the better predictor of defibrillation success.

Bibliography

[1] G. Tomaselli, "Electrophysiological remodeling in hypertrophy and heart failure," *Cardiovascular Research*, vol. 42, no. 2, pp. 270–283, may 1999.

[2] D. M. Bers, "Cardiac excitation–contraction coupling," *Nature*, vol. 415, no. 6868, pp. 198–205, jan 2002.

[3] Z. Qu, J. N. Weiss, and A. Garfinkel, "Cardiac electrical restitution properties and stability of reentrant spiral waves: a simulation study," *Am J Physiol Heart Circ Physiol*, vol. 276, no. 1, pp. H269–283, 1999.

[4] S. M. Narayan, "T-wave alternans and the susceptibility to ventricular arrhythmias." *Journal of the American College of Cardiology*, vol. 47, no. 2, pp. 269–81, jan 2006.

[5] S. M. Narayan, J. D. Bayer, G. Lalani, and N. A. Trayanova, "Action Potential Dynamics Explain Arrhythmic Vulnerability in Human Heart Failure. A Clinical and Modeling Study Implicating Abnormal Calcium Handling," *Journal of the American College of Cardiology*, vol. 52, no. 22, pp. 1782–1792, nov 2008.

[6] J. B. Nolasco and R. W. Dahlen, "A graphic method for the study of alternation in cardiac action potentials." *Journal of applied physiology*, vol. 25, no. 2, pp. 191–6, aug 1968.

[7] J. N. Weiss, A. Karma, Y. Shiferaw, P. S. Chen, A. Garfinkel, and Z. Qu, "From pulsus to pulseless: The saga of cardiac alternans," *Circulation Research*, vol. 98, no. 10, pp. 1244–1253, may 2006.

[8] L. Wang, R. C. Myles, N. M. De Jesus, A. K. P. Ohlendorf, D. M. Bers, and C. M. Ripplinger, "Optical mapping of sarcoplasmic reticulum Ca2+ in the intact heart: Ryanodine receptor refractoriness during alternans and fibrillation," *Circulation Research*, vol. 114, no. 9, pp. 1410–1421, feb 2014.

[9] M. A. Watanabe, F. H. Fenton, S. J. Evans, H. M. Hastings, and A. Karma, "Mechanisms for discordant alternans." *Journal of Cardiovascular Electrophysiology*, vol. 12, no. 2, pp. 196–206, feb 2001.

[10] S. S. Chugh, R. Havmoeller, K. Narayanan, D. Singh, M. Rienstra, E. J. Benjamin, R. F. Gillum, Y.-H. Kim, J. H. McAnulty, Z.-J. Zheng, M. H. Forouzanfar, M. Naghavi, G. A. Mensah, M. Ezzati, and C. J. L. Murray, "Worldwide Epidemiology of Atrial Fibrillation: A Global Burden of Disease 2010 Study," *Circulation*, vol. 129, no. 8, pp. 837–847, feb 2014.

[11] L. Fabritz, E. Guasch, C. Antoniades, I. Bardinet, G. Benninger, T. R. Betts, E. Brand, G. Breithardt, G. Bucklar-Suchankova, A. J. Camm, D. Cartlidge, B. Casadei, W. W. L. Chua, H. J. G. M. Crijns, J. Deeks, S. Hatem, F. Hidden-Lucet, S. Kääb, N. Maniadakis, S. Martin, L. Mont, H. Reinecke, M. F. Sinner, U. Schotten, T. Southwood, M. Stoll, P. Vardas, R. Wakili, A. West, A. Ziegler, and P. Kirchhof, "Expert consensus document: Defining the major health modifiers causing atrial fibrillation: a roadmap to underpin personalized prevention and treatment." *Nature reviews. Cardiology*, vol. 13, no. January 2016, pp. 230–237, 2015.

[12] C. M. Hanley, V. M. Robinson, and P. R. Kowey, "Status of Antiarrhythmic Drug Development for Atrial Fibrillation," *Circulation: Arrhythmia and Electrophysiology*, vol. 9, no. 3, p. e002479, mar 2016.

[13] N. Voigt, J. Heijman, Q. Wang, D. Y. Chiang, N. Li, M. Karck, X. H. T. Wehrens, S. Nattel, and D. Dobrev, "Cellular and molecular mechanisms of atrial arrhythmogenesis in patients with paroxysmal atrial fibrillation," *Circulation*, vol. 129, no. 2, pp. 145–156, nov 2014.

[14] N. Voigt, N. Li, Q. Wang, W. Wang, A. W. Trafford, I. Abu-Taha, Q. Sun, T. Wieland, U. Ravens, S. Nattel, X. H. T. Wehrens, and D. Dobrev, "Enhanced sarcoplasmic reticulum Ca2+ leak and increased Na+-Ca2+ exchanger function underlie delayed afterdepolarizations in patients with chronic atrial fibrillation." *Circulation*, vol. 125, no. 17, pp. 2059–70, may 2012.

[15] S. Nattel, B. Burstein, and D. Dobrev, "Atrial remodeling and atrial fibrillation: mechanisms and implications." *Circulation. Arrhythmia and electrophysiology*, vol. 1, no. 1, pp. 62–73, apr 2008.

[16] M. Haissaguerre, M. Hocini, A. Denis, A. J. Shah, Y. Komatsu, S. Yamashita, M. Daly, S. Amraoui, S. Zellerhoff, M.-Q. Picat, A. Quotb, L. Jesel, H. Lim, S. Ploux, P. Bordachar, G. Attuel, V. Meillet, P. Ritter, N. Derval, F. Sacher, O. Bernus, H. Cochet, P. Jais, and R. Dubois, "Driver domains in persistent atrial fibrillation." *Circulation*, vol. 130, no. 7, pp. 530–8, aug 2014.

[17] M. R. Franz, S. M. Jamal, and S. M. Narayan, "The role of action potential alternans in the initiation of atrial fibrillation in humans: A review and future directions," *Europace*, vol. 14, no. SUPPL. 5, pp. v58–64, nov 2012.

[18] S. M. Narayan, M. R. Franz, P. Clopton, E. J. Pruvot, and D. E. Krummen, "Repolarization alternans reveals vulnerability to human atrial fibrillation," *Circulation*, vol. 123, no. 25, pp. 2922–2930, jun 2011.

[19] N. A. Trayanova and K. C. Chang, "How computer simulations of the human heart can improve anti-arrhythmia therapy," *The Journal of Physiology*, vol. 594, no. 9, pp. 2483–2502, may 2016.

[20] A. L. Hodgkin and A. F. Huxley, "A quantitative description of membrane current and its application to conduction and excitation in nerve," *The Journal of Physiology*, vol. 117, no. 4, pp. 500–544, aug 1952.

[21] D. Noble, "A modification of the Hodgkin-Huxley equations applicable to Purkinje fibre action and pacemaker potentials," *The Journal of Physiology*, vol. 160, no. 2, pp. 317–352, feb 1962.

[22] D. Noble, "From the Hodgkin-Huxley axon to the virtual heart," *The Journal of Physiology*, vol. 580, no. 1, pp. 15–22, apr 2007.

[23] E. J. Vigmond, M. Hughes, G. Plank, and L. J. Leon, "Computational Tools for Modeling Electrical Activity in Cardiac Tissue," *Journal of Electrocardiology*, vol. 36, no. SUPPL., pp. 69–74, dec 2003.

[24] G. Plank, L. Zhou, J. L. Greenstein, S. Cortassa, R. L. Winslow, B. O'Rourke, and N. A. Trayanova, "From mitochondrial ion channels to arrhythmias in the heart: computational techniques to bridge the spatio-temporal scales." *Philosophical transactions. Series A, Mathematical, physical, and engineering sciences*, vol. 366, no. 1879, pp. 3381–3409, sep 2008.

[25] K. C. Chang, J. D. Bayer, and N. A. Trayanova, "Disrupted Calcium Release as a Mechanism for Atrial Alternans Associated with Human Atrial Fibrillation," *PLoS Computational Biology*, vol. 10, no. 12, p. e1004011, dec 2014.

[26] W. M. Feinberg, "Prevalence, Age Distribution, and Gender of Patients With Atrial Fibrillation," *Archives of Internal Medicine*, vol. 155, no. 5, p. 469, mar 1995.

[27] A. S. Go, E. M. Hylek, K. A. Phillips, Y. Chang, L. E. Henault, J. V. Selby, and D. E. Singer, "Prevalence of Diagnosed Atrial Fibrillation in Adults," *Jama*, vol. 285, no. 18, p. 2370, may 2001.

[28] K. S. Coyne, C. Paramore, S. Grandy, M. Mercader, M. Reynolds, and P. Zimetbaum, "Assessing the direct costs of treating nonvalvular atrial fibrillation in the United States," *Value in Health*, vol. 9, no. 5, pp. 348–356, 2006.

[29] S. Nattel, "New ideas about atrial fibrillation 50 years on." *Nature*, vol. 415, no. 6868, pp. 219–26, jan 2002.

[30] B.-S. Kim, Y.-H. Kim, G.-S. Hwang, H.-N. Pak, S. C. Lee, W. J. Shim, D. J. Oh, and Y. M. Ro, "Action potential duration restitution kinetics in human atrial fibrillation." *Journal of the American College of Cardiology*, vol. 39, no. 8, pp. 1329–36, apr 2002.

[31] S. M. Narayan, F. Bode, P. L. Karasik, and M. R. Franz, "Alternans of atrial action potentials during atrial flutter as a precursor to atrial fibrillation," *Circulation*, vol. 106, no. 15, pp. 1968–1973, sep 2002.

[32] K. Hiromoto, H. Shimizu, Y. Furukawa, T. Kanemori, T. Mine, T. Masuyama, and M. Ohyanagi, "Discordant repolarization alternans-induced atrial fibrillation is suppressed by verapamil." *Circulation journal : official journal of the Japanese Circulation Society*, vol. 69, no. 11, pp. 1368–1373, nov 2005.

[33] S. Nattel and D. Dobrev, "The multidimensional role of calcium in atrial fibrillation pathophysiology: Mechanistic insights and therapeutic opportunities," *European Heart Journal*, vol. 33, no. 15, pp. 1870–7, aug 2012.

[34] J. Heijman, N. Voigt, S. Nattel, and D. Dobrev, "Cellular and molecular electrophysiology of atrial fibrillation initiation, maintenance, and progression," *Circulation Research*, vol. 114, no. 9, pp. 1483–1499, apr 2014.

[35] J. D. Bayer, S. M. Narayan, G. G. Lalani, and N. A. Trayanova, "Rate-dependent action potential alternans in human heart failure implicates abnormal intracellular calcium handling," *Heart Rhythm*, vol. 7, no. 8, pp. 1093–1101, aug 2010.

[36] J. Hüser, Y. G. Wang, K. a. Sheehan, F. Cifuentes, S. L. Lipsius, and L. a. Blatter, "Functional coupling between glycolysis and excitation-contraction coupling underlies alternans in cat heart cells." *The Journal of physiology*, vol. 524 Pt 3, no. 3, pp. 795–806, may 2000.

[37] L. A. Blatter, J. Kockskämper, K. A. Sheehan, A. V. Zima, J. Hüser, and S. L. Lipsius, "Local calcium gradients during excitation-contraction coupling and alternans in atrial myocytes." *The Journal of physiology*, vol. 546, no. Pt 1, pp. 19–31, jul 2003.

[38] V. M. Shkryl, J. T. Maxwell, T. L. Domeier, and L. a. Blatter, "Refractoriness of sarcoplasmic reticulum Ca2+ release determines Ca2+ alternans in atrial myocytes," *AJP: Heart and Circulatory Physiology*, vol. 302, no. 11, pp. H2310–H2320, jun 2012.

[39] D. E. Krummen and S. M. Narayan, "Mechanisms for the initiation of human atrial fibrillation," *Heart Rhythm*, vol. 6, no. 8 SUPPL., pp. S12–6, aug 2009.

[40] E. Grandi, S. V. Pandit, N. Voigt, A. J. Workman, D. Dobrev, J. Jalife, and D. M. Bers, "Human atrial action potential and Ca2+ model: sinus rhythm and chronic atrial fibrillation." *Circulation research*, vol. 109, no. 9, pp. 1055–66, sep 2011.

[41] D. M. Harrild, C. S. Henriquez, and T. H. Atria, "CS, A Computer Model of Normal Conduction," *in the Human Atria, Circ Res, vol 87*, vol. 87, no. 7, pp. 25–36, sep 2000.

[42] D. E. Krummen, J. D. Bayer, J. Ho, G. Ho, M. R. Smetak, P. Clopton, N. A. Trayanova, and S. M. Narayan, "Mechanisms of human atrial fibrillation initiation clinical and computational studies of repolarization restitution and activation latency," *Circulation: Arrhythmia and Electrophysiology*, vol. 5, no. 6, pp. 1149–1159, oct 2012.

[43] O. Dössel, M. W. Krueger, F. M. Weber, M. Wilhelms, and G. Seemann, "Computational modeling of the human atrial anatomy and electrophysiology," *Medical & Biological Engineering & Computing*, vol. 50, no. 8, pp. 773–799, jun 2012.

[44] L.-H. Xie, D. Sato, A. Garfinkel, Z. Qu, and J. N. Weiss, "Intracellular Ca alternans: coordinated regulation by sarcoplasmic reticulum release, uptake, and leak," *Biophysical Journal*, vol. 95, no. 6, pp. 3100–10, sep 2008.

[45] J. G. Restrepo, J. N. Weiss, and A. Karma, "Calsequestrin-mediated mechanism for cellular calcium transient alternans." *Biophysical journal*, vol. 95, no. 8, pp. 3767–3789, oct 2008.

[46] Y. Shiferaw, M. A. Watanabe, A. Garfinkel, J. N. Weiss, and A. Karma, "Model of intracellular calcium cycling in ventricular myocytes." *Biophysical journal*, vol. 85, no. 6, pp. 3666–86, dec 2003.

[47] Z. Qu, Y. Shiferaw, and J. N. Weiss, "Nonlinear dynamics of cardiac excitation-contraction coupling: An iterated map study," *Physical Review E - Statistical, Nonlinear, and Soft Matter Physics*, vol. 75, no. 1, p. 011927, jan 2007.

[48] E. J. Vigmond, R. Weber dos Santos, A. J. Prassl, M. Deo, and G. Plank, "Solvers for the cardiac bidomain equations," *Progress in Biophysics and Molecular Biology*, vol. 96, no. 1-3, pp. 3–18, 2008.

[49] X. Wan, M. Cutler, Z. Song, A. Karma, T. Matsuda, A. Baba, and D. S. Rosenbaum, "New experimental evidence for mechanism of arrhythmogenic membrane potential alternans based on balance of electrogenic INCX/I Ca currents," *Heart Rhythm*, vol. 9, no. 10, pp. 1698–1705, oct 2012.

[50] M. E. Díaz, S. C. O'Neill, and D. A. Eisner, "Sarcoplasmic Reticulum Calcium Content Fluctuation Is the Key to Cardiac Alternans," *Circulation Research*, vol. 94, no. 5, pp. 650–656, mar 2004.

[51] E. A. Sobie and W. J. Lederer, "Dynamic local changes in sarcoplasmic reticulum calcium: Physiological and pathophysiological roles," *Journal of Molecular and Cellular Cardiology*, vol. 52, no. 2, pp. 304–311, feb 2012.

[52] P. B. Radwański, A. E. Belevych, L. Brunello, C. A. Carnes, and S. Györke, "Store-dependent deactivation: Cooling the chain-reaction of myocardial calcium signaling," *Journal of Molecular and Cellular Cardiology*, vol. 58, no. 1, pp. 77–83, may 2013.

[53] D. R. Laver, C. H. T. Kong, M. S. Imtiaz, and M. B. Cannell, "Termination of calcium-induced calcium release by induction decay: An emergent property of stochastic channel gating and molecular scale architecture," *Journal of Molecular and Cellular Cardiology*, vol. 54, no. 1, pp. 98–100, jan 2013.

[54] M. D. Stern, E. Ríos, and V. a. Maltsev, "Life and death of a cardiac calcium spark." *The Journal of general physiology*, vol. 142, no. 3, pp. 257–74, sep 2013.

[55] D. Sato and D. M. Bers, "How does stochastic ryanodine receptor-mediated Ca leak fail to initiate a Ca spark?" *Biophysical Journal*, vol. 101, no. 10, pp. 2370–2379, nov 2011.

[56] E. A. Sobie, "Parameter sensitivity analysis in electrophysiological models using multivariable regression," *Biophysical Journal*, vol. 96, no. 4, pp. 1264–1274, feb 2009.

[57] Y. Miyauchi, S. Zhou, Y. Okuyama, M. Miyauchi, H. Hayashi, A. Hamabe, M. C. Fishbein, W. J. Mandel, L. S. Chen, P. S. Chen, and H. S. Karagueuzian, "Altered atrial electrical restitution and heterogeneous sympathetic hyperinnervation in hearts with chronic left ventricular myocardial infarction: Implications for atrial fibrillation," *Circulation*, vol. 108, no. 3, pp. 360–366, jul 2003.

[58] S. Kettlewell, F. L. Burton, G. L. Smith, and A. J. Workman, "Chronic myocardial infarction promotes atrial action potential alternans, afterdepolarizations, and fibrillation," *Cardiovascular Research*, vol. 99, no. 1, pp. 215–224, jul 2013.

[59] F. Jousset, J. Tenkorang, J. M. Vesin, P. Pascale, P. Ruchat, A. G. Rollin, M. Fromer, S. M. Narayan, and E. Pruvot, "Kinetics of atrial repolarization alternans in a free-behaving ovine model," *Journal of Cardiovascular Electrophysiology*, vol. 23, no. 9, pp. 1003–1012, sep 2012.

[60] J. Monigatti-Tenkorang, F. Jousset, P. Pascale, J. M. Vesin, P. Ruchat, M. Fromer, S. M. Narayan, and E. Pruvot, "Intermittent atrial tachycardia promotes repolarization alternans and conduction slowing during rapid rates, and increases susceptibility to atrial fibrillation in a free-behaving sheep model," *Journal of Cardiovascular Electrophysiology*, vol. 25, no. 4, pp. 418–427, jan 2014.

[61] J. Kockskämper, A. V. Zima, and L. A. Blatter, "Modulation of sarcoplasmic reticulum Ca2+ release by glycolysis in cat atrial myocytes." *The Journal of physiology*, vol. 564, no. Pt 3, pp. 697–714, may 2005.

[62] W. Xie, G. Santulli, X. Guo, M. Gao, B. X. Chen, and A. R. Marks, "Imaging atrial arrhythmic intracellular calcium in intact heart," *Journal of Molecular and Cellular Cardiology*, vol. 64, pp. 120–123, 2013.

[63] L. M. Livshitz and Y. Rudy, "Regulation of Ca2+ and electrical alternans in cardiac myocytes: role of CAMKII and repolarizing currents." *American journal of physiology. Heart and circulatory physiology*, vol. 292, no. 6, pp. H2854–66, jun 2007.

[64] A. E. Belevych, D. Terentyev, S. Viatchenko-Karpinski, R. Terentyeva, A. Sridhar, Y. Nishijima, L. D. Wilson, A. J. Cardounel, K. R. Laurita, C. A. Carnes, G. E. Billman, and S. Gyorke, "Redox modification of ryanodine receptors underlies calcium alternans in a canine model of sudden cardiac death," *Cardiovascular Research*, vol. 84, no. 3, pp. 387–395, dec 2009.

[65] D. Dobrev, N. Voigt, and X. H. T. Wehrens, "The ryanodine receptor channel as a molecular motif in atrial fibrillation: Pathophysiological and therapeutic implications," *Cardiovascular Research*, vol. 89, no. 4, pp. 734–743, mar 2011.

[66] S. O. Marx and A. R. Marks, "Dysfunctional ryanodine receptors in the heart: New insights into complex cardiovascular diseases," *Journal of Molecular and Cellular Cardiology*, vol. 58, no. 1, pp. 225–231, may 2013.

[67] K. R. Laurita and D. S. Rosenbaum, "Cellular mechanisms of arrhythmogenic cardiac alternans," *Progress in Biophysics and Molecular Biology*, vol. 97, no. 2-3, pp. 332–347, 2008.

[68] D. Dobrev and X. H. T. Wehrens, "Role of RyR2 phosphorylation in heart failure and arrhythmias: Controversies around ryanodine receptor phosphorylation in cardiac disease," *Circulation Research*, vol. 114, no. 8, pp. 1311–1319, apr 2014.

[69] S. R. Houser, "Role of RyR2 Phosphorylation in Heart Failure and Arrhythmias: Protein Kinase A-Mediated Hyperphosphorylation of the Ryanodine Receptor at Serine 2808 Does Not Alter Cardiac Contractility or Cause Heart Failure and Arrhythmias," *Circulation Research*, vol. 114, no. 8, pp. 1320–1327, apr 2014.

[70] J. J. Arnáiz-Cot, B. J. Damon, X.-H. Zhang, L. Cleemann, N. Yamaguchi, G. Meissner, and M. Morad, "Cardiac calcium signalling pathologies associated with defective calmodulin regulation of type 2 ryanodine receptor." *The Journal of physiology*, vol. 591, no. 17, pp. 4287–99, jul 2013.

[71] M. Mayr, S. Yusuf, G. Weir, Y.-L. Chung, U. Mayr, X. Yin, C. Ladroue, B. Madhu, N. Roberts, A. De Souza, S. Fredericks, M. Stubbs, J. R. Griffiths, M. Jahangiri, Q. Xu, and a. J. Camm, "Combined metabolomic and proteomic analysis of human atrial fibrillation." *Journal of the American College of Cardiology*, vol. 51, no. 5, pp. 585–594, feb 2008.

[72] A. I. De Souza, S. Cardin, R. Wait, Y. L. Chung, M. Vijayakumar, A. Maguy, A. J. Camm, and S. Nattel, "Proteomic and metabolomic analysis of atrial profibrillatory remodelling in congestive heart failure," *Journal of Molecular and Cellular Cardiology*, vol. 49, no. 5, pp. 851–863, jul 2010.

[73] A. Kourliouros, X. Yin, A. Didangelos, M. T. Hosseini, O. Valencia, M. Mayr, and M. Jahangiri, "Substrate modifications precede the development of atrial fibrillation after cardiac surgery: A proteomic study," *Annals of Thoracic Surgery*, vol. 92, no. 1, pp. 104–110, jul 2011.

[74] E. Picht, J. DeSantiago, L. A. Blatter, and D. M. Bers, "Cardiac alternans do not rely on diastolic sarcoplasmic reticulum calcium content fluctuations," *Circulation Research*, vol. 99, no. 7, pp. 740–748, sep 2006.

[75] R. Rovetti, X. Cui, A. Garfinkel, J. N. Weiss, and Z. Qu, "Spark-induced sparks as a mechanism of intracellular calcium alternans in cardiac myocytes," *Circulation Research*, vol. 106, no. 10, pp. 1582–1591, may 2010.

[76] E. Alvarez-Lacalle, I. R. Cantalapiedra, A. Peñaranda, J. Cinca, L. Hove-Madsen, and B. Echebarria, "Dependency of Calcium Alternans on Ryanodine Receptor Refractoriness," *PLoS ONE*, vol. 8, no. 2, p. e55042, jan 2013.

[77] C. a. Lugo, I. R. Cantalapiedra, A. Peñaranda, L. Hove-Madsen, and B. Echebarria, "Are SR Ca content fluctuations or SR refractoriness the key

to atrial cardiac alternans?: insights from a human atrial model." *American journal of physiology. Heart and circulatory physiology*, vol. 306, no. 11, pp. H1540–52, mar 2014.

[78] M. Frisk, J. T. Koivumaki, P. A. Norseng, M. M. Maleckar, O. M. Sejersted, and W. E. Louch, "Variable t-tubule organization and Ca2+ homeostasis across the atria," *Am J Physiol Heart Circ Physiol*, vol. 307, no. 4, pp. H609–20, jun 2014.

[79] R. Thul, S. Coombes, H. L. Roderick, and M. D. Bootman, "Subcellular calcium dynamics in a whole-cell model of an atrial myocyte," *Proceedings of the National Academy of Sciences*, vol. 109, no. 6, pp. 2150–2155, feb 2012.

[80] Q. Li, S. C. O'Neill, T. Tao, Y. Li, D. Eisner, and H. Zhang, "Mechanisms by which cytoplasmic calcium wave propagation and alternans are generated in cardiac atrial myocytes lacking t-tubules-insights from a simulation study," *Biophysical Journal*, vol. 102, no. 7, pp. 1471–1482, apr 2012.

[81] J. T. Koivumäki, T. Korhonen, and P. Tavi, "Impact of sarcoplasmic reticulum calcium release on calcium dynamics and action potential morphology in human atrial myocytes: A computational study," *PLoS Computational Biology*, vol. 7, no. 1, p. e1001067, jan 2011.

[82] T. Krogh-Madsen, G. W. Abbott, and D. J. Christini, "Effects of electrical and structural remodeling on atrial fibrillation maintenance: A simulation study," *PLoS Computational Biology*, vol. 8, no. 2, p. e1002390, feb 2012.

[83] K. S. McDowell, F. Vadakkumpadan, R. Blake, J. Blauer, G. Plank, R. S. Macleod, and N. A. Trayanova, "Mechanistic inquiry into the role of tissue remodeling in fibrotic lesions in human atrial fibrillation," *Biophysical Journal*, vol. 104, no. 12, pp. 2764–2773, jun 2013.

[84] Z. Qu, A. Garfinkel, P.-S. Chen, and J. N. Weiss, "Mechanisms of Discordant Alternans and Induction of Reentry in Simulated Cardiac Tissue," *Circulation*, vol. 102, no. 14, pp. 1664–1670, oct 2000.

[85] A. Defauw, I. V. Kazbanov, H. Dierckx, P. Dawyndt, and A. V. Panfilov, "Action potential duration heterogeneity of cardiac tissue can be evaluated from cell properties using Gaussian Green's function approach," *PLoS ONE*, vol. 8, no. 11, p. e79607, jan 2013.

[86] P. N. Jordan and D. J. Christini, "Characterizing the contribution of voltage- and calcium-dependent coupling to action potential stability: implications for repolarization alternans." *American journal of physiology. Heart and circulatory physiology*, vol. 293, no. 4, pp. H2109–18, oct 2007.

[87] C. H. Luo and Y. Rudy, "A dynamic model of the cardiac ventricular action potential. I. Simulations of ionic currents and concentration changes." *Circulation research*, vol. 74, no. 6, pp. 1071–96, jun 1994.

[88] M. Deo, Y. Ruan, S. V. Pandit, K. Shah, O. Berenfeld, A. Blaufox, M. Cerrone, S. F. Noujaim, M. Denegri, J. Jalife, and S. G. Priori, "KCNJ2 mutation in short QT syndrome 3 results in atrial fibrillation and ventricular proarrhythmia." *Proceedings of the National Academy of Sciences of the United States of America*, vol. 110, no. 11, pp. 4291–6, mar 2013.

[89] A. J. Workman, K. A. Kane, and A. C. Rankin, "The contribution of ionic currents to changes in refractoriness of human atrial myocytes associated with chronic atrial fibrillation," *Cardiovascular Research*, vol. 52, no. 2, pp. 226–235, nov 2001.

[90] M. Courtemanche, R. J. Ramirez, and S. Nattel, "Ionic mechanisms underlying human atrial action potential properties: insights from a mathematical model," *Am J Physiol Heart Circ Physiol*, vol. 275, no. 1, pp. H301–321, 1998.

[91] A. X. Sarkar, D. J. Christini, and E. A. Sobie, "Exploiting mathematical models to illuminate electrophysiological variability between individuals." *The Journal of physiology*, vol. 590, no. Pt 11, pp. 2555–67, jun 2012.

[92] V. M. Spitzer and D. G. Whitlock, "The Visible Human Dataset: the anatomical platform for human simulation." *The Anatomical record*, vol. 253, no. 2, pp. 49–57, apr 1998.

[93] M. A. Colman, O. V. Aslanidi, S. Kharche, M. R. Boyett, C. Garratt, J. C. Hancox, and H. Zhang, "Pro-arrhythmogenic effects of atrial fibrillation-induced electrical remodelling: insights from the three-dimensional virtual human atria." *The Journal of physiology*, vol. 591, no. Pt 17, pp. 4249–72, sep 2013.

[94] K. T. Konings, C. J. Kirchhof, J. R. Smeets, H. J. Wellens, O. C. Penn, and M. A. Allessie, "High-density mapping of electrically induced atrial fibrillation in humans." *Circulation*, vol. 89, no. 4, pp. 1665–80, apr 1994.

[95] Y. Gong, F. Xie, K. M. Stein, A. Garfinkel, C. A. Culianu, B. B. Lerman, and D. J. Christini, "Mechanism Underlying Initiation of Paroxysmal Atrial Flutter/Atrial Fibrillation by Ectopic Foci: A Simulation Study," *Circulation*, vol. 115, no. 16, pp. 2094–2102, apr 2007.

[96] D. R. Van Wagoner, A. L. Pond, M. Lamorgese, S. S. Rossie, P. M. McCarthy, and J. M. Nerbonne, "Atrial L-Type Ca2+ Currents and Human Atrial Fibrillation," *Circulation Research*, vol. 85, no. 5, pp. 428–436, sep 1999.

[97] M. W. Krueger, V. Schmidt, C. Tobón, F. M. Weber, C. Lorenz, D. U. J. Keller, H. Barschdorf, M. Burdumy, P. Neher, G. Plank, K. Rhode, G. Seemann, D. Sanchez-Quintana, J. Saiz, R. Razavi, and O. Dossel, "Modeling Atrial Fiber Orientation in Patient-Specific Geometries: A Semi-automatic Rule-Based Approach," in *Functional Imaging and Modeling of the Heart*, ser. Lecture Notes in Computer Science, D. N. Metaxas and L. Axel, Eds. Springer Berlin Heidelberg, 2011, vol. 6666, pp. 223–232.

[98] A. Karma, "Electrical alternans and spiral wave breakup in cardiac tissue." *Chaos*, vol. 4, no. 3, pp. 461–472, 1994.

[99] R. H. Clayton, E. A. Zhuchkova, and A. V. Panfilov, "Phase singularities and filaments: simplifying complexity in computational models of ventricular fibrillation." *Progress in biophysics and molecular biology*, vol. 90, no. 1-3, pp. 378–98, jan 2006.

[100] M. Hubert and E. Vandervieren, "An adjusted boxplot for skewed distributions," *Computational Statistics & Data Analysis*, vol. 52, no. 12, pp. 5186–5201, aug 2008.

[101] N. Cressie and T. R. C. Read, "Multinomial Goodness-of-Fit Tests," *Journal of the Royal Statistical Society. Series B (Methodological)*, vol. 46, no. 3, pp. 440–464, 1984.

[102] R. R. Wilcox, "Wilcox' Robust Statistics," 2016. [Online]. Available: http://dornsife.usc.edu/labs/rwilcox/software/

[103] R. R. Wilcox, "Comparing Pearson Correlations: Dealing with Heteroscedasticity and Nonnormality," *Communications in Statistics - Simulation and Computation*, vol. 38, no. 10, pp. 2220–2234, nov 2009.

[104] J. Jalife, "Mother rotors and fibrillatory conduction: a mechanism of atrial fibrillation," *Cardiovascular Research*, vol. 54, no. 2, pp. 204–216, may 2002.

[105] N. A. Trayanova, "Mathematical approaches to understanding and imaging atrial fibrillation: significance for mechanisms and management." *Circulation research*, vol. 114, no. 9, pp. 1516–31, apr 2014.

[106] C. Tobón, C. A. Ruiz-Villa, E. Heidenreich, L. Romero, F. Hornero, and J. Saiz, "A three-dimensional human atrial model with fiber orientation. Electrograms and arrhythmic activation patterns relationship." *PloS one*, vol. 8, no. 2, p. e50883, jan 2013.

[107] U. Schotten, D. Dobrev, P. G. Platonov, H. Kottkamp, and G. Hindricks, "Current controversies in determining the main mechanisms of atrial fibrillation." *Journal of internal medicine*, vol. 279, no. 5, pp. 428–38, may 2016.

[108] J. G. Quintanilla, J. Pérez-Villacastín, N. Pérez-Castellano, S. V. Pandit, O. Berenfeld, J. Jalife, and D. Filgueiras-Rama, "Mechanistic Approaches to Detect, Target, and Ablate the Drivers of Atrial Fibrillation," *Circulation: Arrhythmia and Electrophysiology*, vol. 9, no. 1, p. e002481, jan 2016.

[109] M. W. Krueger, K. S. Rhode, M. D. O'Neill, C. A. Rinaldi, J. Gill, R. Razavi, G. Seemann, and O. Doessel, "Patient-specific modeling of atrial fibrosis increases the accuracy of sinus rhythm simulations and may explain maintenance of atrial fibrillation," *Journal of Electrocardiology*, vol. 47, no. 3, pp. 324–328, 2014.

[110] S. Zahid, H. Cochet, P. M. Boyle, E. L. Schwarz, K. N. Whyte, E. J. Vigmond, R. Dubois, M. Hocini, M. Haïssaguerre, P. Jaïs, and N. A. Trayanova, "Patient-derived models link re-entrant driver localization in atrial fibrillation to fibrosis spatial pattern," *Cardiovascular Research*, vol. 110, no. 3, pp. 443–454, jun 2016.

[111] F. Pashakhanloo, D. A. Herzka, H. Ashikaga, S. Mori, N. Gai, D. A. Bluemke, N. A. Trayanova, and E. R. McVeigh, "Myofiber Architecture of the Human Atria as Revealed by Submillimeter Diffusion Tensor Imaging," *Circulation: Arrhythmia and Electrophysiology*, vol. 9, no. 4, p. e004133, apr 2016.

[112] M. J. Gonzales, K. P. Vincent, W.-J. Rappel, S. M. Narayan, and A. D. McCulloch, "Structural contributions to fibrillatory rotors in a patient-derived computational model of the atria." *Europace : European pacing, arrhythmias, and cardiac electrophysiology : journal of the working groups on cardiac pacing, arrhythmias, and cardiac cellular electrophysiology of the European Society of Cardiology*, vol. 16 Suppl 4, no. suppl_4, pp. iv3–iv10, nov 2014.

[113] R. Majumder, M. C. Engels, A. A. F. de Vries, A. V. Panfilov, and D. A. Pijnappels, "Islands of spatially discordant APD alternans underlie arrhythmogenesis by promoting electrotonic dyssynchrony in models of fibrotic rat ventricular myocardium." *Scientific reports*, vol. 6, p. 24334, jan 2016.

[114] I. V. Kazbanov, K. H. W. J. Ten Tusscher, and A. V. Panfilov, "Effects of Heterogeneous Diffuse Fibrosis on Arrhythmia Dynamics and Mechanism." *Scientific reports*, vol. 6, p. 20835, jan 2016.

[115] F. Xiong, T. Liu, X.-Y. Qi, W. Zhou, P. Comtois, C. Huang, D. Dobrev, and S. Nattel, "Ryanodine Receptor Refractoriness Changes as a Path to Reentry-promoting Alternans in Atrial Fibrillation Related Remodeling," in *Heart Rhythm*, vol. 13, no. 5, may 2016, pp. S166–S250.

[116] T. Liu, F. Xiong, X.-Y. Qi, Y. Sobue, W. Zhou, C. Huang, D. Dobrev, and S. Nattel, "Dantrolene Prevents Atrial Fibrillation Induction in a Tachycardia-Remodeled Substrate by Stabilizing Ryanodine Receptors," in *Heart Rhythm*, vol. 13, no. 5, may 2016, p. S7.

[117] C. E. Molina, A. Llach, A. Herraiz-Martínez, C. Tarifa, M. Barriga, R. F. Wiegerinck, J. Fernandes, N. Cabello, A. Vallmitjana, R. Benitéz, J. Montiel, J. Cinca, and L. Hove-Madsen, "Prevention of adenosine A2A receptor activation diminishes beat-to-beat alternation in human atrial myocytes," *Basic Research in Cardiology*, vol. 111, no. 1, p. 5, jan 2016.

[118] G. Meissner, "Molecular regulation of cardiac ryanodine receptor ion channel," *Cell Calcium*, vol. 35, no. 6, pp. 621–628, 2004.

[119] X.-D. Zhang, D. K. Lieu, and N. Chiamvimonvat, "Small-conductance Ca(2+)-activated K(+) channels and cardiac arrhythmias." *Heart rhythm : the official journal of the Heart Rhythm Society*, vol. 12, no. 8, pp. 1845–1851, 2015.

[120] B. O. Bingen, Z. Neshati, S. F. A. Askar, I. V. Kazbanov, D. L. Ypey, A. V. Panfilov, M. J. Schalij, A. A. F. de Vries, and D. A. Pijnappels, "Atrium-Specific Kir3.x Determines Inducibility, Dynamics and Termination of Fibrillation by Regulating Restitution-Driven Alternans," *Circulation*, vol. 128, no. 25, pp. 2732–44, sep 2013.

[121] H. Fuller, F. Justo, B. D. Nearing, K. M. Kahlig, S. Rajamani, L. Belardinelli, and R. L. Verrier, "Eleclazine, a new selective cardiac late sodium current inhibitor, confers concurrent protection against autonomically induced atrial premature beats, repolarization alternans and heterogeneity, and atrial fibrillation in an intact porcine model," *Heart Rhythm*, apr 2016.

[122] A. N. Iyer and R. A. Gray, "An Experimentalist's Approach to Accurate Localization of Phase Singularities during Reentry," *Annals of Biomedical Engineering*, vol. 29, no. 1, pp. 47–59, jan 2001.

[123] C. Larson, L. Dragnev, and N. Trayanova, "Analysis of Electrically Induced Reentrant Circuits in a Sheet of Myocardium," *Annals of Biomedical Engineering*, vol. 31, no. 7, pp. 768–780, jul 2003.

[124] R. H. Clayton and A. V. Holden, "A method to quantify the dynamics and complexity of re-entry in computational models of ventricular fibrillation." *Physics in medicine and biology*, vol. 47, no. 2, pp. 225–238, 2002.

[125] H. Tandri, S. H. Weinberg, K. C. Chang, R. Zhu, N. A. Trayanova, L. Tung, and R. D. Berger, "Reversible cardiac conduction block and defibrillation with

high-frequency electric field." *Science translational medicine*, vol. 3, no. 102, p. 102ra96, sep 2011.

[126] S. H. Weinberg, K. C. Chang, R. Zhu, H. Tandri, R. D. Berger, N. A. Trayanova, and L. Tung, "Defibrillation success with high frequency electric fields is related to degree and location of conduction block," *Heart Rhythm*, vol. 10, no. 5, pp. 740–748, may 2013.

[127] M. J. Bishop, B. Rodriguez, F. Qu, I. R. Efimov, D. J. Gavaghan, and N. A. Trayanova, "The Role of Photon Scattering in Optical Signal Distortion during Arrhythmia and Defibrillation," *Biophysical Journal*, vol. 93, no. 10, pp. 3714–3726, nov 2007.

[128] T. Ashihara, J. Constantino, and N. A. Trayanova, "Tunnel propagation of postshock activations as a hypothesis for fibrillation induction and isoelectric window." *Circulation research*, vol. 102, no. 6, pp. 737–45, mar 2008.

[129] B. Rodríguez, L. Li, J. C. Eason, I. R. Efimov, and N. A. Trayanova, "Differences between left and right ventricular chamber geometry affect cardiac vulnerability to electric shocks." *Circulation research*, vol. 97, no. 2, pp. 168–75, jul 2005.

[130] R. Plonsey, "Bioelectric sources arising in excitable fibers (ALZA lecture)." *Annals of biomedical engineering*, vol. 16, no. 6, pp. 519–46, 1988.

[131] C. H. Luo and Y. Rudy, "A model of the ventricular cardiac action potential. Depolarization, repolarization, and their interaction." *Circulation research*, vol. 68, no. 6, pp. 1501–26, jun 1991.

[132] T. Ashihara and N. A. Trayanova, "Cell and tissue responses to electric shocks." *Europace : European pacing, arrhythmias, and cardiac electrophysiology : journal of the working groups on cardiac pacing, arrhythmias, and cardiac cellular electrophysiology of the European Society of Cardiology*, vol. 7 Suppl 2, no. s2, pp. 155–65, sep 2005.

[133] D. K. Cheng, L. Tung, and E. A. Sobie, "Nonuniform responses of transmembrane potential during electric field stimulation of single cardiac cells." *The American journal of physiology*, vol. 277, no. 1 Pt 2, pp. H351–62, jul 1999.

[134] K. A. DeBruin and W. Krassowska, "Electroporation and Shock-Induced Transmembrane Potential in a Cardiac Fiber During Defibrillation Strength Shocks," *Annals of Biomedical Engineering*, vol. 26, no. 4, pp. 584–596, jul 1998.

[135] N. Trayanova, J. Eason, and F. Aguel, "Computer simulations of cardiac defibrillation: a look inside the heart," *Computing and Visualization in Science*, vol. 4, no. 4, pp. 259–270, jul 2002.

[136] G. Plank, M. Liebmann, R. Weber dos Santos, E. J. Vigmond, and G. Haase, "Algebraic multigrid preconditioner for the cardiac bidomain model." *IEEE transactions on bio-medical engineering*, vol. 54, no. 4, pp. 585–96, apr 2007.

[137] E. J. Vigmond, F. Aguel, and N. A. Trayanova, "Computational techniques for solving the bidomain equations in three dimensions." *IEEE transactions on bio-medical engineering*, vol. 49, no. 11, pp. 1260–9, nov 2002.

[138] N. Trayanova, "Concepts of ventricular defibrillation," *Philosophical Transactions of the Royal Society A: Mathematical, Physical and Engineering Sciences*, vol. 359, no. 1783, pp. 1327–1337, jun 2001.

[139] N. Trayanova, K. Skouibine, and F. Aguel, "The role of cardiac tissue structure in defibrillation," *Chaos: An Interdisciplinary Journal of Nonlinear Science*, vol. 8, no. 1, p. 221, 1998.

[140] J. H. Steiger, "Tests for comparing elements of a correlation matrix." *Psychological Bulletin*, vol. 87, no. 2, pp. 245–251, 1980.

[141] I. R. Efimov, Y. Cheng, Y. Yamanouchi, and P. J. Tchou, "Direct evidence of the role of virtual electrode-induced phase singularity in success and failure of defibrillation." *Journal of cardiovascular electrophysiology*, vol. 11, no. 8, pp. 861–8, aug 2000.

Abbreviations

AF	atrial fibrillation
ALT_{fast}	human atria model with alternans onset at fast rates
ALT_{slow}	human atria model with alternans onset at slow rates
ANM	APD alternans normalized magnitude
AP	action potential
APD	action potential duration
AVN	atrioventricular node
cAF	chronic AF
cAF_{alt}	ionic model of cAF cell with slow-rate alternans
CaT	Ca^{2+} transient
CDA	Ca^{2+}-driven alternans
CI	coupling interval
CICR	Ca^{2+}-induced Ca^{2+} release

ABBREVIATIONS

CL	cycle length
CSQN	calsequestrin
CV	conduction velocity
DAD	delayed afterdepolarization
DI	diastolic interval
EAD	early afterdepolarization
EC	excitation–contraction
FT	filament tree
GPV	Grandi-Pandit-Voigt human atrial action potential model
GPVm	modified GPV model
JSR	junctional sarcoplasmic reticulum
LA	left atrium
LRd	Luo-Rudy dynamic model
LV	left ventricle
NCX	Na^+/Ca^{2+} exchanger
NSR	network sarcoplasmic reticulum
PS	phase singularity
PV	pulmonary vein
RA	right atrium

ABBREVIATIONS

RSPV	right superior pulmonary vein
RV	right ventricle
RyR2	ryanodine receptor
SAN	sinoatrial node
SD	standard deviation
SERCA	sarco/endoplasmic reticulum Ca^{2+}-ATPase
SR	sarcoplasmic reticulum
VF	ventricular fibrillation

Symbols

I_{CaL}	L-type Ca^{2+} current
I_{K1}	inward rectifier K^+ current
I_{Kr}	delayed rectifier K^+ current
$I_{NCX_{sl}}$	sub-sarcolemmal Na^+/Ca^{2+} exchanger (NCX) current
I_{NCX}	NCX current
I_{NaK}	Na^+/K^+ current
I_{NaL}	late Na^+ current
I_{Na}	fast Na^+ current
I_{to}	transient outward K^+ current
J_{SERCA}	sarcoplasmic reticulum (SR) Ca^{2+} uptake flux
$J_{SRCa_{rel}}$	SR Ca^{2+} release flux
K_{mf}	K_m for SERCA pump in forward mode
RyR_i	RyR2 inactivated probability

SYMBOLS

RyR_o	RyR2 open probability
V_m	transmembrane potential
$V_{maxSRCaP}$	V_{max} of SERCA pump
$\Delta[Ca^{2+}]_i$	intracellular Ca^{2+} transient amplitude
$\bar{I}_{NCX}$	maximal NCX current
$\bar{g}_{CaL}$	maximum L-type Ca^{2+} current conductance
$\bar{g}_{K1}$	maximum inward rectifier K^+ current conductance
$\bar{g}_{Kr}$	maximum delayed rectifier K^+ current conductance
$\bar{g}_{Ks}$	maximum slowly activating delayed rectifier K^+ current conductance
$\bar{g}_{Kur}$	maximum ultra-rapid delayed rectifier K^+ current conductance
$\bar{g}_{NaL}$	maximum late Na^+ current conductance
$\bar{g}_{Na}$	maximum fast Na^+ current conductance
$\bar{g}_{to}$	maximum transient outward K^+ current conductance
κ	sarcolemmal Ca^{2+} efflux factor
τ_f	L-type Ca^{2+} current voltage-dependent inactivation time constant
τ_{fCa}	L-type Ca^{2+} current Ca^{2+}-dependent inactivation time constant
ec_{50SR}	EC_{50} for luminal Ca^{2+} dependence of RyR2
k_{leak}	SR Ca^{2+} leak rate constant
k_s	SR Ca^{2+} release rate constant

ki_{Ca}	RyR2 inactivation rate constant
ki_m	transition rate constant for RyR2
ko_{Ca}	RyR2 activation rate constant
ko_m	transition rate constant for RyR2
m	SR Ca^{2+} release slope
u	SR Ca^{2+} uptake factor
$[Ca^{2+}]_{SR}$	SR Ca^{2+} concentration
$[Ca^{2+}]_i$	intracellular Ca^{2+} concentration
$[Ca^{2+}]_j$	junctional Ca^{2+} concentration
$[Ca^{2+}]_{sl}$	sub-sarcolemmal Ca^{2+} concentration
Ca^{2+}	calcium
K^+	potassium
Na^+	sodium

Vita

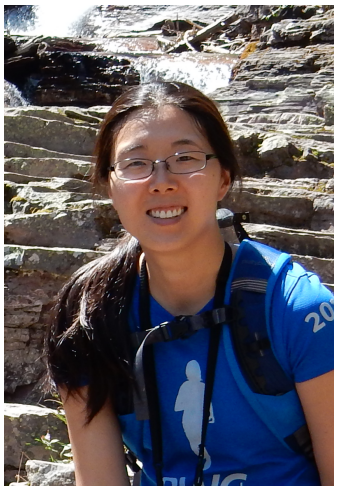

Kelly C. Chang was born on January 17, 1986 in Champaign, IL, U.S.A. She received the Sc. B. degree in Biological Engineering from Massachusetts Institute of Technology in 2008 and enrolled in the Biomedical Engineering Ph.D. program at Johns Hopkins University in 2009. She won the Znaty Award for Achievement in Biological Engineering and was inducted into the Phi Beta Kappa Honor Society in 2008. She received a National Science Foundation Graduate Research Fellowship Honorable Mention in 2010, the inaugural David C. Gakenheimer Fellowship Award in 2013, and an Achievement Rewards for College Scientists Scholarship in 2014. Her research focuses on computational modeling of cardiac electrophysiology and mechanisms of arrhythmia in disease.

Starting in July 2016, Kelly will join the Comprehensive in vitro Proarrhythmia Assay (CiPA) initiative as an ORISE Fellow, where she will work on a computational platform to screen drugs for proarrhythmic risk.